Sara Maria de Oliveira Gomes

RELIABILITY ANALYSIS OF FRP STRENGTHENED PRESTRESSED CONCRETE GIRDERS

Tese de doutoramento em Engenharia Civil na Especialidade de Mecânica Estrutural, orientada pelo Doutor Daniel Dias-da-Costa e pelo Doutor Luis Neves e apresentada ao Departamento de Engenharia Civil da Faculdade de Ciências e Tecnologia da Universidade de Coimbra.

Setembro, 2016

· U C ·

UNIVERSIDADE DE COIMBRA

Sara Maria de Oliveira Gomes

Reliability Analysis of FRP Strengthened Prestressed Concrete Girders

Tese de doutoramento em Engenharia Civil na Especialidade de Mecânica Estrutural, orientada pelo Doutor Daniel Dias-da-Costa e pelo Doutor Luis Neves e apresentada ao Departamento de Engenharia Civil da Faculdade de Ciências e Tecnologia da Universidade de Coimbra.

Setembro, 2016

Universidade de Coimbra

To my father
To my mother
To my brother

Resumo

Nas últimas décadas o grande aumento de tráfego proporcionou fortes investimentos em redes de autoestradas. A utilização de vigas prefabricadas em betão pré-esforçado é uma das possíveis soluções empregue na construção de pontes e viadutos. Contudo, o envelhecimento destas estruturas devido a vários fenómenos (corrosão, falta de manutenção, sobrecarregamento, impactos, etc), faz com que o seu tempo de vida útil se torne mais reduzido do que o inicialmente previsto, e consequentemente seja cada vez mais frequente recorrer ao seu reforço ou reabilitação.

O uso de polímeros reforçados com fibras (FRP) como reforço por colagem externa (EBR) tem-se vindo a popularizar devido às suas vantagens, nomeadamente: baixo custo, rapidez e facilidade de aplicação. No entanto, o uso de FRP na construção civil é ainda relativamente recente quando comparado com outros materiais tais como o betão ou o aço, sendo a maioria dos estudos relacionados com esta matéria de natureza experimental ou numérica. Nesta tese, é apresentado um estudo de fiabilidade de vigas em betão pré-esforçado reforçadas com FRP de carbono (CFRP).

É estudada a natureza estatística das propriedades mecânicas de CFRP, sendo este um assunto de extrema importância na análise de fiabilidade de elementos estruturais reforçados com FRP, dada a sua relevância na resistência estrutural. Os modelos desenvolvidos permitem caracterizar estatisticamente as propriedades mecânicas de CFRP para serem usados em análises do âmbito de fiabilidade estrutural.

São efectuadas análises de fiabilidade de vigas em betão pré-esforçado representativas do contexto estrutural português dos últimos 40 anos. Estas análises têm como objetivo a calibração de coeficientes parciais de segurança de CFRP, considerando o comportamento não linear das vigas através de modelos de elementos finitos com

descontinuidades fortes para caracterizar a fissuração do betão e tendo em conta: i) o método de fiabilidade de primeira ordem (FORM) e o método da superfície de resposta (RSM), ii) vários níveis de dano estrutural, iii) laminados de CFRP para reabilitar as vigas; e iv) o regulamento Português RSA para o dimensionamento e o regulamento Eurocódigo 1 para o reforço. Os resultados mostram que o RSA é menos conservativo que o Eurocódigo 1, as variáveis sobrecarga de tráfego e incertezas nos modelos são fundamentais para este tipo de análise e o coeficiente parcial de segurança determinado está de acordo com os sugeridos em regulamentos existentes – CEB/FIB e CNR. Esta metodologia pode servir de apoio ao desenvolvimento de regulamentos de dimensionamento de reforço de estruturas com FRP, tendo em conta o comportamento não linear, a degradação e o contexto estrutural.

Posteriormente são realizadas análises de fiabilidade em função do tempo de uma viga em betão pré-esforçado, considerando a degradação devido à corrosão dos cabos de pré-esforço, que é uma das causas mais preocupantes para a degradação estrutural. Para tal, a corrosão é estimada variar: i) em função do tempo através de modelos existentes; e ii) ao longo do comprimento da viga considerando os limites de Ditlevsen para análises de fiabilidade de elementos em série. As vigas são reabilitadas com laminados de CFRP. Os limites de Ditlevsen mostram ser uma ferramenta útil para calcular a fiabilidade de sistemas em série de vigas em betão pré-esforçado, considerando a corrosão ao longo da viga, e os CFRP mostram poder recuperar com sucesso a fiabilidade estrutural a longo prazo. O método apresentado prova ser útil para apoiar os engenheiros durante o processo de tomada de decisões.

Palavras-chave:

FRP, viga, betão pré-esforçado, análise de fiabilidade, análises numéricas.

Abstract

During the last decades, large stocks of prestressed concrete (PC) girders bridges were built all over the world to accommodate the growth in traffic. However, the deterioration processes often observed in reinforcement concrete (RC) elements, resulting from several factors (e.g., corrosion, lack of maintenance, overloading, impact, etc), can reduce significantly its structural lifetime. Thus, when a certain degree of deterioration is reached, strengthening is a fundamental tool to restore the full structural capacity.

The use of fibre reinforced polymer (FRP) composites as externally bonded reinforcement (EBR) for repair or rehabilitation purposes, is an increasingly used technology given its advantages, namely reduced costs, low weight, simplicity of installation and quickness. Nonetheless, the use of FRP in concrete structures is relatively new, when compared with other materials – e.g., concrete or steel – and the majority of studies concerning this subject are of experimental or numerical nature, neglecting probabilistic based studies. This thesis deals with different topics related with reliability analysis of carbon FRP (CFRP) strengthened PC girders.

The statistical characteristics of the mechanical properties of CFRP are firstly studied. This is fundamental for structural reliability of FRP strengthened elements, since these are usually important in failure. The developed models provide a way of characterising the probabilistic nature of CFRP for reliability analysis.

After this, PC girders representing the construction practice in Portugal during the last four decades, are analysed. A method for the calibration of CFRP partial safety factors considering non-linear finite element analysis using strong discontinuities for concrete cracking is presented. The proposed procedure uses: i) the First Order

Reliability Method (FORM) and the Response Surface Method (RSM), ii) several levels of damage, iii) CFRP laminates to repair or upgrade the girders; and iv) the Portuguese code RSA during the design stage and the Eurocode 1 for the strengthening process, to characterise the structural context. Additionally, the outcomes of this study confirm that the RSA is less conservative than the Eurocode 1, traffic loads and models uncertainties random variables are fundamental for this type of analysis and the computed partial safety factor is in agreement with those proposed in existing codes – CEB/FIB and CNR. This methodology can support the development of a safety-check code for the use of FRP, taking into account the structural non-linear behaviour and degradation.

A time-dependent reliability analysis of a PC girder is also carried out considering the deterioration due to prestressing strands corrosion, which is the most concerning cause of RC structures degradation. The temporal and spatial nature of corrosion is considered through: i) existing time-dependent models; and ii) series system reliability analysis using the Ditlevsen bounds. The repair process to restore the girder safety is considered to be made using CFRP as EBR. The adopted procedure shows that pitting corrosion strongly reduces the reliability of the girder, which can be successfully restored using CFRP. Additionally, spatial corrosion can be considered using the Ditlevsen bounds and traffic loads, models uncertainties and corrosion rate are the most important variables. This method can be a basis for a tool used for maintenance decision practices for the concrete heritage.

Keywords:

FRP, girder, prestressed concrete, reliability analysis, finite element analysis.

Acknowledgements

I want to thank:

- to my advisor Doctor Daniel Dias-da-Costa for his guidance and constructive suggestions throughout this thesis;
- to my co-advisor Doctor Luis Neves for his guidance and teaching during this work, and also for having me at Nottingham University;
- to Doctor Rui Graça-e-Costa for his support with the numerical software;
- to all my colleagues from the University of Coimbra for the three years of friendship and fun;
- to all my colleagues from the Nottingham Transportation Engineering Centre (NTEC), University of Nottingham, for having me so well during the year I have spent there.
- to S&P - Clever Reinforcement Ibérica for the experimental results of fibre reinforced polymer composites tensile tests;
- and to the Portuguese Science and Technology Foundation (FCT) for their financial support (Ph.D. Grant Number SFRH/BD/76345/2011).

Finally, I want to thank:

- to my family: my father, my mother and my brother for showing me the engineering of life;
- and to Carlos for always being there.

Supporting Institutions:

Contents

List of Figures

List of Tables

List of Symbols

Latin lower case letters

$\boldsymbol{a}$	Total displacement vector at the nodes
$\hat{\boldsymbol{a}}$	Regular displacement vector at the nodes
$\tilde{\boldsymbol{a}}$	Enhanced displacement vector at the nodes
b	Cross section width
$\bar{\boldsymbol{b}}$	Body forces vector
b_w	Web thickness
c	Concrete cover
d	Cross section effective depth
$\boldsymbol{f}$	Vector of global nodal forces
$\hat{\boldsymbol{f}}$	Regular external vector force at the regular nodes
f_c	Compressive strength of concrete
f_{cm}	Mean of concrete cylinder compressive strength
f_{ctm}	Mean value of concrete axial tensile strength
f_f	Tensile strength of FRP
$f_{p0.1}$	0.1% proof-stress of prestressing steel
f_y	Yield strength of longitudinal reinforcement
$\hat{\boldsymbol{f}}_w$	External vector force at the additional nodes
g_f	Division of G_f by the applicable value in the smeared crack approach
h	Height
i_c	Corrosion rate
i_{corr}	Corrosion current
k_n, k_s	Normal and shear penalties
l_d	Length of the discontinuity

$\boldsymbol{n}^+$	Unit vectors orthogonal to the discontinuity composing the local frame
p	Radius of pit
q_k	Characteristic distributed variable action
r^2	Coefficient of determination
s	Local slip
$\boldsymbol{s}$	Unit vector tangent to the discontinuity composing the local frame
t	Time
$\boldsymbol{t}$	Traction vector
$\bar{\boldsymbol{t}}$	Natural forces vector
$\boldsymbol{u}$	Total displacement vector
u^*	Coordinates at design point
$\bar{\mathbf{u}}$	Regular displacement vector field
$\tilde{\mathbf{u}}$	Enhanced displacement vector field
$[\![\mathbf{u}]\!]$	Jump vector
$\mathbf{w}^e$	Nodal jump vector
wc	Water-cement ratio

Latin upper case letters

A_f	Cross sectional area of FRP
A_p	Cross sectional area of prestress reinforcement
A_{pit}	Area of pit
C	Chloride concentration
C_s	Chloride concentration on concrete surface
C_{th}	Chloride threshold value
D_0	Initial prestressing bar diameter
D_{cl}	Chloride diffusion coefficient
E_{cm}	Secant Young's modulus of concrete
E_f	Young's modulus of FRP
E_p	Young's modulus of prestressing steel
E_s	Young's modulus of reinforcing steel
F	Action
G	Limit state function

G_f	Fracture energy
$\mathbf{H}_{\Gamma_d}$	Diagonal matrix containing the Heaviside function evaluated at each degree of freedom
$\boldsymbol{K}$	Stiffness matrix
$\boldsymbol{K}_{aa}$	Stiffness matrix for the interface elements
$\boldsymbol{K}_{\hat{a}\hat{a}}$	Bulk stiffness matrix
$\boldsymbol{K}_{aw}, \boldsymbol{K}_{wa}, \boldsymbol{K}_{ww}$	Enhanced bulk stiffness matrices
$\boldsymbol{K}_d$	Discontinuity stiffness matrix
L	Span
L_u	Effective length
$\mathbf{L}_w$	Matrix computing the difference between top and bottom displacements for an interface
M	Bending moment
M_D	Bending moment caused by dead loads
M_L	Bending moment caused by live loads
M_{Rd}	Design value of the bending moment resistance
M_{Sd}	Design value of the applied internal bending moment
$\boldsymbol{M}_w$	Matrix transmitting the jump from the discontinuity opening
$\boldsymbol{N}_w$	Shape function matrix for the jumps
P_{av}	Average pit depth
P_f	Probability of failure
P_{max}	Maximum pit depth
Q_k	Characteristic concentrated variable action
R	Structure resistance
S	Structure solicitation
$\boldsymbol{T}$	Discontinuity constitutive matrix
V	Coefficient of variation

Greek lower case letters

α	Sensitivity factor
β	Reliability index
β_t	Target reliability index
γ	Partial safety factor

γ_c	Concrete self-weight; partial safety factor of concrete
γ_{dl}	Dead loads; partial safety factor of dead loads
γ_f	Partial safety factor of FRP
γ_{ic}	Corrosion model error
γ_p	Partial safety factor of prestressing strength
γ_Q	Partial safety factor of traffic loads
γ_{tl}	Traffic loads scale factor
δ	Vertical displacement
δ_{Γ_d}	Dirac's delta function along the discontinuity
$\boldsymbol{\varepsilon}$	Total strain tensor
$\hat{\boldsymbol{\varepsilon}}$	Regular strain tensor
ε_0	Concrete strain in the most extreme tensile fibre before strengthening
ε_c	Compressive strain in concrete
ε_{c1}	Compressive strain in concrete at peack stress f_c
ε_{fu}	Ultimate strain of FRP
θ_E	Load model uncertainties
θ_R	Resistance model uncertainties
μ	Mean value
σ	Standard deviation
$\boldsymbol{\sigma}$	Stress vector
σ_c	Compressive stress in concrete
τ	Local bond stress
ϕ	Reduction factor

Greek upper case letters

Γ	Boundary
Ω	Body

Acronyms

ACI	American Concrete Institute
AFRP	Aramid fibre reinforced polymer

CDF	Cumulative distribution function
CEB/FIB	Euro-International Concrete Committee/International Federation for Structural Concrete
CEN	European Committee for Standardisation
CFRP	Carbon fibre reinforced polymer
CNR	Italian National Research Council
CoV	Coefficient of variation
CSA	Canadian Standards Association
CV	Critical value
DSDA	Discrete strong discontinuity approach
EBR	Externally bonded reinforcement
EC	Eurocode
FE	Finite element
FORM	First order reliability method
FRP	Fibre reinforced polymer
GFRP	Glass fibre reinforced polymer
JCSS	Join Committee on Structural Safety
LRFD	Load Resistance Design Format
MLE	Maximum likelihood estimation
MCS	Monte Carlo simulation
MPP	Most probable point
PC	Prestressed concrete
PDF	Probability density function
RC	Reinforced concrete
RSA	Regulamento de Segurança e acções
RSM	Response Surface Method
SLA	Sequentially Linear Approach
SLS	Service Limit State
SORM	Second order reliability method
TR 55	Technical Report No. 55 - English Concrete Society
ULS	Ultimate Limit State

Chapter 1

Introduction

1.1 Overview

In the last five decades, significant resources were invested in developed countries to create new highways networks given the increase of road traffic. In order to give a proper answer to this need, large stocks of reinforced concrete (RC) bridges using precast prestressed concrete (PC) girders were built. Numerous examples of such structures (see Figure 1.1) can be found all over the world. This structural solution was mainly used due to the advantages that the prefabrication industry presents over the cast in-situ solutions, as for instance: speed of construction, economic solutions or controlled materials quality.

After several decades of use, there are a number of reasons that may lead to the need of repair and/or strengthening of these structural elements, such as accidental actions (see Figure 1.2 (a)), lack of maintenance, environmental degradation (see Figures 1.2 (b) and (c)), poor materials, inadequate construction methods (see Figure 1.2 (d)), poor design practices, overloading or change in use (CEB/FIB, 2001). Moreover, for a large part of existing structures in developing countries, the design life has already been reached or is about to be, very soon.

To provide answers to the need of repair and/or strengthening of RC structural elements, several techniques were developed. One of the most accepted for strength-

(a) (b)

Figure 1.1: PC girders in Leiria over: (a) the pedestrian circuit in the city centre; and (b) highway A19.

ening RC elements consists in using fibre reinforced polymer (FRP) composites as externally bonded reinforcement (EBR). When compared with other EBR techniques, such as the ones based on epoxy-bonded steel plates or concrete jacketing, the use of FRP is becoming more popular due to reduced costs, low weight and easy transportation and installation (CNR, 2013). Together with the latter qualities, the speed of application makes this method one of the most used by engineers to restore the full capacity of RC bridges in a short period of time, as seen in Figure 1.3. Additionally, it is important to highlight that when it comes to deal with public structures that assume an important role for countries, the chosen method undertakes a higher importance for the overall economy competitiveness.

The growing usage of FRP in construction field led to the publication of new design guides for RC structures strengthened with this material, such as CEB/FIB (2001), CNR (2013), TR-55 (2000) or ACI 440 (2008). These represent the efforts made in the last years to improve the safe use of composite materials in construction (Wang et al., 2010). Nevertheless, there are still some issues that have to be addressed to develop semi-probabilistic based design codes capable to ensure a confidence level to FRP compatible with other materials, such as steel or concrete (Wang et al., 2010). For instance, the statistical characterisation of large batches of FRP or the consideration of degradation scenarios for guidelines calibration are issues that are still missing.

Up to now, and in spite efforts made during the last 30 years to study safety factors

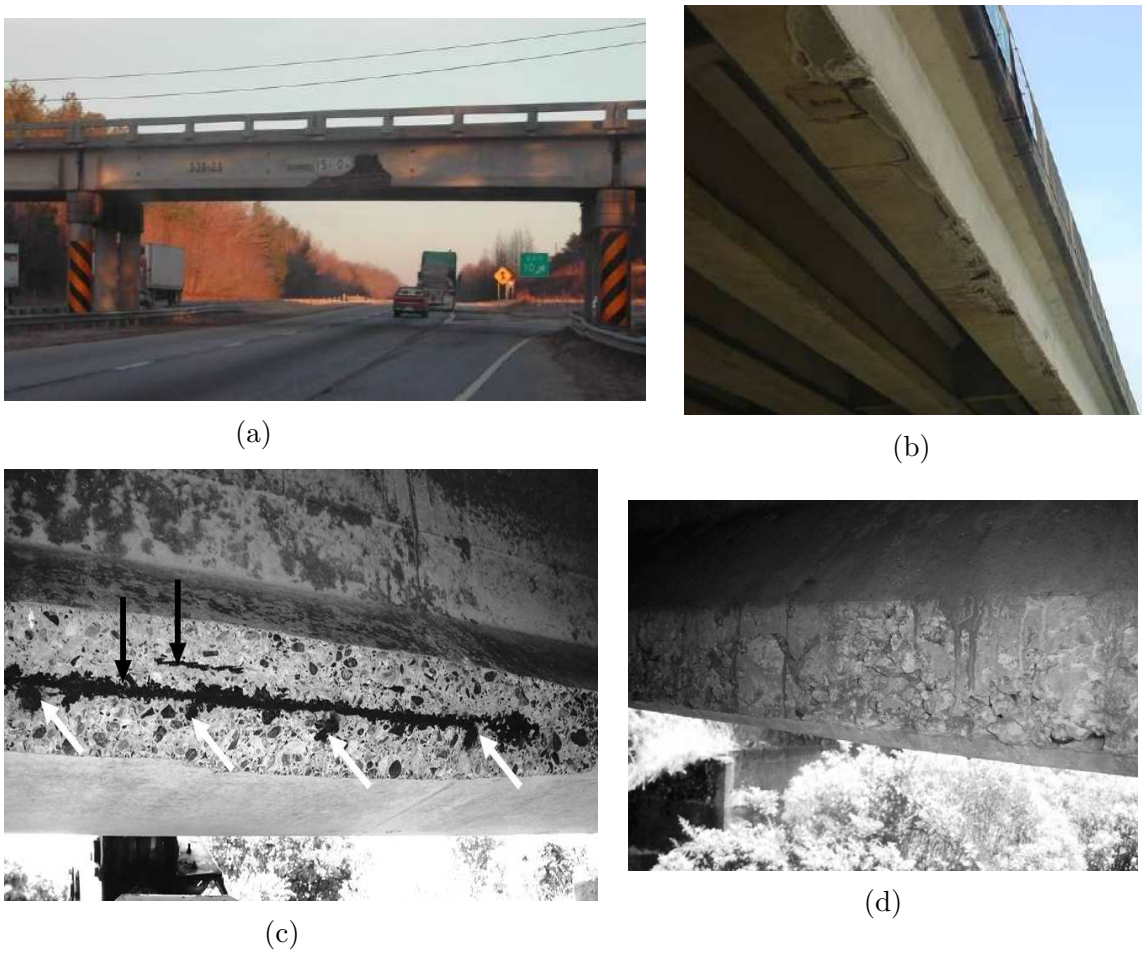

Figure 1.2: Several types of damage in PC girders: (a) loss of section due to vehicle impact in the middle span, (b) concrete spalling, (c) spalling over prestressing strand and corrosion; and (d) poor compaction of concrete (Bruce et al., 2008; Harries et al., 2009).

and to develop design methodologies based on probabilistic tools, the great majority of studies related with RC girders strengthened with FRP are mostly experimental. Some examples of reliability analysis of FRP strengthened RC beams can still be found in literature, such as: Plevris et al. (1995), El-Tawil and Okeil (2002), Atadero and Karbhari (2008) or Wang et al. (2010).

Less research has been dedicated to the time-dependent reliability analysis of RC beams retrofitted with FRP (Bigaud and Ali, 2014). This issue can assume particular interest since FRP is used to extend the structural lifetime horizon. Until now, several authors, such as Stewart (2004, 2012); Stewart and Al-Harthy (2008); Stewart and Mullard (2007); Stewart and Rosowsky (1998a); Stewart and Suo (2009);

Figure 1.3: Application of FRP laminates in PC girders (Sika Group [online]).

Val and Melchers (1997); Val et al. (1998); Vu and Stewart (2000) have used a procedure for time-dependent reliability that considers spatial variability of corrosion over beams. Nonetheless, only Bigaud and Ali (2014) have studied the time-dependent reliability of FRP strengthened girders.

1.2 Objectives

The main objective of this thesis is to establish a framework to assess the reliability of FRP strengthened PC girders. In particular, the following objectives have been identified:

- *statistical characterisation of mechanical properties of carbon FRP (CFRP):*

  to propose new statistical and correlation models to characterise mechanical properties of CFRP, based on a large batch of tension tests of pre-cured laminates embedded in epoxy matrices. The models are based on the main mechanical properties, such as Young's modulus, tensile strength and ultimate strain;

- *calibration of partial safety factors for CFRP considering reliability analysis*:

  to present an advanced methodology to compute structural reliability of CFRP strengthened PC girders and partial safety factors for CFRP. The proposed

methodology is based on the present Portuguese structural context and the simulation of the structural behaviour is addressed; in particular the degree of detail vs. computational cost in the choice of numerical and analytical models;

- *time-dependent reliability analysis of PC girders strengthened with CFRP:*

  to establish a methodology to compute time-dependent reliability for FRP strengthened PC girders that accounts for time and spatial evolution of corrosion, the most concerning cause of RC elements degradation, considering the Portuguese structural context.

1.3 Outline

The thesis is divided in seven chapters, schematised in the Figure 1.4, and described in the following:

- the first chapter presents a general introduction to the problem, the objectives and the outline of the thesis;
- in Chapter 2, a literature review on structural reliability is performed. The aim of this chapter is to provide the necessary theoretical background for the understanding of this thesis. It starts with a briefly introduction to the importance of structural reliability and some basic statistical principles. Afterwards, the concepts of probability of failure and the reliability index are outlined, followed by the description of reliability methods, the response surface method, time-dependent reliability and assessment of existing structures. Finally, the procedure using reliability methods for codes calibration is addressed;
- Chapter 3 presents a statistical study of the mechanical properties of CFRP. First, an introduction to FRP as a strengthening material for construction and its use in RC beams is made. Then, the statistical analysis of probabilist models of CFRP mechanical properties, including the correlation analysis between properties, is presented;
- Chapter 4 focus the adopted numerical and analytical models and underlying assumptions. All relevant aspects of the discrete crack model used in the

numerical analysis and the adopted methodology employed for the analytical models are described. Models validation using experimental data available and the main conclusions are also summarised;

- Chapter 5 introduces the calibration of partial safety factors for CFRP. A review of the existing studies and an introduction to the most relevant design guidelines for RC structures strengthened with FRP are made. Subsequently, the adopted procedure used for reliability analysis, describing the structural, load and statistical models is introduced. Finally, the results are shown;

- Chapter 6 presents the time-dependent reliability analysis, starting with the existing studies and the corrosion mechanism of reinforcing steel in RC structures. Then, the adopted procedure is thoroughly detailed, including the case study, time- and spatial-dependent models used for steel corrosion, degradation model adopted for CFRP strength and statistical variables. In the end, the results are presented;

- finally, Chapter 7 summarises the major conclusions and highlights possible future developments.

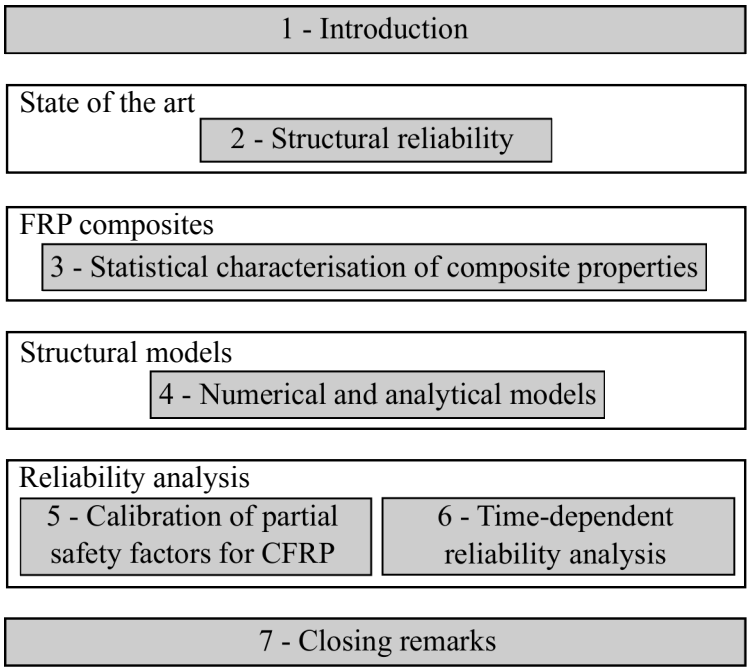

Figure 1.4: Thesis organisation.

Chapter 2

Structural reliability

In structural engineering problems, all stages concerning the planning, design, construction, operating and decommissioning of structures are susceptible to errors, in which consequences and uncertainties vary (Faber, 2005). The structural reliability field consider the treatment of these existing uncertainties that may cause structural failure (Faber, 2005). Additionally, a better understanding of structural reliability, as new statistical data or construction methods are available, contribute to improve the assessment of structural probability of failure by setting probabilistic models for loads and resistances, based on available statistical information (Melchers, 1999).

This chapter describes some of the basic aspects of structural reliability based on fundamental bibliography. This framework is the basis of the studies presented in the following chapters. First, in Section 2.1, structural reliability is introduced, followed by the definition of some basic statistical concepts in Section 2.2. Then, structural reliability notions and the codes calibration process based on reliability methods are described in Sections 2.3 and 2.4, respectively.

2.1 Introduction

Structural safety is essential to ensure the safety of citizens and to minimise economical losses. In our society, citizens expect the failure of structures to be an extremely

rare event and typically do not address this problem as a risk for society. In fact, people only consider structural failures after its occurrence, trusting engineers to plan and ensure proper construction and maintenance (Ellingwood, 2000; Schneider, 1997). On the other hand, engineers rely on codes and standards to provide an effective answer to the following question (Fischhoff et al., 1978):

"How safe is safe enough?"

Starting from the fact that it is impossible to achieve absolute safety, an adequate answer to the previous question should consider that there is safety when risk is limited to acceptable levels. Figure 2.1 illustrates the relation between potential hazard and treated risk, showing that just part of total hazard is objectively known and subjectively realised; and therefore just a part of potential hazard is taken into account. Furthermore, risk treatment measures are planned to deal just with the not accepted risks and not all measures are considered adequate to control risk. In the end, just a part of potential hazards are prevented with correctly implemented measures, whereas the not prevented part is accepted or caused by human errors (Faber, 2005; Schneider, 1997).

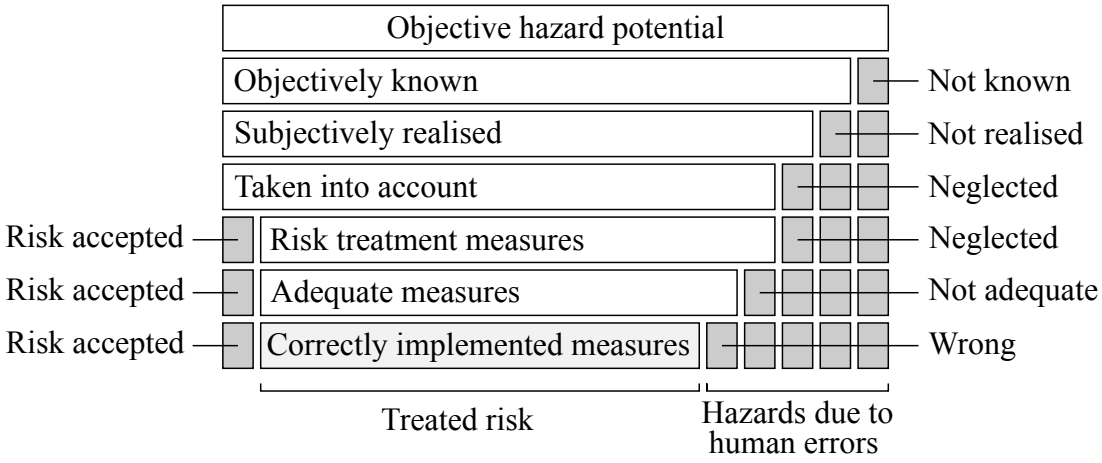

Figure 2.1: Relation between total hazard and distribution of accepted risks, treated risks and risks due to human errors (Faber, 2005).

The definition of risk can be understood as the expected consequences associated with an activity as:

$$R = P \times C \tag{2.1}$$

where R is the risk, P is the probability of occurrence of an event and C are the potential consequences of that event (Faber, 2005; Stewart and Rosowsky, 1998a). Understanding all potential hazards that may lead to personal, environmental and economic consequences, is therefore essential (Faber, 2005).

Engineers rely on probabilistic and statistic tools to control, to a certain extend, the uncertainties present in structural loads and material properties (Ellingwood, 2000). The sources of uncertainty are very dependent on the purpose of risk analysis and may include (Faber, 2005; Melchers, 1999; Stewart and Rosowsky, 1998a):

- physical uncertainties – associated with material properties, structure geometry, loading environment and construction or rehabilitation quality;
- statistical uncertainties – related with the finite size of statistical data;
- model uncertainties – associated with the mathematical models adopted to simulate structural behaviour and to characterise material properties;
- phenomenological uncertainties – which emerges when the form of construction or design causes uncertainty in its behaviour under construction, service or extreme conditions;
- decision uncertainties – related with the decision if a phenomenon has occurred;
- prediction uncertainties – associated with the anticipation of possible future situations;
- uncertainties due to human factors – resulted due to i) human errors; and ii) human intervention.

There are several methods to calculate the structural probability of failure that combine potential uncertainties. The procedure details can vary according to the problem and can be summarised in 4 levels (Melchers, 1999):

Level 1 - Code level methods

This is the simplest level and the most commonly used format by limit state codes. Probabilities are only considered implicitly.

Level 2 - Second moment methods

Only normal distributions are used and simple limit state functions are considered to compute the probability of failure.

Level 3 - Exact methods

The probability of failure is obtained using the best probabilities models available. At this level, uncertainties caused due to variability of human activities and time-dependent reliability analysis may be considered.

Level 4 - Decision methods

This level considers any of the described methods and economic data to compute the minimum costs or the maximum benefits. It is used as a decision tool.

2.2 Basic principles

In this section, some elementary statistical definitions are briefly described to facilitate the understanding of following sections.

2.2.1 Random variables

Random variables are numerical outcomes from uncertainty phenomena and can be used to define mathematical functions capable of describing a pattern over a sample space. The variation of a continuous random variable can be described using a probability density function (PDF), whereas the cumulative distribution function (CDF) can be adopted either for discrete or continuous variables – see Figure 2.2. Both functions are described, respectively, as follows:

$$f_X(x) = \frac{dF_X(x)}{dx} \tag{2.2}$$

and

$$F_X(x) = P(X \leq x) = \int_{-\infty}^{x} f_X(x)dx \tag{2.3}$$

where P is the probability and X is the random variable equal or less to a certain value of x.

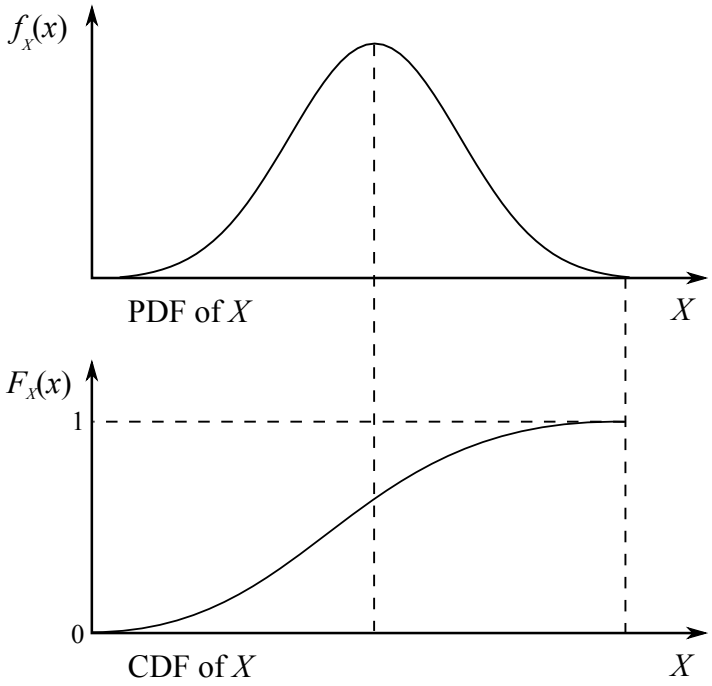

Figure 2.2: PDF and CDF of a random variable (Schneider, 1997).

Each random variable X is defined using few parameters, usually called moments (Faber, 2005; Melchers, 1999):

First moment - arithmetical mean

The first moment measures the central tendency of a random variable, and for continuous variables can be defined as:

$$E(X) = \mu_x = \int_{-\infty}^{+\infty} x f_X(x) dx \tag{2.4}$$

Second moment - variance

The variance measures the scatter of continuous random variables as:

$$E(X - \mu_X)^2 = \sigma_X^2 = \int_{-\infty}^{+\infty} (x - \mu_X)^2 f_X(x) dx \tag{2.5}$$

in which σ_X is the standard deviation. Additionally, the coefficient of variation,

that is a dimensionless measure of uncertainty, can be computed as:

$$V_X = \frac{\sigma_X}{\mu_X} \tag{2.6}$$

Third moment - skewness

The third moment measures the asymmetry of a distribution over the mean:

$$E(X - \mu_X)^3 = \int_{-\infty}^{+\infty} (x - \mu_X)^3 f_X(x) dx \tag{2.7}$$

Fourth moment - kurtosis

The kurtosis gives the flatness of a distribution and is defined by:

$$E(X - \mu_X)^4 = \int_{-\infty}^{+\infty} (x - \mu_X)^4 f_X(x) dx \tag{2.8}$$

2.2.2 Distributions fitting

In engineering there are several families of distributions that can be used to describe sets of random variables, such as the uniform, triangular, normal, log-normal, gamma, beta, exponential, Gumbel (extreme type I), Frechet (extreme type II), Weibull (extreme type III) or Poisson.

The distribution fitting process consists in adjusting an appropriate distribution to a random data and typically is not a straightforward process, specially when available data has a limited size. This process can be supported by using graphic plots, such as the histogram, shown in Figure 2.3 (a), which is a bar diagram that presents the relative frequency of data in a predefined interval. This plot allows estimating the PDF of the underlying variable. Figure 2.3 (b) shows the Q-Q plot that is used to verify the correspondence between data and analytical results.

Several goodness-of-fit tests are used to help the fitting decision, such as the Chi-Square, the Anderson-Darling, the Pearson's chi-squared or the Kolgomorov-Smirnov. These tests typically compute the discrepancy between two data sets. Further details are described later in Section 3.4.2.

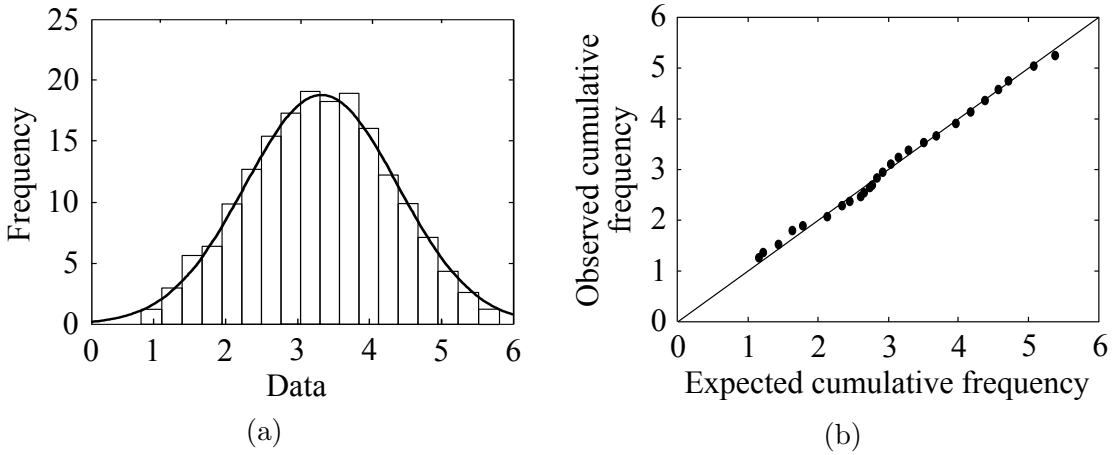

(a) (b)

Figure 2.3: Graphical representation of random data: (a) histogram; and (b) Q-Q plot.

2.2.3 Linear correlation

When two (or more) variables are under analysis, one question that often arises is whether there is any degree of interdependence and how significant it is. In this scope, the covariance can be used to measure linear interdependence for continuous variables (Schneider, 1997):

$$Cov(x, y) = \frac{1}{n-1} \sum_{i=1}^{n} (x_i - \mu_x)(y_i - \mu_y) \tag{2.9}$$

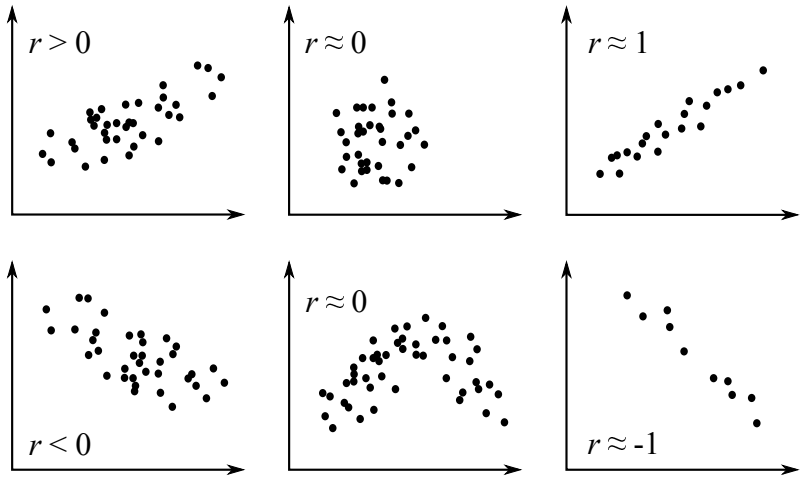

Figure 2.4: Linear correlation plots (Schneider, 1997).

A dimensionless correlation coefficient for the statistical relationship can be defined as follows:

$$r_{x,y} = \frac{Cov(x,y)}{\sigma_x \sigma_y} \tag{2.10}$$

which can assume values in the range of -1 to 1 – see Figure 2.4 – where -1 or 1 correspond to fully correlated and 0 to totally uncorrelated variables.

2.3 Aspects of structural reliability

Reliability can be defined according to Schneider (1997) as:

"the probability of an item performing its intended function in a specified period of time, under defined conditions."

The probability of failure, P_f, is a complement of reliability ($Reliability = 1 - P_f$) and makes use of statistical knowledge of uncertainties. In this context, structural failure is said to occur when a random structural resistance, R, is lower than the corresponding random load demand, S, as:

$$P_f = P(R - S < 0) \tag{2.11}$$

In structural reliability, the problem set in Equation (2.11) is defined by a limit state function $G(X_i)$, corresponding to the boundary between acceptable and unacceptable performances of a structure (Nowak and Collins, 2012). This function depends on the random variables, X_i, that represent the properties of the problem according to predefined distributions. The limit state is violated whenever the failure condition is exceeded:

$$G(X_i) < 0 \tag{2.12}$$

In structural engineering there are two fundamental limits states: i) the Ultimate Limit State (ULS); and ii) the Service Limit State (SLS). Whereas the first limit is related with the loss of capacity that may affect both people and structural safety, the latter is related with unacceptable serviceability conditions, including excessive

deterioration, cracking, deformation or vibrations affecting comfort and the normal use of the structure (CEN, 2002a).

When only two variables are considered, the probability of failure corresponds to the grey volume depicted in Figure 2.5, where $G(r, s) < 0$ or $r < s$, and can be defined by:

$$P_f = \iint\limits_{G()<0} f_{R,S}(r, s)drds \tag{2.13}$$

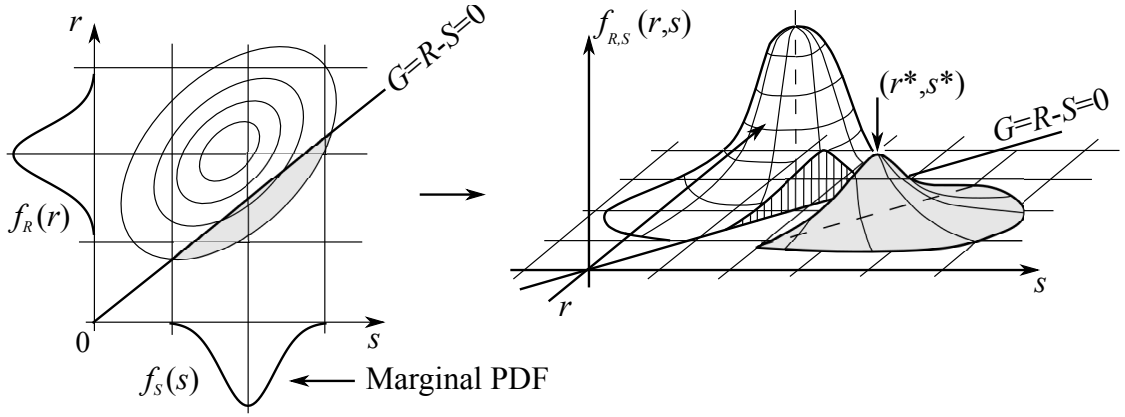

Figure 2.5: Joint density function $f_{R,S}(r, s)$ of two random variables with the marginal density functions f_R and f_S (Schneider, 1997).

In the case of independent random variables, Equation (2.13) can be re-written as:

$$P_f = \int_{-\infty}^{+\infty} F_R(x) f_s(x)dx \tag{2.14}$$

where F_R is the CDF of structural resistance and f_S is the PDF of load demands.

2.3.1 Reliability index

The Cornell reliability index, β, can be used instead of the probability of failure (see Figure 2.6) (Schneider, 1997). For example, considering R and S independent and normally distributed variables, the limit state function in Equation (2.11) can be written as:

$$P(Z < 0) = P(R - S < 0) \tag{2.15}$$

with the mean, μ_Z, and the standard variation, σ_Z, given by:

$$\mu_z = \mu_R - \mu_S \tag{2.16}$$

$$\sigma_Z = \sqrt{\sigma_R^2 + \sigma_S^2} \tag{2.17}$$

and the Cornell reliability index defined as:

$$\beta = \frac{\mu_Z}{\sigma_Z} \tag{2.18}$$

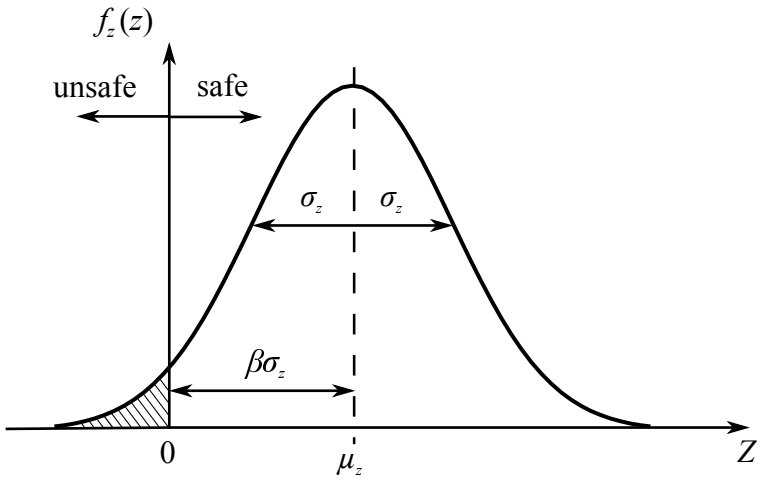

Figure 2.6: PDF of safety margin, Z (Schneider, 1997).

The probability of failure can be expressed by computing:

$$P_f = P(Z \leq 0) = \Phi\left(\frac{0 - \mu_Z}{\sigma_Z}\right) = \Phi(-\beta) \tag{2.19}$$

where Φ is the standard normal CDF with zero mean and unit standard deviation. Table 2.1 shows several values of β and corresponding probabilities of failure.

Table 2.1: Failure probability and corresponding reliability indices (CEN, 2002a).

P_f	10^{-1}	10^{-2}	10^{-3}	10^{-4}	10^{-5}	10^{-6}	10^{-7}
β	1.28	2.32	3.09	3.72	4.27	4.75	5.20

For linear limit state functions, the previous methodology can be extended to several

variables. The limit state function for i variables can then be written as:

$$Z = a_0 + \sum_{i=1}^{n} a_i X_i \tag{2.20}$$

where X_i is a random variable and the mean μ and standard variation σ of Z are:

$$\mu_Z = a_0 + \sum_{i=1}^{n} a_i.\mu_i \tag{2.21}$$

and

$$\sigma_Z = \left[\sum_{i=1}^{n} (a_i.\sigma_i)^2\right]^{1/2} \tag{2.22}$$

The reliability index is set according to Equation (2.18). It is limited to normal independent random variables and depends on the limit state function formulation.

2.3.2 Sensitivity factor

The sensitivity factor, α_i, shows the importance that each parameter has on the probability of failure – see Figure 2.7 – providing the contribution of each random variable to the safety and the relation between the performance function and physical variables. For R and S variables, this parameter can be defined as (Schneider, 1997):

$$\alpha_R = \frac{\sigma_R}{\sqrt{\sigma_R^2 + \sigma_S^2}} \tag{2.23}$$

$$\alpha_S = -\frac{\sigma_S}{\sqrt{\sigma_R^2 + \sigma_S^2}} \tag{2.24}$$

in which:

$$\alpha_R^2 + \alpha_S^2 = 1 \tag{2.25}$$

where α_R is the sensitivity factor and σ_R is the standard deviation of structural resistance; and σ_S is the standard deviation and α_S is the sensitivity factor of load demands. A positive α means that an increase of the mean value of the variable increases structural safety, whereas a negative alpha means the opposite.

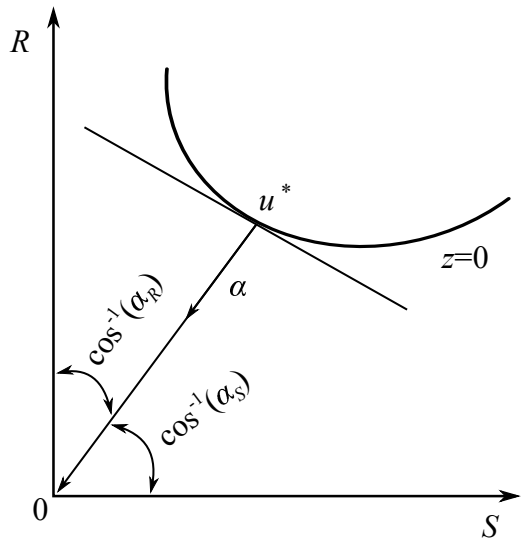

Figure 2.7: Cosines direction at design point.

2.3.3 Reliability methods

There are several methods to determine the reliability index and the probability of failure, when the influencing parameters are not normally distributed or the safety margin is not linear. In terms of reliability analysis, the approaches currently adopted are extensions of the method developed by Hasofer and Lind in 1974, according to Schneider (1997). The limit state function is transformed into the normalised standard space using standardised independent normally random variables. For example, the normally distributed variables R and S are transformed into standardised normally distributed U_1 and U_2 with a mean of 0 and a standard deviation of 1:

$$U_1 = \frac{R - \mu_R}{\sigma_R} \tag{2.26}$$

$$U_2 = \frac{S - \mu_S}{\sigma_S} \tag{2.27}$$

The failure surface no longer crosses the origin in the standard space – see Figure 2.8. The reliability index or the so called Hasofer/Lind safety index depends on the boundary between safe and failure domains (Faber, 2005), and is now measured as the minimum distance from the origin to the failure surface, given rise

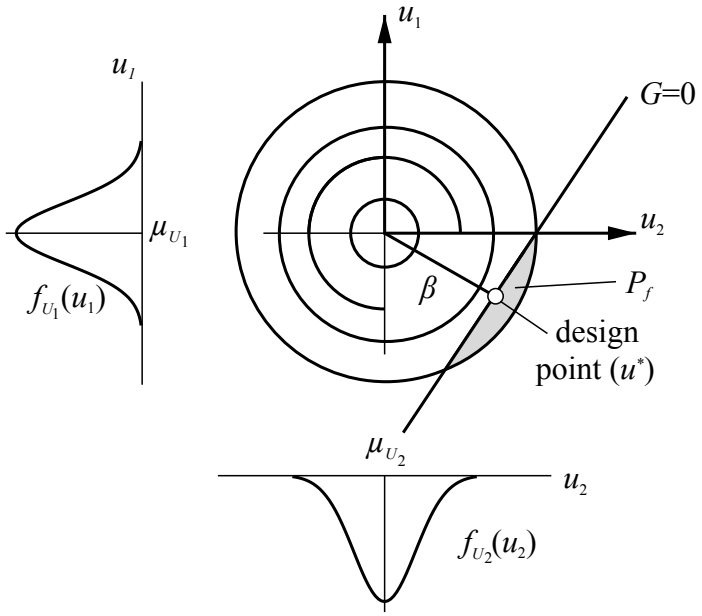

Figure 2.8: Reliability index and design point in the standard space, assuming a linear limit state function (Schneider, 1997).

to the design point:

$$\beta_{HL} = \min \left(\sqrt{\sum_{i=1}^{n} u_i^{*2}} \right) \tag{2.28}$$

where u is the vector of the random normal variables in the normal space and $*$ indicates that the values are taken at the design point.

Using the definition of reliability index, the weighting factors with several random variables can be written in as:

$$\alpha_i = \frac{\partial \beta}{\partial u_i^*} = \frac{\partial}{\partial u_i^*} \sqrt{u_1^{*2} + u_2^{*2} + \cdots + u_i^{*2}} = -\frac{u_i^*}{\beta} \tag{2.29}$$

where u_i are random variables.

2.3.3.1 First Order Reliability Method (FORM)

The direct evaluation of the probability in Equation (2.13) is not straightforward given the number of random variables and the non-linearity of limit state func-

tions. The FORM simplifies this process by transforming the distributions in equivalent more regular and symmetric forms, and by approximating the integration limit state function.

The FORM is based on the Hasofer and Lind reliability index definition described above and consists on a simple approach to compute small probabilities of failure. It is assumed that the non-linear limit state function is approximated using the first term of the Taylor expansion in the neighbouring region of the design point:

$$G = g(u_i^*) + \sum_{i=1}^{n}(U_i - u_i^*)\frac{\partial g}{\partial U_i} \tag{2.30}$$

or

$$G = g(u_i^*) + \nabla g(u_i^*)(U_i - u_i^*)^{\mathrm{T}} \tag{2.31}$$

where G is the limit state function, u_i are the normalised random variables, * is used to indicate partial differentials calculated at the design point and $\nabla g(u_i^*)$ is the gradient of $g(U)$ at u^* given by:

$$\nabla g(u_i^*) = \left(\frac{\partial g}{\partial U_1}, \frac{\partial g}{\partial U_2}, \ldots, \frac{\partial g}{\partial U_n}\right)\Bigg|_{u^*} \tag{2.32}$$

The first step in FORM consists in the transformation of the random variables from the original space (X-space) to a standard normal space (U-space) – see Figure 2.9. By this procedure, the shape of the integrand becomes regular and easier to compute, since the transformed variables follow a normalised distribution. This procedure can be achieved using the Nataf transformation (Nataf, 1962) described in the following (Melchers, 1999).

Nataf transformation

The Nataf transformation (Nataf, 1962) can be used when the joint CDF, $F_X(x)$, is not available but the marginal CDF, $F_{X_i}()$, and the correlation matrix, $\mathbf{P} = \{\rho_{ij}\}$, are available. The physical random variables X can be transformed into correlated standard normal variables U, considering the joint PDF approximation given by (Melchers, 1999):

$$f_X(x) = \phi_n(u, \mathbf{P'})|\mathbf{J}| \tag{2.33}$$

with the Jacobian defined by:

$$|\mathbf{J}| = \frac{\partial(u_1, \ldots, u_n)}{\partial(x_1, \ldots, x_n)} = \frac{f_{x_1}(x_1).f_{x_2}(x_2)\ldots f_{x_n}(x_n)}{\phi(u_1)\phi(u_2)\ldots\phi(u_n)} \tag{2.34}$$

and the correlation for any two variables given by:

$$\rho_{ij} = \int_{-\infty}^{+\infty}\int_{-\infty}^{+\infty} z_i z_j \phi_2(u_i, u_j, \rho'_{ij}) d_{u_i} d_{u_j} \tag{2.35}$$

in which $Z_i = (X_i - \mu_{x_i})/\sigma_{X_i}$, μ_{x_i} and σ_{X_i} are respectively the mean and standard deviation of X_i and ϕ_2 is the 2D standard normal PDF with the correlation coefficient ρ.

The independent normal variables are then obtained from:

$$\begin{aligned} u_1 &= L_0^{-1} z_1 \\ u_2 &= L_0^{-1} z_2 \\ &\vdots \\ u_n &= L_0^{-1} z_n \end{aligned} \tag{2.36}$$

where L_0^{-1} is the lower-triangular decomposition of $\mathbf{P}_0 = \rho_{0ij}$, such that $\mathbf{L}_0\mathbf{L}_0^T = \mathbf{P}_0$.

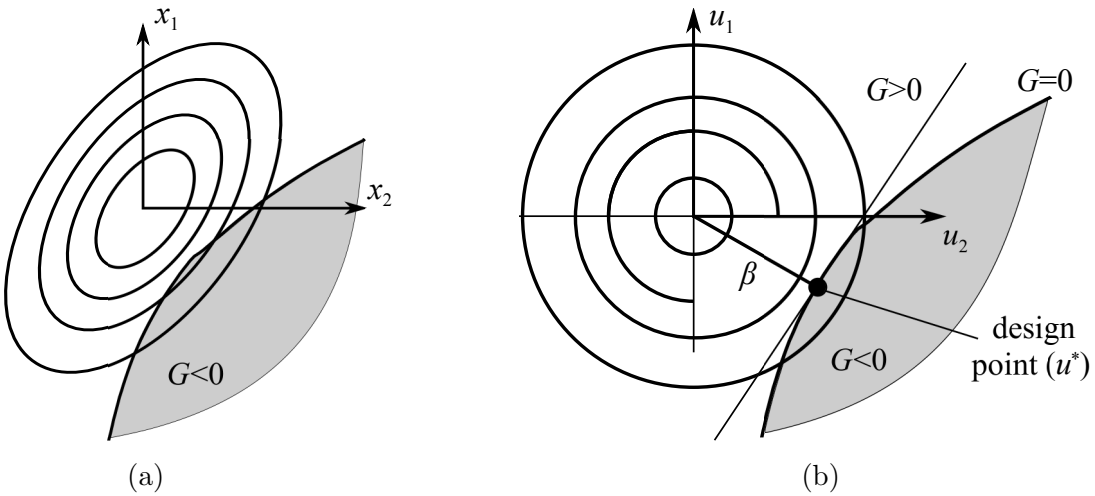

Figure 2.9: Probability integration in: (a) X-space; and (b) U-space.

Most Probable Point (MPP) search

The design point, also called the Most Probable Point (MPP) of failure, is then iteratively found in the standard space by solving the optimisation problem shown in Figure 2.10:

$$u^* = \arg\min \{\| u \|,\ g(u, \theta_g) = 0\} \tag{2.37}$$

where $g(u, \theta_g)$ is the limit state function, u is the realisation of random vectors U and θ_g is the vector of the deterministic limit state function (failure occurs when $g(u, \theta_g) \leq 0$).

For each iteration a new MPP, u, is found until convergence is reached. For instance, for the n^{th} iteration, the linearised limit state function at u can be defined according to:

$$g(u) = g(u^n) + \nabla g(u^n)(u - u^n)^{\mathrm{T}} \tag{2.38}$$

and the linearised limit state function in the next iteration will be:

$$g(u^{n+1}) = g(u^n) + \nabla g(u^n)(u^{n+1} - u^n)^{\mathrm{T}} = 0 \tag{2.39}$$

Considering that the MPP corresponds to the shortest distance from the origin to the tangent point between the limit state function and the performance function – see Figure 2.10 – and that the vector u^{n+1} is orthogonal to the limit state function, the direction of the gradient vector can be represented by α:

$$\alpha^n = -\frac{u^{n+1}}{\beta^{n+1}} \tag{2.40}$$

and from Equation (2.29):

$$\alpha^n = -\frac{u^n}{\beta^n} \tag{2.41}$$

where α^n is the unit vector of the gradient with the opposite direction to u^{n+1}, which has a magnitude equal to β (or $\| u^{n+1} \|$).

Substituting Equations (2.40) and (2.41) in Equation (2.39) yields:

$$g(u^n) + \nabla g(u^n)(\alpha^n)^{\mathrm{T}}(\beta^n - \beta^{n+1}) = g(u^n) + \| \nabla g(u^n) \| (\beta^n - \beta^{n+1}) = 0 \tag{2.42}$$

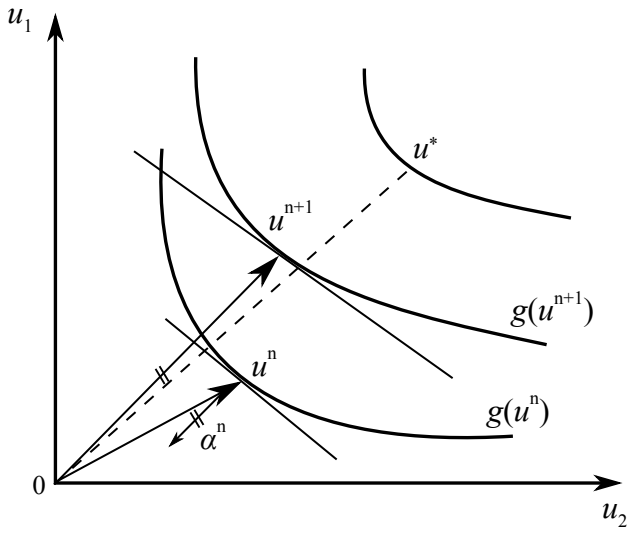

Figure 2.10: Design point search.

Rearranging Equation (2.42) leads to:

$$\beta^{n+1} = \beta^n + \frac{g(u^n)}{\parallel \nabla g(u^n) \parallel} \tag{2.43}$$

Finally, the updated MPP can be computed as:

$$u^{n+1} = -\alpha^n \left\{ \beta^n + \frac{g(u^n)}{\parallel \nabla g(u^n) \parallel} \right\} \tag{2.44}$$

Convergence can be reached when the MPP coordinates do not vary more than a predefined quantity.

After finding the MPP, the limit state function can be written as:

$$G(U) = \sum_{i=1}^{n} \left. \frac{\partial g(U)}{\partial U_i} \right|_{u^*} (U_i - u_i^*) = a_0 + \sum_{i=1}^{n} a_i U_i \tag{2.45}$$

where

$$a_0 = -\sum_{i=1}^{n} \left. \frac{\partial g(U)}{\partial U_i} \right|_{u^*} u_i^* \tag{2.46}$$

and

$$a_i = \left. \frac{\partial g(U)}{\partial U_i} \right|_{u^*} \tag{2.47}$$

in which $g(U)$ is a linear function of standard normal variables with mean, μ_g, equal to a_0 and standard variation equal to:

$$\sigma_g = \sqrt{\sum_{i=1}^{n} a_i^2} \tag{2.48}$$

Then, according to Equation (2.19), the probability of failure can be computed as:

$$P_f = P(G(U) < 0) = \Phi\left(-\frac{\mu_g}{\sigma_g}\right) = \Phi\left(\sum_{i=1}^{n} \alpha_i u_i^*\right) \tag{2.49}$$

Let the vector α_i be:

$$\alpha = (\alpha_1, \alpha_2, \ldots, \alpha_n) = \frac{\nabla g(u^*)}{\parallel \nabla g(u^*) \parallel} \tag{2.50}$$

The probability of failure can be computed as:

$$P_f = \Phi\left(\sum_{i=1}^{n} \alpha_i u_i^*\right) = \Phi(\alpha u^{*\mathrm{T}}) \tag{2.51}$$

By replacing Equation (2.41) in the last equation, the probability of failure can be determined as:

$$P_f = \Phi(-\beta\alpha\alpha^{\mathrm{T}}) = \Phi(-\beta) \tag{2.52}$$

The described process can be summarised in the following steps:

1. select the limit state function G(X);
2. select an initial design point u_0 – usually equal to μ_i;
3. compute the limit state function at u (Equation (2.38));
4. compute the gradient vector (Equation (2.40));
5. calculate a new u^* (Equation (2.44));

6. repeat steps 3 up to 5, until convergence is reached, i.e., when the MPP coordinates do no vary more than a predefined value. If convergence is not reached, the adopted initial design point in step 3 corresponds to the last computed design point in step 5;

7. determine P_f (Equation (2.52)).

When the second order term of the Taylor series is used, the limit state function is approximated by a tangent hypersurface and the method is called Second Order Reliability Method (SORM). Figure 2.11 shows the different approximations from FORM and SORM.

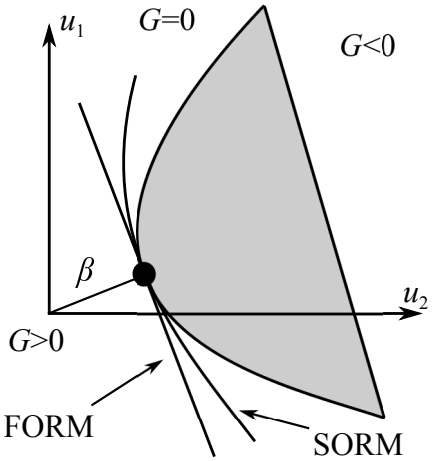

Figure 2.11: Comparison between FORM and SORM.

2.3.3.2 Monte Carlo Simulation (MCS)

The Monte Carlo Simulation (MCS) uses random generation of samples to create a large set of limit state functions. Since the number of failures corresponds to the number of times the limit state function is exceeded, the probability of failure can be computed by (Faber, 2005):

$$P_f \approx \lim_{z \to +\infty} \frac{z_0}{z} \tag{2.53}$$

where z_0 is the number of failures and z is the total number of samples.

Figure 2.12 shows the principle of simulation using a random variable. Firstly, a uniformly distributed random number, z_{ji}, is generated between 0 and 1 for each component of $\hat{x}_j$. Then, the numbers z_{ji} are transformed to $\hat{x}_{ji}$ using:

$$x_{ji} = F_{x_i}^{-1}(z_{ji}) \tag{2.54}$$

where $F_{x_i}()$ is the CDF for the random variable X_i.

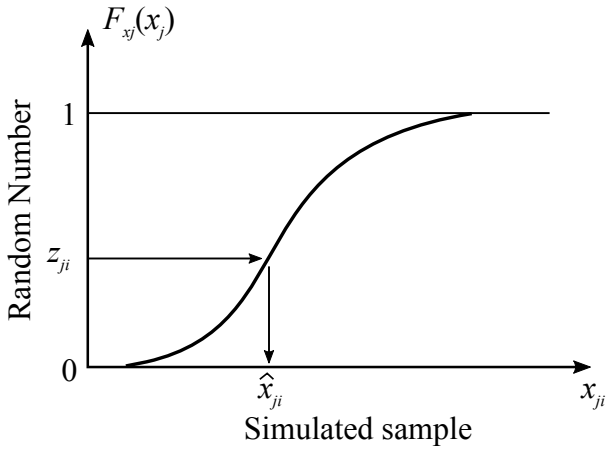

Figure 2.12: Random variable simulation principle (Faber, 2005).

2.3.4 Response Surface Method (RSM)

In the last decades, several computational approaches were proposed for the reliability analysis of implicit functions. The RSM (Bucher, 2009), for instance, is applicable to structural reliability analyses when complex non-linear responses based on finite element models are required. It consists in the construction of response surfaces to describe experiment outcomes through mathematical equations – see Figure 2.13. Two different types of response surface can be considered: i) regression models, such as polynomials or exponentials; or ii) interpolation models, such as polyhedra or radial functions.

2.3.4.1 Response surface construction

A regression analysis is the most commonly used method to perform approximations to data or samples. Typically, lower-order polynomials can be more appropriate for

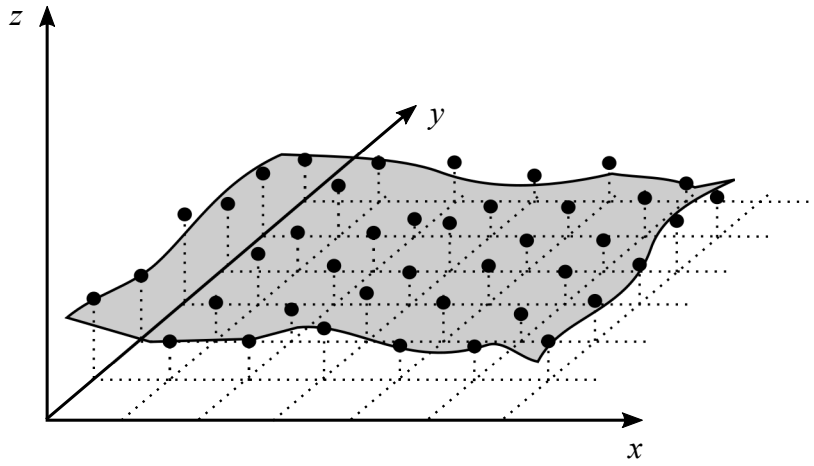

Figure 2.13: Response surface (Bucher, 2009).

small regions with independent variables and reduced curvature, whereas higher-order polynomials can become more suitable for higher curvatures. Higher order responses, however, can lead to multiple co-linearities that must be corrected. In both cases, first- or second-order polynomial models can be used according to the following equation:

$$\hat{y}(x) = p_0 + \sum_{i=1}^{n} p_i x_i + \sum_{i=1}^{n} \sum_{j=i}^{n} p_{ij} x_i x_j \tag{2.55}$$

where $\hat{y}(x)$ is the response surface approach, n is the number of basic variables x_i and p_0, p_i and p_{ij} are the gradients of the response surface in the direction of the respective basic variables x_i and x_j.

The determination of the response coefficients, p_0, p_i and p_{ij}, can be obtained based on the least-squared method:

$$\mathrm{err}(p) = \sum_{k=1}^{n} \left(y(x^k) - \hat{y}(x) \right)^2 \tag{2.56}$$

in which $y(x^k)$ is the exact value of the problem and $\left\{ x^k, k = 1, \ldots, n \right\}$ are fitting points for which the response is constructed.

Rewriting the Equation (2.55) as:

$$\hat{y}(x) = \{1, x_i, x_j\}^{\mathrm{T}} . \{p_0, p_i, p_{ij}\} \equiv \mathbb{Z}^{\mathrm{T}}(x^k).p \tag{2.57}$$

in which the response coefficients can be found through the following optimisation problem:

$$p = \min \left\{ \sum_{k=1}^{n} (y^k - \mathbb{Z}^{\mathrm{T}}(x^k).p)^2 \right\} \tag{2.58}$$

The quality of the determined response can be measured according to the determination coefficient:

$$r^2 = \frac{\sum_{i=1}^{n} (\hat{y}^k - \bar{y})}{\sum_{i=1}^{n} (y^k - \bar{y})} \tag{2.59}$$

where $\bar{y}, y^k$ and $\hat{y}^k$ are the mean, the real and estimated values for each response, respectively. This coefficient ranges between 0 to 1, indicating a poor or a good fit. The adjusted r^2 can be determined by:

$$\bar{r}^2 = 1 - \frac{k-1}{k-p}(1 - r^2) \tag{2.60}$$

where k is the number of responses and p is the number of regression coefficients. The latter equation also varies between 0 and 1. Additionally, when both parameters are close to 1, the model presents a proper fit. On the other hand, if different values are found, some variables can be removed from the models.

2.3.4.2 Set of data

The RSM can require a high computational cost. When a new problem is being defined, the selection of variables should be linked to the influence that each parameter has on the analysis. This deliberation can significantly reduce the size of the problem, since a high number of variables increases the computational cost. The number of responses depends on the adopted polynomial, and for the first- or second-order polynomials, it can be respectively estimated according to:

$$N_1 = 1 + n \tag{2.61}$$

and

$$N_2 = 1 + n + \frac{n(n+1)}{2} \tag{2.62}$$

where n is the number of random variables, $\{p_i, i = 1, \ldots, n\}$.

The response surface can be generated based on support points obtained from:

$$x_i = \mu_i \pm k\sigma_i \tag{2.63}$$

where x_i are the support points, μ_i is the mean value of the variable i^{th}, k is an arbitrary factor used to define the region, usually considered as unitary, and σ_i is the standard deviation of the variable i^{th}.

Figure 2.14 shows an example of support points definition for two variables. For each random variable, two support points are generated from the central one by adding or removing the distance σ. Thus, for two variables, four support points are generated and five points in the total are considered for the response.

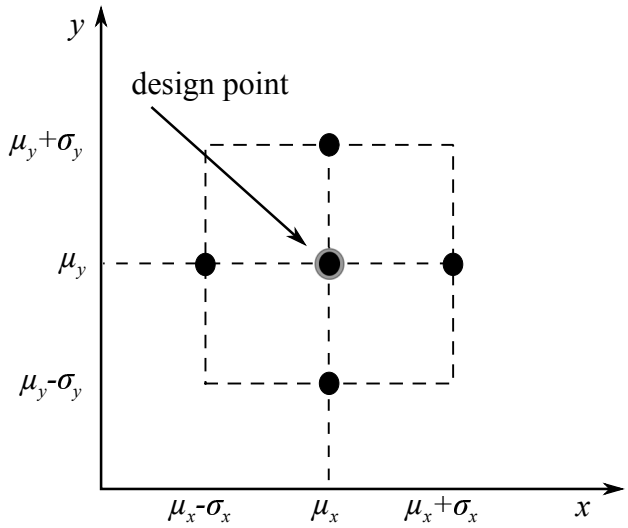

Figure 2.14: Central design point and support points.

2.3.4.3 RSM algorithm

In the case of structural reliability that considers a limit state function, $g(X)$, according to $g(X) = R(X) - S(X)$, where R is the resistance, S is the load effect and

X is a vector including all random variables, the response surface can be generated for the limit state function or separately for each component.

In general, the implementation of RSM for a reliability analysis can be described as (Haldar and Mahadevan, 2000):

1. define the relevant variables to evaluate the limit state function $g(X)$;
2. define the number of support points according to Equations (2.61) or (2.62), depending on the polynomial order;
3. determine the support points according to Equation (2.63). In the first iteration these are obtained around the mean values of the variables;
4. run deterministic analysis for all the sets of random variables defined in step 3 and compute the final results, $y(x_i)$;
5. construct the response surface based on the results from the previous step, $\hat{y}(x_i)$; a regression analysis is performed considering a first- or second-order polynomial (Equation (2.58));
6. check the accuracy of the response (Equation (2.59));
7. use FORM with the latter generated equation to calculate the probability of failure, P_f, and the new design points.

In reliability analysis, steps 3 to 7 are repeated until the coordinates of the design point converge, according to the tolerance criterion. After the first iteration, step 3 always defines the support points based on results from step 7.

2.3.5 Time-dependent reliability

In general, both resistance and load variables will vary over time and this can usually be described by a stochastic process – see Figure 2.15. In time-dependent reliability,

the probability of failure corresponds to the probability of the limit state function being violated for the first time for each time increment (Faber, 2005):

$$P_f(t) = P[R(t) \leq S(t)], \forall (t \in [0 - t_L]) \tag{2.64}$$

where $[0, t_L]$ is the time interval of interest and both random variables are a function of time.

For each period of time, t, the PDF of each realisation is considered, $f_R(t)$ and $f_S(t)$. Thus, the probability of failure, $P_f(t)$, can be computed from Equation (2.14) through the interaction of: F_R and f_S, at each time interval, as shown in Figure 2.15. Over time, the probability of failure may increase caused by the growth interaction between resistance and loads.

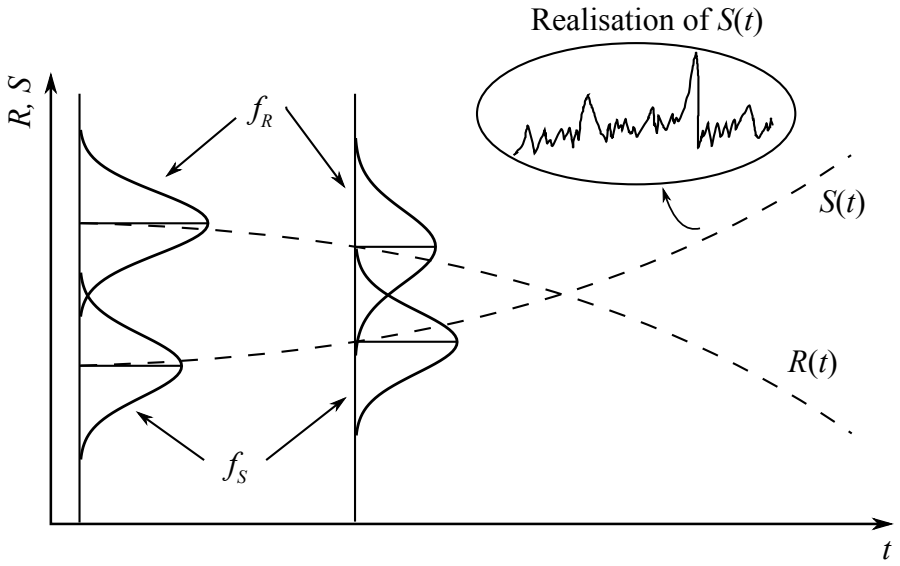

Figure 2.15: Time-dependent reliability problem (Melchers, 1999).

2.3.6 Reliability assessment of existing structures

The assessment of existing structures often involves field inspections, information collection and assessment; and decision making (Melchers, 1999). The structural assessment might be supported by modern reliability theory methods that can work as a powerful tool for rational decisions. There are several reasons that can lead to

the need of reliability assessments, as for instance the change of the structural use, or possible issues concerning project errors or material quality (Ellingwood, 1996). For this purpose, appropriate models are needed to describe the strength and actions on structures. Also, proper load models are needed to predict the actual or expected structural behaviour, considering that for assessment purposes, conservative models results in higher costs than for similar cases in the design phase (Melchers, 1999). The uncertainties present in existing structures, not only in resistances or loads, but also on the undergoing repair or even in the inspection process, are another topic that need to be taken into account.

The assessment of existing structures for rehabilitation purposes using reliability tools differs from a new one in various aspects, including: i) the cost of increasing safety levels, that are higher for existing structures, ii) the remaining lifetime for existing structures that is lower than for new structures; and iii) the potential uncertainties present in existing structures.

For existing structures, reliability assessment considers the following steps (Faber, 2005):

1. prior formulation of uncertainty models;
2. development of limit state functions;
3. definition of probabilistic models;
4. decision analysis;
5. setting acceptable levels for the failure probability and choice of an acceptable target reliability index.

The reliability assessment of existing structures may work as a tool to optimise policies of repair or upgrade, minimising costs over structural lifetime. Figure 2.16 shows an example of the computed probability of failure over time of a structure. This type of analysis may help the decision process to evaluate when the estimated reliability level reaches the acceptable minimum. Decisions, such as closure, repair or reduction of load level can be taken. As structures become older, reassessments and therefore decision making processes are preformed more frequently.

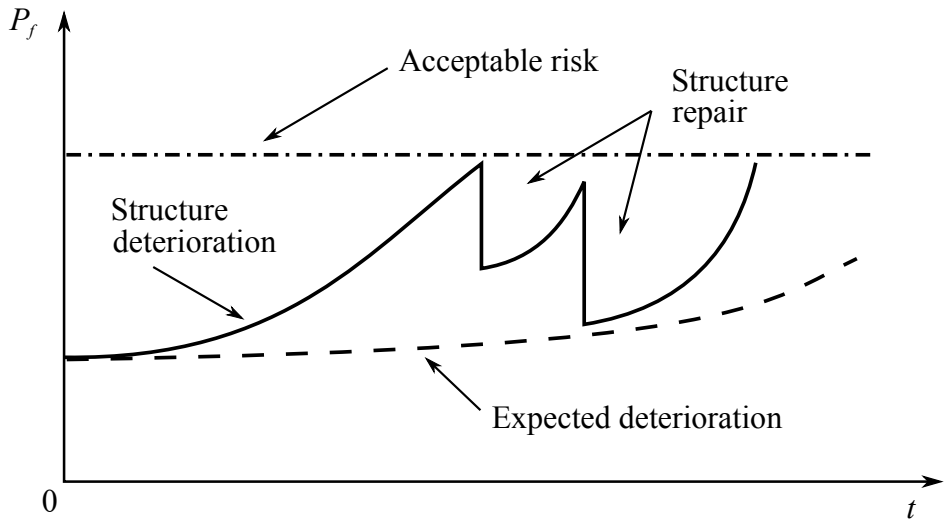

Figure 2.16: Reliability and assessment over time (Melchers, 1999).

2.3.7 Reliability of structural systems

System structural reliability is used whenever structures can be split into segments and its individual or combined failures can lead to the whole structure failure, or when there are several limit states, e.g., bending, shear or deflection that can be considered for each area (Schneider, 1997). There are two fundamental types of systems in reliability analysis, as shown in Figure 2.17. In the first case, segments are connected in series and whenever the weakest segment fails, the whole chain fails. Thus, the reliability is defined by the weakest segment. On the other hand, in a parallel system, failure occurs when all segments fail, and therefore reliability depends on all segments.

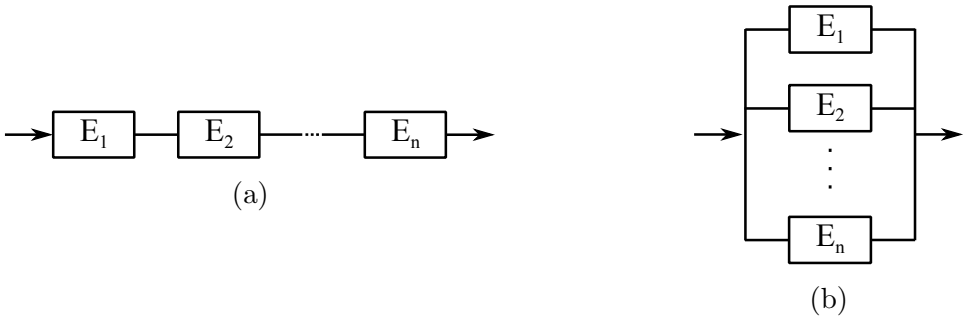

Figure 2.17: System reliability: (a) series; and (b) parallel.

When all segments are statistically independent, the probability of failure of series

and parallel systems, are respectively:

$$P_f = 1 - \prod_{i=1}^{n}(1 - p_{fi}) \tag{2.65}$$

$$P_f = \prod_{i=1}^{n} p_{fi} \tag{2.66}$$

where p_{fi} is the probability of failure of the i^{th} segment.

On the other hand, when segments are considered completely correlated, the probability of failure of series and parallel systems are respectively:

$$P_f = max[p_{fi}] \tag{2.67}$$

$$P_f = min[p_{fi}] \tag{2.68}$$

in which p_{fi} is the probability of failure of the i^{th} segment.

Therefore, the probability of failure for series and parallel systems falls within the following limits:

$$max[p_{fi}] \leq P_f \leq 1 - \prod_{i=1}^{n}(1 - p_{fi}) \tag{2.69}$$

$$\prod_{i=1}^{n} p_{fi} \leq P_f \leq min[p_{fi}] \tag{2.70}$$

For a series system, Ditlevsen (1979) proposed narrower bounds by taking into account the correlation between the segments, as:

$$max[p_{fi}] + \sum_{a=2}^{n} max\left(p_{f_a} - \sum_{b=1}^{a-1} p_{f_a} \bigcap p_{f_b}; 0\right) \leq P_f \leq \sum_{a=1}^{n} p_{f_a} - \sum_{a=2,b<a}^{n} max(p_{f_b} \bigcap p_{f_a}) \tag{2.71}$$

In the previous equation, the lower bound accounts for individual probabilities, p_{fa} and all possible joint probabilities involving two segments, i.e., $p_{f_a} \bigcap p_{f_b}$. The joint probabilities involving more than two segments are neglected as simplification. The

upper bound includes also the individual and joint probabilities, where failure events are ordered from the highest probability of failure to the lowest.

The joint probabilities are calculated using the integral of the bivariate normal distribution function:

$$P(p_{f_1} \bigcap p_{f_2}) = \int_{\beta_1}^{\infty} \int_{\beta_2}^{\infty} \frac{1}{2\pi\sqrt{1-\rho_{sys_{ab}}^2}} e^{-1/2(1-\rho_{sys_{ab}}^2)(\beta_a^2\beta_b^2 - 2\rho_{sys_{ab}}\beta_a\beta_b)} d\beta_a d\beta_b \tag{2.72}$$

where $\rho_{sys_{ab}}$ is the correlation factor between segments a and b.

The correlation coefficient, $\rho_{sys_{ab}}$, between two segments (see Figure 2.18) corresponds to the cosine of reliability vectors associated with a and b. The direction cosines gives the contribution of each random variable to the reliability vector. Thus, the correlation can be computed from:

$$\rho_{sys_{a,b}} = \frac{Cov(a,b)}{\sigma_a \sigma_b} = \sum_{k=1}^{n} \alpha_{ak}^* \alpha_{bk}^* \tag{2.73}$$

where α_{ak}^* is the direction cosine at the MPP of failure and evaluates the contribution of a over the segment k.

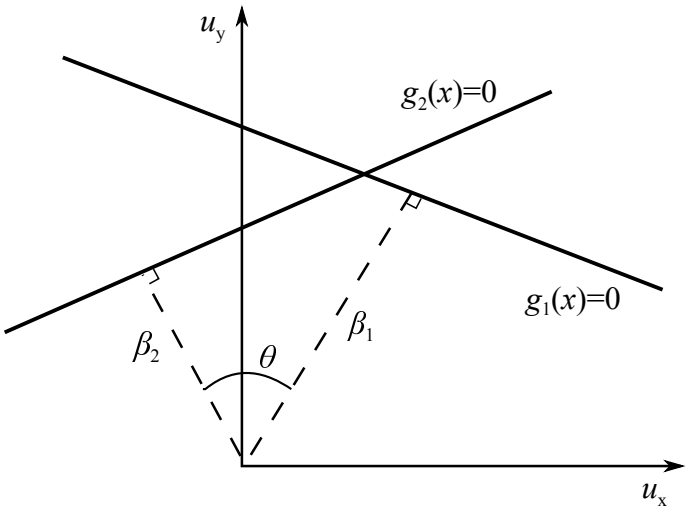

Figure 2.18: Possible correlation between two segments (Estes, 1997).

The system correlation matrix between each segment can be computed according to:

$$\rho_{sys} = \begin{bmatrix} \rho_{sys_{11}} & \rho_{sys_{12}} & \cdots & \rho_{sys_{1z}} \\ \rho_{sys_{21}} & \rho_{sys_{22}} & \cdots & \rho_{sys_{2z}} \\ \vdots & \vdots & \ddots & \cdots \\ \rho_{sys_{z1}} & \rho_{sys_{z2}} & \cdots & \rho_{sys_{zz}} \end{bmatrix} \tag{2.74}$$

Finally, the reliability of the system, β_{sys}, can be estimated as the average between upper and lower bounds of the Ditlevsen (1979) bounds:

$$\beta_{sys} = \frac{\beta_{lower} + \beta_{upper}}{2} \tag{2.75}$$

Although, structural systems are frequently more complex in most cases and can be simplified into series or parallel systems to compute the reliability, as seen in Figure 2.19.

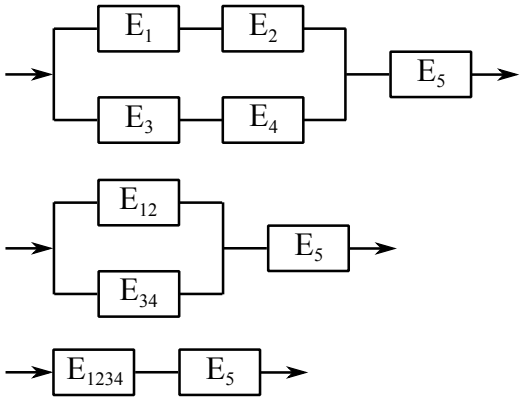

Figure 2.19: Mixed system.

2.4 Structural design codes

The main objective of a design code is to ensure safety and serviceability of structures during a predefined period of time, while keeping costs acceptable (Schneider, 1997). Designers are required to follow codes to validate the design, although having the freedom to determine the main structural aspects. Currently, any upgrade of existing guidelines or the development of new codes, is an extremely complex issue;

more than addressing the structural safety, it concerns the national economy and competitiveness. Any changes should be introduced gradually to prevent operating issues by users (Melchers, 1999).

'Probabilistic' design codes adopt statistical tools that are not yet generally employed by designers, given their restrictions and insufficient available data. As a practical approach, the design codes propose partial safety factors (or reduction factors) that have been previously derived from probabilistic data, allowing designers to consider implicitly the uncertainties in loads, materials or models. Thus, codes allow risk control to a certain level when good engineering practice is observed (Melchers, 1999).

2.4.1 Probability-based codes

Since earlier stages, structural engineers have always approached problems considering the existing risk. In the late 19^{th} century, engineers relied on the allowable stress design method by comparing elastic stresses in members due to service loads with specific allowable stress reduced by a safety factor (Ellingwood, 2000):

$$f \leq \frac{F}{FS} \tag{2.76}$$

where f is the allowable stress, F is the elastic stress and FS is the factor of safety.

The adopted safety factors were based on previous experience and neglected uncertainties. Over the years, semi-probability limit states design codes have been developed all over the world. In the United States of America, the Load and Resistance Factor Design (LRFD) format code was developed between the 1940s and 1960s (Ellingwood, 1994). This code has the following form:

$$\phi R_n \geq \sum_{k=1}^{i} \gamma_k S_{km} \tag{2.77}$$

where ϕ is the resistance factor, R_n is the nominal resistance, γ_k is the load factor and S_{km} is the nominal load. The former factors reflect the uncertainties in resistances and the consequences of failures associated with the reliability index (Ellingwood,

2000).

The LRFD was calibrated so that the probability of a particular event is reasonable small, whereas the load and resistance factors were calibrated such that a wide range of designs could be close to the target reliability.

A similar approach is adopted in the National Building Codes from the Canadian Standards Association (CSA), following the subsequent form:

$$\phi R \geq g_s \left[\gamma_D D_n + \Psi \left(\gamma_L L_n + \gamma_W W_n + \gamma_T T_n + \dots\right)\right] \tag{2.78}$$

where ϕ is the partial factor for the resistance R, γ_x are the partial safety factors applied to several nominal loads, such as dead load D_n, live load L_n or wind load W_n and Ψ is the load combination factor that considers the reduced probability that the dead load, live load and wind load reach its nominal values simultaneously.

As the LFRD code, this one combines the member strength and geometrical errors in a single factor ϕ, making it simpler for the designer. Nevertheless, it may not be the most suitable for structures composed by different materials (Melchers, 1999).

The European Committee for Standardisation (CEN) establishes the basis of all European structural design codes, according to the following format:

$$g_R\left(\frac{f_1}{\gamma_{m_1}}; \frac{f_2}{\gamma_{m_2}}; \dots; \frac{f_k}{\gamma_{m_i}}\right) \geq g_S\left(\gamma_{f_1} Q_1; \gamma_{f_2} Q_2; \dots; \gamma_{f_i} Q_k\right) \tag{2.79}$$

where g_R and g_S are the resistance and load functions, f_k and Q_k are the characteristic values for materials strength and loads; and γ_{mi} and γ_{fi} are the partial factors for materials and loads respectively.

The former code generally considers as the characteristic values for materials the 5^{th} percentile. Moreover, different materials and loads are treated independently, by different partial safety factors. The material partial safety factor has into account possible strength deviations from the characteristic values, possible defects and inaccurate assessments. On the other hand, the partial factor of loads has into account potential deviations from characteristic values or possible errors in load definition.

The main objective of a reliability based code calibration is the optimisation of

partial safety factors, γ_i, given by:

$$\gamma_R = \frac{r_k}{r_d} \qquad \text{for resistance-type random variable,} \tag{2.80}$$

$$\gamma_S = \frac{s_d}{s_k} \qquad \text{for loading-type random variable,} \tag{2.81}$$

where r_d and s_d are the design values of the random values – used to perform the structural design – and r_k and s_k are the characteristic values, for resistances and loads respectively.

For a given set of partial safety factors, the reliability index is evaluated according to a defined limit state function. Then, partial safety factors can be calibrated through the following optimisation problem Gayton et al. (2004):

$$\min_{\gamma_i}(\gamma_i) = \sum_{j=1}^{L} \left(\beta_j(\gamma_i) - \beta_t\right)^2 \tag{2.82}$$

where β_t is the target reliability index.

2.4.2 Code calibration procedure

The optimisation procedure of the best set of partial safety factors may have different approaches. Nonetheless, the main steps are common to all – see Faber and Sorensen (2002) or Gayton et al. (2004) – and consist on the following:

Step 1 - Study domain definition

The class of structures and the failure modes are defined at this stage, including the scope and aims of the code. The type of structures (e.g., residential buildings) or materials (e.g., concrete) have to be prescribed. This step is important since it is impossible to develop just one structural code to all design situations.

Step 2 - Code objective characterisation

The code objective may be defined based on an expected target reliability index. Modern design codes, such as the Eurocodes (CEN, 2002a) or the

American Concrete Institute (ACI) codes (ACI Committee 222, 2001), have set an objective safety level defined by the target reliability index, β_t (Schneider, 1997). The ideal way to define this parameter is by solving an optimisation problem having into account the consequences of each type of failure and cost per live saved (JCSS, 2001). Cost-benefit-risk analysis may be done to establish upper and lower bounds on acceptable levels, having into account social and political status (Melchers, 1999). The target reliability indices for ULS present in CEN (2002a) and JCSS (2001) are summarised on Tables 2.2 and 2.3, respectively. It should be highlighted that these values are defined for the design of new structures.

Table 2.2: Target reliability indices for ULS from CEN (2002a).

Reliability level	Minimum reliability indices	
	1 year reference period	50 years reference period
High consequences in terms of economical, social and environmental	5.2	4.3
Medium consequences in terms of economical, social and environmental	4.7	3.8
Low consequences in terms of economical, social and environmental	4.2	3.3

Table 2.3: Target reliability indices for ULS related to one year reference period from JCSS (2001).

Relative cost of safety measure	Minor consequences of failure	Moderate consequences of failure	Large consequences of failure
Large	3.1	3.3	3.7
Normal	3.7	4.2	4.4
Small	4.2	4.4	4.7

Setting a target reliability index for rehabilitated structures is not simple. Unlike for new structures, conservative rules for assessing existing structures are usually very expensive, leading to the remaining question of what should be the accepted failure probability for this type of structures (Melchers, 1999;

Steenbergen and Vrouwenvelder, 2010). On the other hand, similar to new structures, human life limits and economical issues are fundamental factors to set reliability indices. For repaired structures, reliability indices can be determined as (Allen, 1991; Steenbergen and Vrouwenvelder, 2010):

$$\beta_r = \beta_n - \Delta\beta \tag{2.83}$$

where β_n is the reliability of new structures and $\Delta\beta$ is a reduction coefficient applied to existing structures.

Steenbergen and Vrouwenvelder (2010) suggested values of 0.5, based on an economic optimisation study for existing structures, whereas Allen (1991) suggested that this coefficient could be adjusted according to the sum of several assessment factors, depending on: i) inspections performance, ii) system behaviour; and iii) risk category. Although, further studies are needed to support the choice of this coefficient.

Step 3 - Design situations construction

Representative design models of the whole study domain (step 1) are selected. Basic variables, such as span length, cross-sectional areas, material properties or applied loads are defined to create the design space.

Step 4 - Limit state functions definition

The limit state functions and probabilistic models are defined. For each limit state, a different function is established. For instance, in the case of concrete girders, limit state functions for shear or bending strength can be used. Additional, real models that have into account the non-linear structural behaviour are preferred rather than conservative elastic models.

Step 5 - Reliability computation

For each design situation (step 3) and limit state function (step 4), the reliability index is determined using an appropriate method, such as FORM, to compute partial safety factors for each random variable. Following Section 2.3.3.1, the transformation of variables can be written as (Melchers, 1999):

$$x_i^* = F_{x_i}^{-1}\left[\Phi(u_i^*)\right] = \mu_{X_i}(1 - \alpha_i\beta_c V_{X_i}) \tag{2.84}$$

with the design point coordinates equal to $x_i^* = \mu_{x_i} - \alpha_i \beta \sigma_{x_i}$. Thus, the limit state function can be described as:

$$G(x^*) = G\left\{F_X^{-1}\left[\Phi(u^*)\right]\right\} = G\left[\mu_{X_i}\left(1 - \alpha_i \beta_C V_{X_i}\right)_{i=1,\ldots,n}\right] = 0 \tag{2.85}$$

where $X_i, i = 1, \ldots, m$ are the resistance variables. Then, by converting the means to the characteristic values by considering that $R_k = \mu_R(1 - k_R V_R)$, the second part of Equation (2.84) becomes:

$$x_i^* = \mu_{X_i}(1 - \alpha_i \beta_C V_{X_i}) = \frac{1 - \alpha_i \beta_C V_{X_i}}{1 - k_{X_i} V_{X_i}} x_{ki} \tag{2.86}$$

in which k_{X_i} is the characteristic fractile coefficient of the normal distribution and the partial safety factor of the resistance random variables, γ_{mi}, is defined according to:

$$x_i^* = \frac{x_{ki}}{\gamma_{mi}} \tag{2.87}$$

On the other hand, the partial safety factor of the load random variables, γ_{fi}, can be computed according to:

$$x_i^* = \mu_{X_i}(1 - \alpha_i \beta_C V_{X_i}) = \frac{1 - \alpha_i \beta_C V_{X_i}}{1 + k_{X_i} V_{x_i}} x_{ki} = \gamma_{fi} x_{ki} \tag{2.88}$$

When the limit state function is linear and just one load case is considered, the described procedure can be defined by using the following limit state function (Melchers, 1999):

$$G(X) = Z = R - S \tag{2.89}$$

with

$$\mu_Z = \mu_R - \mu_S \tag{2.90}$$

and

$$\sigma_Z = \sqrt{(\sigma_R^2 + \sigma_S^2)} \tag{2.91}$$

where R corresponds to the random structural resistance and S to the load demand, respectively, μ is the mean and σ is the standard deviation. Then, according to Equation (2.18), the reliability index, β_C can be associated with

μ and σ through:

$$\mu_Z = \mu_R - \mu_S \geq \alpha\beta_C(\mu_R V_R + \mu_S V_S) \tag{2.92}$$

where α is a factor used to linearised the limit state function and V are the coefficients of variation.

The characteristic safety factors can be computed as:

$$\lambda_k = \frac{R_k}{S_k} = \frac{\mu_R(1 - k_R V_R)}{\mu_S(1 + k_S V_S)} \tag{2.93}$$

so that

$$\frac{R_k}{S_k} \geq \frac{(1 - k_R V_R)}{(1 - \alpha\beta_C V_R)} \frac{(1 + \alpha\beta_C V_S)}{(1 + k_S V_S)} \tag{2.94}$$

or

$$R_k \geq \gamma_R \gamma_S S_k \tag{2.95}$$

where γ_R and γ_S are the partial safety factors for random resistance and load. The latter factors correspond to the inverse of LFRD factors ($\phi = 1/\gamma$).

Step 6 - Optimisation of the partial safety factors

The calibration of partial safety factors is performed through an optimisation problem to minimise the deviation of the code from the objective. In safety-checking format codes, the partial safety factors should assume constant values for several design situations aiming at simplifying the design procedure. Thus, some deviation of the expected reliability index are acceptable. The least-squares method is commonly used to determine the error in the target reliability according to Equation (2.82). Moreover, it is possible to propose just one partial safety factor or supplementary factors that have into account more than one specification, e.g., environmental exposures or costs.

Chapter 3

Statistical characterisation of composite properties

3.1 Introduction

Fibre reinforced polymers (FRP) are considered as a practical material of strengthening or repairing existing RC structures. When compared with other materials, such as steel or concrete, FRP has unique properties and advantages that make this material more attractive in rehabilitation. In fact, FRP usage in construction has grown very significantly over the last decades, and therefore still continues to be subject to intensive research. Moreover, to enable a sustained growth and to provide confidence to structural engineers, structural reliability studies that help to support safety-checking format codes are needed.

As briefly presented in the previous chapter, reliability analysis have into account the uncertainties that may arise during the construction and use of a structure, including in material properties. Thus, a statistical description of material properties that considers the existing variability is fundamental. In this chapter, a statistical analysis of the most significant mechanical properties of CFRP laminates is described, namely the Young's modulus, the tensile strength and the ultimate strain. The proposed models were developed within the scope of reliability analysis, which

require statistical descriptions of the material variability, in particular regarding the extreme values. Existing works developing probabilistic models for CFRP properties have been performed using small samples, e.g., Atadero (2006) or Zureick et al. (2006), reason why it becomes difficult to propose reliable models. Therefore, the aim of this chapter is to present a statistical analysis of a large homogeneous batch of test specimens, in this case pultruded pre-cured laminates of carbon fibres and vinylester matrices commonly used in civil engineering commercial applications.

In the following, a bibliographic review of FRP as a strengthening material for concrete structures is presented. Firstly, in Section 3.2, a review of the mechanical properties of FRP is performed. Afterwards, Section 3.3 addresses the use of FRP in RC structures and Section 3.4 presents the statistical study, including: a review of the previous studies on the development of probabilistic models for FRP, the description of all data and experimental tests used for this study; and the statistical and correlation analysis. Lastly, the main conclusions are summarised in Section 3.5.

3.2 Fibre reinforced polymers

Fibre reinforced polymers (FRP) are composite materials in which a polymeric matrix is reinforced with fibres, as shown in Figure 3.1 (a). The polymeric matrix allows fibres to act together as if a single element. On the other hand, fibres help withstanding the applied load. When isolated, fibres show higher stiffness and lower ultimate strain than matrix, as illustrated in Figure 3.1 (b). When both fibres and matrix are combined, the resulting composite material has lower stiffness than the fibres, but still shows roughly the same ultimate strain. The FRP composite also shows elastic behaviour until failure, without any region of plastic deformation (ACI Committee 440, 1996; Leeming and Hollaway, 1999).

3.2.1 Matrix

The matrix protects fibres from abrasion, chemical, mechanical and environmental agents and, at same time, binds fibres together in the desired arrangement. It also

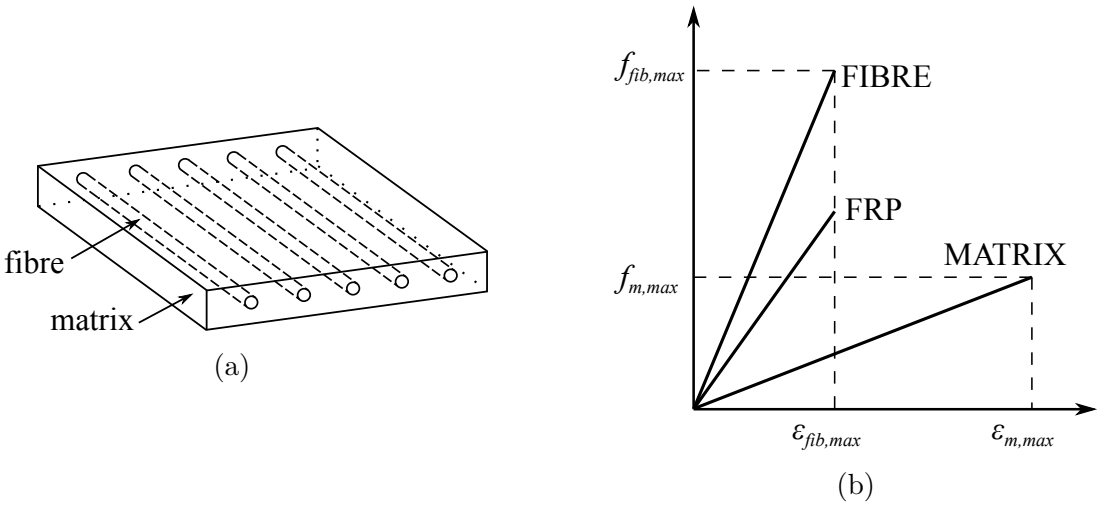

Figure 3.1: Composite components: (a) general layout; and (b) stress vs. strain for fibre, matrix and FRP composite (CNR, 2013).

allows stresses to be transferred between fibres and structure (ACI Committee 440, 1996; CEB/FIB, 2001).

The matrices can be made of several types of resins, including polyester, vinylester or epoxy. The polyester resins are the most economical and easy to handle due to low viscosity and fast curing time. The vinylester resins have similar handling and performance characteristics, and show better corrosion and chemical resistance. Additionally, the epoxy resin, very popular on other areas, such as aerospace engineering, present a good performance characterised by a good resistance to humidity, chemical agents and very good adhesive properties (ACI 440, 2008; ACI Committee 440, 1996; CEB/FIB, 2001; CNR, 2013).

3.2.2 Fibres

Fibres are small filaments with 5-20 µm of diameter. The most important role of fibres is to provide the composite with the necessary stiffness and resistance to carry the applied load. In civil engineering industry, the most commonly used fibres are made of glass, aramid and carbon, as shown in Figure 3.2 (ACI 440, 2008; CEB/FIB, 2001; CNR, 2013).

(a) (b) (c)

Figure 3.2: Types of fibres: (a) glass, (b) aramid; and (c) carbon (Bikeoff Design Resource [online]).

Glass fibres is the most common fibre used in composites and is relatively inexpensive when compared with other fibres. The disadvantages are the lower Young's modulus and resistance to humidity and alkalinity. The two most common glass fibres are either E-glass or S-glass. Zircon is typically added to protect from the cement-alkali reaction (CNR, 2013; Leeming and Hollaway, 1999).

Aramid fibres are organic, fire resistant and exhibit good toughness and fatigue characteristics. Under compression the behaviour is non-linear and ductile. The disadvantages are related with sensitivity to moisture and ultraviolet radiation (CEB/FIB, 2001; CNR, 2013).

Carbon fibres are characterised by having a high Young's modulus and strength. Actually, these fibres have the largest failure strength when compared with glass or aramid fibres, and are brittle and less sensitive to creep. On the other hand, the main disadvantage is related with the energy requirements for its production and cost. Table 3.1 summarises the typical mechanical properties for all described fibres (CNR, 2013; Leeming and Hollaway, 1999).

3.2.3 Resulting composite

The behaviour of the resulting composite depends on the properties of the fibres and matrix, as well as on the relative proportion. In the scope of civil engineer-

Table 3.1: Mechanical properties of fibres (CEB/FIB, 2001).

Fibre	Young's modulus (GPa)	Tensile strength (MPa)
Glass		
E	70	1900-3000
S	85-90	3500-4800
Aramid		
Low modulus	70-80	3500-4100
High modulus	115-130	3500-4000
Carbon		
High strength	215-235	3500-4800
Ultra high strength	215-235	3500-6000
High modulus	350-500	2500-3100
Ultra high modulus	500-700	2100-2400

ing applications, the main advantages of FRP composites are the low weight, the high ultimate strength, the corrosion resistance and the ease of transportation, handling and application. In addition, the composite material also acts as a layer of environmental and corrosion protection, as well as concrete cracking control. On the other hand, the main disadvantages are the reduced ductility stemming from the linear elastic and the vulnerability to impact, vandalism and fire damage. The susceptibility to moisture, temperature and ultraviolet rays exposure are also drawbacks. In terms of environment impact, composites are not recyclable (CEB/FIB, 2001; CNR, 2013; Leeming and Hollaway, 1999). Table 3.2 presents the typical mechanical properties of glass, aramid and carbon reinforced polymers.

Table 3.2: Mechanical properties of composites of FRP laminates (fibres volumes from 40% to 60%) (ACI 440, 2008).

Resin	Young's modulus (GPa)	Tensile strength (MPa)
Glass FRP (GFRP)	20-40	520-1400
Aramid FRP (AFRP)	48-68	700-1720
Carbon FRP (CFRP)	100-140	1020-2080

For in-situ applications, two systems of FRP EBR can be used – see Figure 3.3. The first is designated by wet lay-up system and consists in the directly application of fibre sheets saturated with resin. This method, requires high skills from the worker

and good measures of quality control, since the FRP is made directly at the repair site. The second, known as prefabricated system, is based on the use of fabricated cured strips (CEB/FIB, 2001). It is based on pultrusion and lends itself to industrial automatisation. This process can be used to produce FRP reinforcing bars, profiles or laminates with a wide variety of shapes, thickness and sizes (CEB/FIB, 2001; Leeming and Hollaway, 1999).

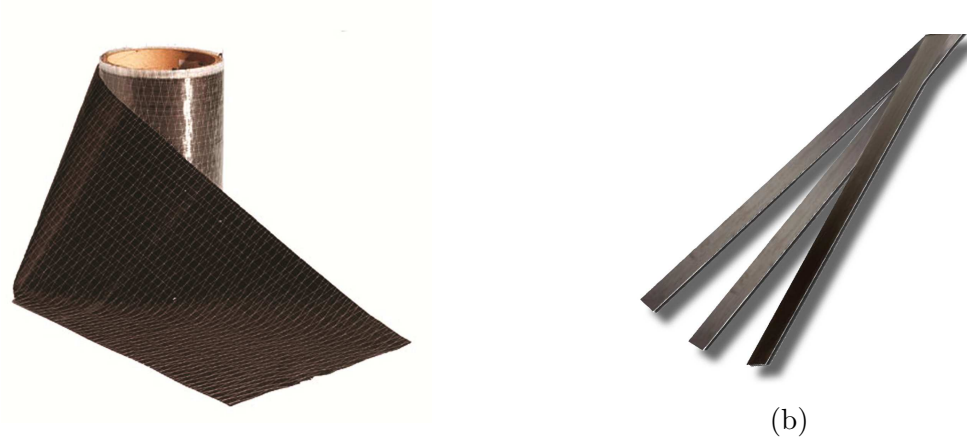

(a) (b)

Figure 3.3: FRP EBR: (a) sheets; and (b) laminates (G&P intech s.r.l [online]).

The application of FRP laminates requires the use of chemical adhesives to assure adequate bond continuity of shear stresses between concrete and FRP. The most used bonding agents are epoxy based – typical properties are shown in Table 3.3. The main advantages of epoxy adhesives over other polymers are low shrinkage and creep, the high cured cohesive strength, good wetting properties and the time available after the adhesive application and before both parts are joined together. On the other hand, the main disadvantages are related with the slow curing, limited performance on plastics and its two-component form (Handbook-MIL 17, 2002).

Table 3.3: Typical epoxy adhesives properties (ISIS, 2007).

Property	Range
Specific gravity	1.20-1.30
Tensile strength (MPa)	55.0-130.0
Young's modulus (GPa)	2.75-4.10
Cure shrinkage (%)	1.0-5.0

3.3 FRP as a strengthening material in RC beams

The maintenance of RC structures is one of the many problems faced by engineers. Several reasons may lead to the need for repairing or upgrading RC structures, such as corrosion of reinforcements, deterioration of concrete, damages due to explosions, fire or crashes, as well as changes in structural use or design errors. In this scope, the FRP can be used to repair or upgrade structures.

FRP have been applied in all types of structures for strengthening or retrofitting purposes, given its properties discussed earlier. It can be used to increase both flexural and shear capacities of concrete members. The EBR technique used with sheet or prefabricated laminates is one of the approaches available (see illustration in Figure 3.4) (CEB/FIB, 2001; Leeming and Hollaway, 1999).

(a) (b)

Figure 3.4: FRP application process of: (a) sheets (CEB/FIB, 2001); and (b) prefabricated laminates (Leeming and Hollaway, 1999).

The application of EBR typically comprises two stages: i) surface preparation; and ii) the application of the FRP, which should include a final quality control check for defects and/or imperfections. The proper application of the FRP requires prior surface preparation to attain the necessary bonding properties. This can be done by high pressure water jetting, grit blasting, scabbling or grinding. After this process, the surface has to be cleaned from oils and coatings and, after inspection, the FRP has to be also cleaned to ensure a good bond adhesion. The adhesive mixture has to be prepared taking into account the environmental conditions and can be applied by hand trowel and should reach a constant thickness. The laminates or

wet lay-up sheets are bonded to the structure using hand pressure (Leeming and Hollaway, 1999). After the strengthening, visual inspections have to be performed to check possible signs of cracking, crazing, delamination or any other local damage that could induce a premature failure. The FRP itself typically does not require maintenance during its lifetime (TR-55, 2000).

The strengthening of RC girders using FRP – see Figure 3.5 – has been used on numerous occasions due to its advantages, namely the speed of application and the minor impact it can have on the normal use of traffic infrastructures.

Figure 3.5: Overall view of a concrete beam FRP strengthened on a bridge at Dresden, Germany (Handbook-MIL 17, 2002).

Flexural strengthening can be achieved using FRP laminates or wet lay-up sheets, and the extremities can be left unanchored, or anchored using steel plates, FRP sheets or fabrics as represented in Figure 3.6. There are also prestressed solutions available. The composite can improve the stiffness and strength of the girder, having some resemblances with the purpose of ordinary steel reinforcement.

RC beams strengthened with FRP for bending moments can have three significant failure modes, which can be triggered independently or in combination: i) flexural failure, that takes place when the maximum tensile strain of FRP or concrete

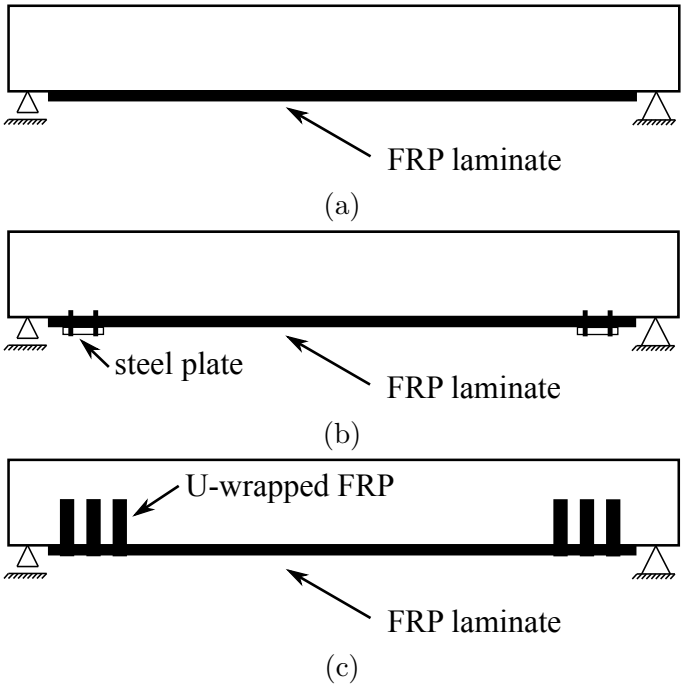

Figure 3.6: FRP flexural strengthening of RC beams: (a) unanchored arrangement, (b) anchored system using steel plates; and (c) anchoring system using U-wrapped sheets.

compressive strain are reached, or when a major intermediate crack causes FRP debonding (see Figure 3.7 (a-c), ii) end anchorage peel due to inappropriate bond or high shear stresses at the bond zone (see Figure 3.7 (d-e)); and iii) shear crack peel given to concrete cracking that cause FRP concrete separation (see Figure 3.7(f-g)) (Leeming and Hollaway, 1999). The adhesive used and eventually the selection and design of an anchoring system can be critical to avoid premature failures due to FRP debonding. Moreover, it should be highlighted that the quality of bond depends primarily on the workmanship and less on the material reliability.

The typical flexural response of a RC beam strengthened with FRP is illustrated in Figure 3.8. The first two significant stages in the overall behaviour are, respectively, the onset of concrete cracking and, later on, the onset of yielding for the flexural reinforcement. Afterwards, the beam can fail by one of the described failure modes. In the case of FRP intermediate crack debonding, plate end debonding, end peeling due to shear force or concrete cover separation, a sudden drop in the load carrying capacity to a residual strength is observed, followed by concrete crushing. If none of these failure modes occurs, the load continues to increase until the beam fails by

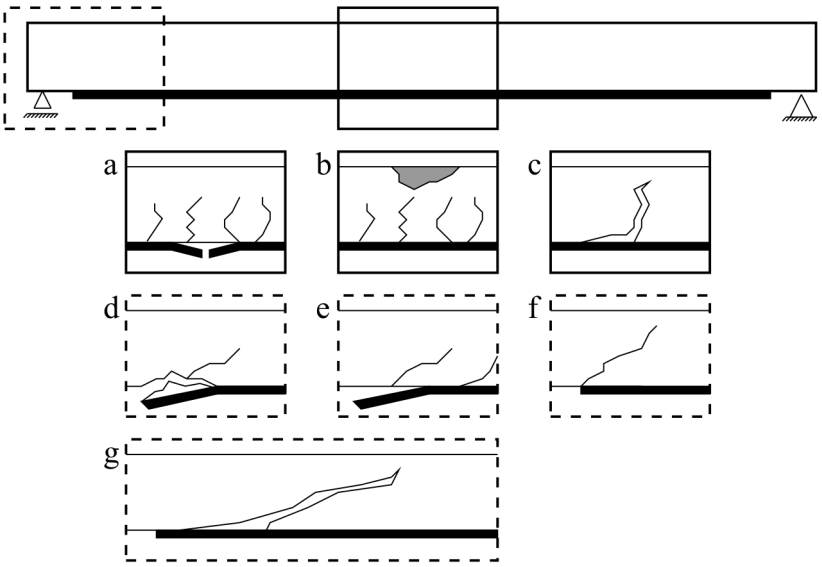

Figure 3.7: Failure modes of RC beams strengthened with FRP: (a) tensile failure of FRP, (b) concrete crushing, (c) intermediate crack induced interfacial debonding, (d) peel on concrete cover, (e) interfacial debonding, (f) shear failure; and (g) critical diagonal crack (Ceci et al., 2012).

concrete crushing or FRP rupture. The latter modes are typically brittle.

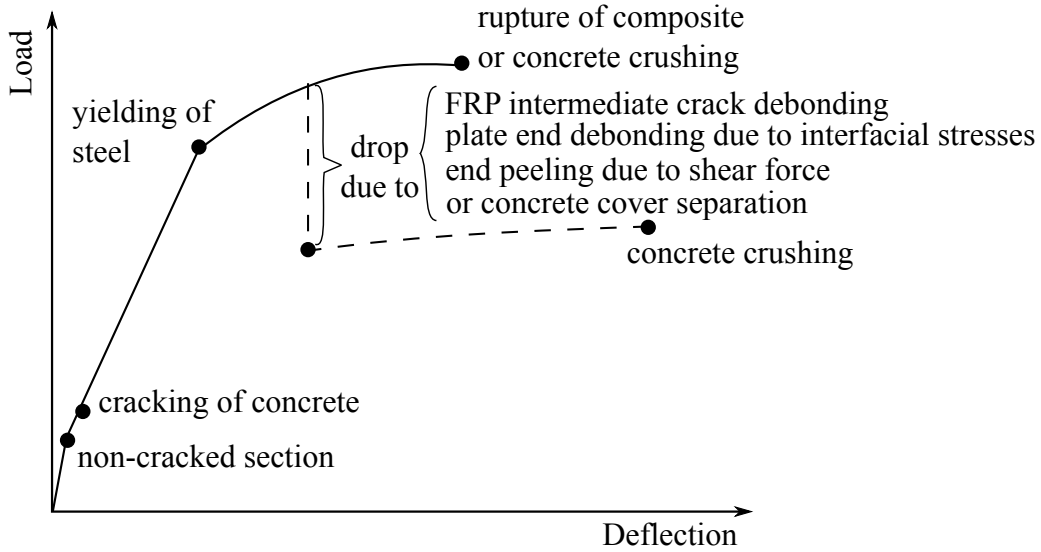

Figure 3.8: Typical load-deflection curve for RC beams strengthened with FRP (Ali, 2012; Balaguru et al., 2008).

Figure 3.9 presents the qualitative behaviour for different reinforcement ratios of FRP strengthened beams. Increasing the amount of FRP gradually increases the

ultimate and cracking loads, and the stiffness, whereas the ductility progressively decreases. Thus, both Young's modulus and ultimate strength of FRP are fundamental properties. There are several experimental studies available in literature, e.g., Quantrill and Hollaway (1998), Triantafillou et al. (1992), Ashour et al. (2004), Ritchie et al. (1991) or Spadea et al. (1998) focusing the use of FRP in RC beams as a strengthening material. Furthermore, these studies highlight the importance of Young's modulus, when failure occurs by debonding of FRP, and of ultimate strength, when failure occurs by rupture of composite. According to ACI 440 (2008), FRP laminates can increase the resistance of the non-strengthened member and decrease the ductility.

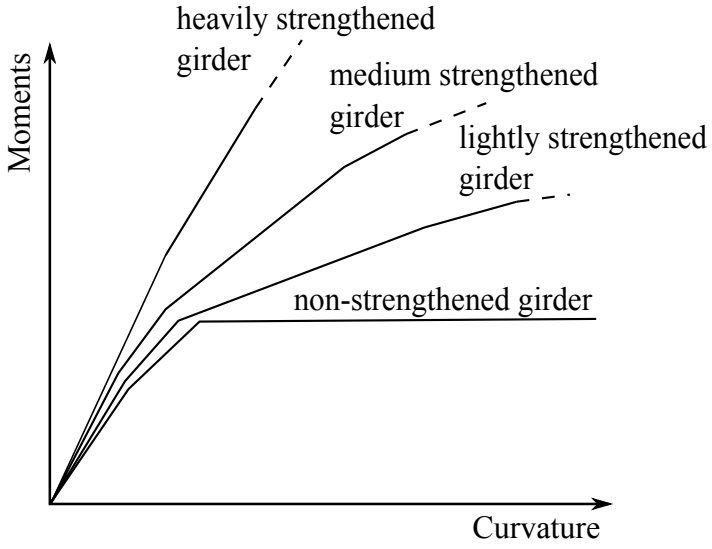

Figure 3.9: Moment vs. curvature of non-strengthened and FRP strengthened beams (adapted from Kelley et al. (2000)).

3.4 Statistical analysis of CFRP properties

Several works aiming at defining statistical models for mechanical properties of FRP are available in literature. Atadero (2006) performed a statistical analysis on field-manufactured wet lay-up carbon and glass epoxy composites from panels constructed during rehabilitation projects or specimens especially manufactured in the laboratory. Six sets, composed by one, three or four subsets resulting in 903 samples, were considered to assess the tensile strength, the Young's modulus and

the laminate thickness. The need to divide the samples in smaller subsets due to different properties and manufacturing processes lead to a significant reduction in the sample size for statistical analysis, resulting in samples of 20 specimens (see Table 3.4). Normal, log-normal, Weibull and Gamma distributions were considered, and the Chi-Squared, the Kolmogorov-Smirnov and the Anderson-Darling goodness-of-fit tests were used to assess the fitting results. The Weibull distribution was adopted to model tensile strength whereas the log-normal distribution was selected to model both Young's modulus and laminate thickness. Additionally, the coefficient of variation (CoV) varied between 0.09 to 0.28 for tensile strength and Young's modulus.

Table 3.4: Summary of the tested samples considered by Atadero (2006).

Data Set	Number of samples	Number of layers	Material	Source
A	49	1	carbon epoxy	rehabilitation project A
	50	2		
	20	3		
B	29	1	carbon epoxy	laboratory
	29	2		
	29	3		
	29	4		
C	177	1	carbon epoxy	rehabilitation project B
D	260	2	carbon epoxy	rehabilitation project C
E	27	1	carbon epoxy	laboratory
	28	2		
	29	3		
	27	4		
F	30	1	glass epoxy	laboratory
	30	2		
	30	3		
	30	4		

Zureick et al. (2006) performed another study over 600 samples of pultruded composite materials of E-glass fibres with polyester or vinylester matrices. The specimens

had to be divided in subsets due to different properties, each one containing no more than 30 samples. The study focused on the longitudinal tensile and compressive strengths, the longitudinal tensile and compressive modulus, the shear strength and modulus. Normal, log-normal and Weibull distributions were considered and the Anderson-Darling goodness-of-fit test was used. The Weibull distribution was proposed to model the strength and stiffness properties. Results presented CoV ranging from 0.04 to 0.132 for tensile strength and modulus. These were lower values than the ones previously shown for field-manufactured wet lay-up samples.

The major drawback of the existing studies is the small sets of samples which cannot accurately characterise the tails of the probabilistic distributions. Furthermore, such reduced number of samples also creates difficulties in the clear choice of the best probability distribution and may result in probabilities of failure varying several orders of magnitude (Ellingwood, 2001). At present, the statistical information concerning this material is still very restricted, which can be seen as a limitation towards the development of more accurate probabilistic models.

The statistical analysis performed over CFRP laminates are described in the following.

3.4.1 Experimental tests

The data used herein was obtained from a large set of tension tests performed as a part of the quality assurance process at S&P - Clever Reinforcement Ibérica, between 2008 and 2012. All samples were produced in the same factory – see Figure 3.10 – and under the same conditions.

The tensile tests were carried out according to ISO 527-5:2009 (2009) standard on a Zwick Z100 universal testing machine, as shown in Figure 3.11 (a). The experimental test set-up is illustrated in Figure 3.11 (b), where the different parts of the specimen are identified. A pre-load of 100 N was applied and specimens were loaded until failure, as shown in Figure 3.12, at a constant displacement rate of 2 mm/min. The applied loading and CFRP strain were directly measured using a load cell and a clip gauge, respectively. A careful selection of data was performed to exclude invalid

Figure 3.10: Factory overview (photography courtesy of S&P - Clever Reinforcement Ibérica).

results arising from the: i) tab region failure, ii) broken fibres in contact with the clip gauge, iii) slippage of specimens from the jaws; and iv) failure of specimens at, or close to, the jaws.

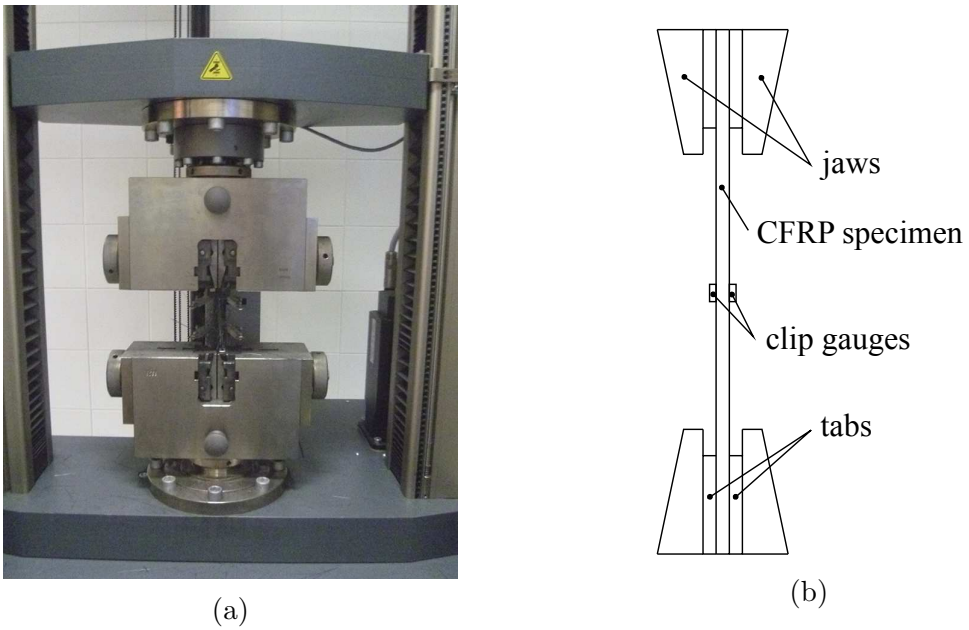

(a) (b)

Figure 3.11: Experimental test set-up: (a) overview (photography courtesy of S&P - Clever Reinforcement Ibérica); and (b) scheme from central area.

A representation of a typical stress-strain diagram of the CFRP is shown in Fig-

(a) (b)

Figure 3.12: Experimental test at failure: (a) overview; and (b) specimen detail (photographs courtesy of S&P - Clever Reinforcement Ibérica).

ure 3.13, where linear elastic behaviour can be observed up to failure. A large batch of tension tests were performed on 1368 laminates of CFRP of various cross-sectional areas (60-168 mm^2) over a period of 4 years. All analysed specimens are pre-cured laminates of carbon fibres embedded in vinylester matrices, the most commonly used set-up for strengthening concrete beams and slabs.

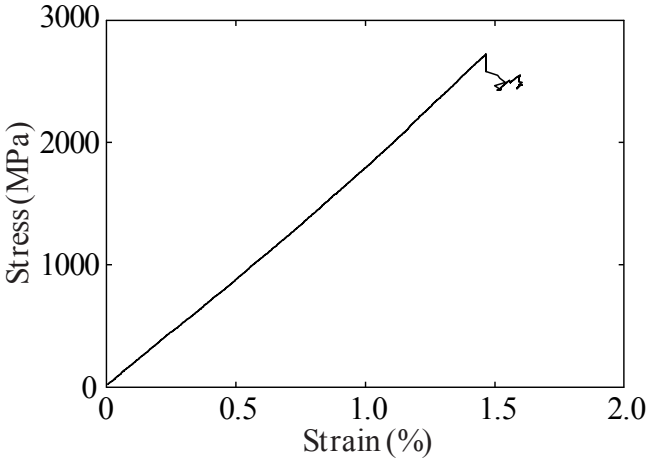

Figure 3.13: Example of stress-strain diagram of tensile tests.

3.4.2 Statistical study

Three statistical distributions were considered to model the CFRP properties: i) normal, ii) log-normal; and iii) Weibull, which are typically appropriate for modelling material properties in several engineering fields. The normal and the log-normal distributions are very easy to use and apply, whereas the Weibull distribution is often found suitable to model brittle materials (such as composites) that usually require extra care for the sample lowest tail (Handbook-MIL 17, 2002). The normal distribution has the advantage of its simplicity and symmetry. The corresponding PDF and CDF are presented in Equations (3.1) and (3.2), where μ is the mean and σ is the standard deviation.

$$\begin{aligned} f(x|\mu,\sigma) &= \tfrac{1}{\sigma\sqrt{2\pi}} e^{-\frac{1}{2}\left(\frac{x-\mu}{\sigma}\right)^2} \\ \sigma > 0; -\infty < x, \mu < +\infty \end{aligned} \tag{3.1}$$

$$F(x|\mu,\sigma) = \frac{1}{\sqrt{2\pi}} \int_{-\infty}^{x} e^{-\frac{1}{2}\left(\frac{t-\mu}{\sigma}\right)^2} dt \tag{3.2}$$

The log-normal distribution is closely related with the normal distribution; a variable is log-normal if its natural logarithm is normally distributed. Equations (3.3) and (3.4) are, respectively, the PDF and the CDF of this distribution, where μ and σ are the mean and standard deviation of the associated normal distribution.

$$\begin{aligned} f(x|\mu,\sigma) &= \tfrac{1}{x\sigma\sqrt{2\pi}} e^{-\frac{1}{2}\left(\frac{\ln(x)-\mu}{\sigma}\right)^2} \\ x > 0; \sigma > 0; -\infty < \mu < +\infty \end{aligned} \tag{3.3}$$

$$F(x|\mu,\sigma) = \frac{1}{\sigma\sqrt{2\pi}} \int_{0}^{x} \frac{1}{t} e^{-\frac{1}{2}\left(\frac{\ln(t)-\mu}{\sigma}\right)^2} dt \tag{3.4}$$

The Weibull distribution is commonly used for modelling properties of composites (Handbook-MIL 17, 2002). The Weibull distribution adopted herein was based solely on two-parameters, since existing studies showed that the statistical characterisation of the FRP does not improve with three-parameters (Alqam et al., 2002). The corresponding PDF and CDF are presented in Equations (3.5) and (3.6), where α

is the shape parameter and β is the scale parameter.

$$\begin{gathered} f(x|\alpha,\beta) = \frac{\alpha}{\beta^{\alpha}} x^{\alpha-1} e^{-\left(\frac{x}{\beta}\right)^{\alpha}} \\ \alpha,\beta \geq 0; 0 \leq x < \infty \end{gathered} \tag{3.5}$$

$$F(x|\alpha,\beta) = 1 - e^{-\left(\frac{x}{\beta}\right)^{\alpha}} \tag{3.6}$$

3.4.2.1 Statistical analysis

The statistical analysis was performed having into special consideration the lower tail of the distributions, which are paramount for structural reliability analysis. The analyses were first performed by considering the whole sample (see Figure 3.14 (a)) and the empirical PDF and CDF were plotted with the fitted distributions for each property. Then, the best fit distributions for the lower tails were found following the censored Maximum Likelihood Estimation (MLE) (Lindley, 1965). This method allows to estimate parameters θ of a statistical distribution for a sample, considering the following:

$$L(\theta|\hat{x}_1, \hat{x}_2, \ldots, \hat{x}_n) = \prod_{i=1}^{n} f_X(\hat{x}_i|\theta) \tag{3.7}$$

in which $L(.)$ is the likelihood that the parameters $\theta = \theta_1, \theta_2, \ldots, \theta_n$ properly describe a sample $\hat{x} = \hat{x}_1, \hat{x}_2, \ldots, \hat{x}_n$ and f_X is the joint PDF of a sample. The maximum likelihood estimators are computed from the set of parameters that maximise the likelihood function, considering all possible cases of θ.

In this thesis, the likelihood method used in Faber et al. (2004) was adopted to perform a better approximation for the lower tail. This technique uses explicitly the values of the lower tail that are smaller than a predefined bound, x_G, as illustrated in Figure 3.14 (b), whereas the remaining values are used implicitly. The censored MLE was defined having into account the following contributions:

$$L = L1 \times L2 \tag{3.8}$$

with

$$L1 = \prod_{i=1}^{j} f(x_i|\theta) \tag{3.9}$$

$$L2 = P(X \geq x_G|\theta)^{n-j} \tag{3.10}$$

$$P(X \geq x_G|\theta) = 1 - F(x_G|\theta) \tag{3.11}$$

where $L1$ is the likelihood associated with the j observations of values equal or lower than the bound value x_G, $L2$ is the likelihood associated with the observations of higher values than the bound value x_G, $F(x_G|\theta)$ is the CDF of x_G given the PDF θ, n is the total number of observations and $n - j$ is the total number of observations exceeding the bound value x_G. The best fit can be computed iteratively through the optimisation problem by maximising L.

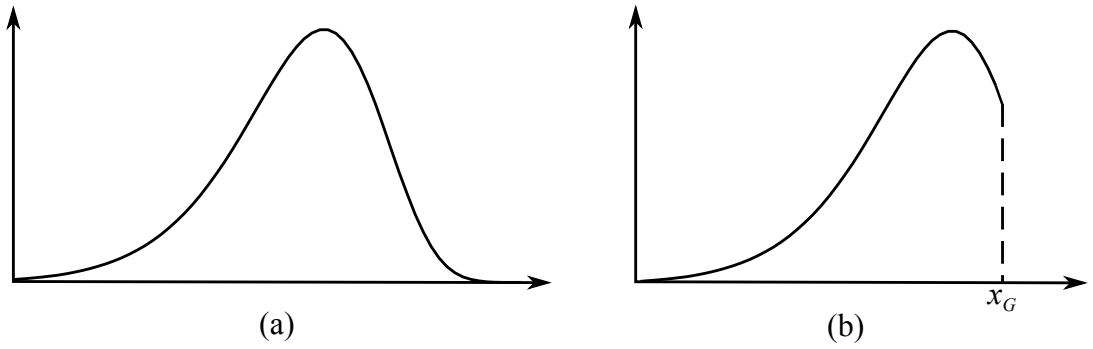

Figure 3.14: Distributions: (a) completed; and (b) right censored.

For each property, the distributions families were adjusted for the entire sample and the: 20^{th}, 25^{th}, 30^{th}, 35^{th} and 40^{th} lower percentiles. In this regard, it is important to highlight that the 20^{th} percentile is considered to be a reasonable choice for the lowest limit in reliability studies since it includes the region of interest without decreasing the sample size to statistically meaningless values.

3.4.2.2 Goodness-of-fit test

The goodness-of-fit test is a method to indicate if a hypothesised distribution is a good fit. This test can be formulated through two statements:

- H_0 (null hypothesis): when the data follows the distribution;
- H_1 (alternative hypothesis): when the data does not follow the distribution.

Several goodness-of-fit tests are used in various branches of engineering, such as the Kolmogorov-Smirnov, the Anderson-Darling or the Pearson's chi-squared. In this thesis, the Anderson-Darling test was used to evaluate the quality of the fit distributions, because it provides more importance to tail regions. Therefore, H_0 was not rejected if the statistic value (A^2) was lower than the critical value (CV). According to Stephens and D'Agostino (1986), the statistic values for the entire range and the right-censored samples could be respectively obtained according to:

$$A^2 = -\frac{1}{n}\sum_{i=1}^{n}(2i-1)\left[\ln Z_{(i)} + \ln(1 - Z_{(n+1-i)})\right] - n \tag{3.12}$$

$$\begin{aligned} A^2_{r,n} = -\frac{1}{n}\sum_{i=1}^{r}(2i-1)[\ln Z_{(i)} - \ln\{1 - Z_{(i)}\}] - 2\sum_{i=1}^{r}\ln\{1 - Z_{(i)}\} \\ -\frac{1}{n}[(r-n)^2\ln\{1 - Z_{(r)}\} - r^2\ln Z_{(r)} + n^2 Z_{(r)}] \end{aligned} \tag{3.13}$$

where r are the uncensored observations, n is the total number of observations and Z denotes the CDF of the probability distribution.

Table 3.5: Critical values (Stephens and D'Agostino, 1986).

Percentile	20^{th}	25^{th}	30^{th}	35^{th}	40^{th}	100^{th}
CV	0.436	0.545	0.651	0.756	0.857	1.933

The critical values for different percentiles are presented in Table 3.5. In order to minimise Type I errors that could occur when H_0 was wrongly rejected; or Type II errors, in which H_0 was wrongly accepted, the significance level, α, was set at 10%.

3.4.2.3 Characteristic values

The FRP design guidelines have a general approach to determine design values for composite properties. Usually, the variability of Young's modulus is neglected, and the nominal value is taken equal to the mean value, whereas the tensile strength and ultimate strain are defined as a specific characteristic value.

The CEB/FIB (2001), the CNR (2013) or the CSA (2006) define the characteristic values to correspond to the 5^{th} percentile of the tests results, whereas other codes – such as the ACI 440 (2008) or the TR-55 (2000) – propose other tiers (see Section 5.2). In this thesis, the characteristic value was considered as the one that corresponds to the 5^{th} percentile, in accordance to the CEN (2002a) philosophy.

3.4.2.4 Results

Young's modulus

The Young's modulus is one of the most significant material property to the structural safety of CFRP for retrofitting existing concrete structures, particularly in situations where failure is expected to occur with tensile stresses at FRP significantly below its strength. This typically occurs when debonding of FRP are dominant failure mechanisms (CEB/FIB, 2001).

The results obtained for the Young's modulus are illustrated in Figure 3.15. As it can be seen in Figure 3.15 (a), when the distributions are fitted to the entire sample, significant differences exist in the range of the lower values. Concerning that these are critical for safety assessment, clear improvements are obtained when applying the censored data approach, as shown in Figure 3.15 (b). Furthermore, it is also possible to verify that the normal and log-normal distributions provide similar results, whereas the Weibull distribution shows the closest fit to the data.

The Q-Q plots are a valuable tool to visualise the quality of fit. In Figure 3.16, the adjustments for the entire data (see Figure 3.16 (a)) and the lower tail (see Figure 3.16 (b)) of the normal distribution are shown. These strengthen the earlier observation that results are better for the range of the lower values when censored

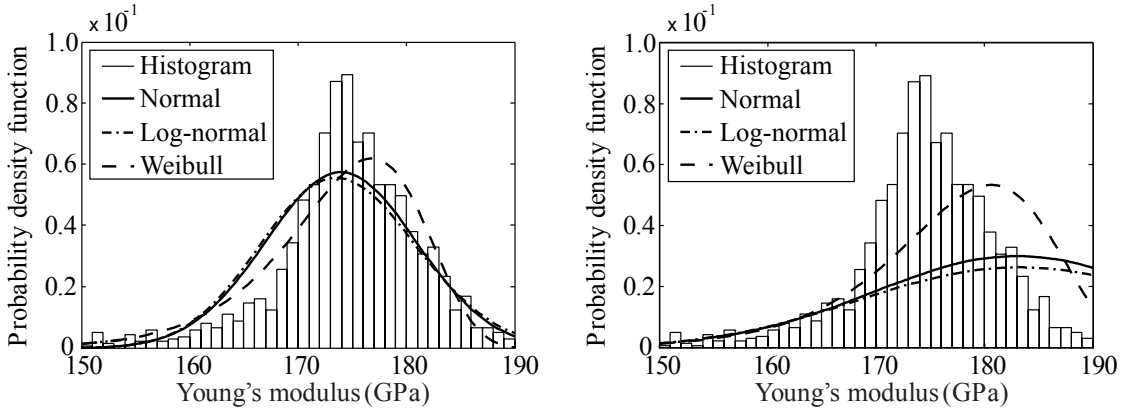

Figure 3.15: PDF for the Young's modulus of: (a) entire data fit; and (b) lower tail fit (20^{th}).

data is considered. Equivalent results are shown in Figures 3.17 and 3.18 for the log-normal and Weibull distributions respectively. The normal and log-normal distributions produce identical results, whereas the Weibull distribution is the one that shows the highest closeness to the data when adjusted to the entire sample (see Figure 3.18 (a)). Moreover, when adjusted to the lowest sample, it also presents the smallest discrepancy between data and distribution (see Figure 3.18 (b)).

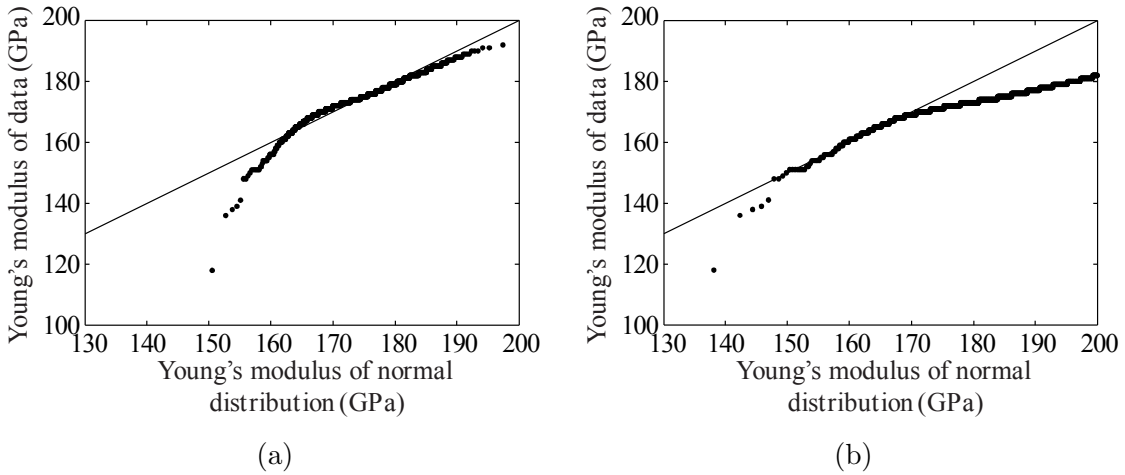

Figure 3.16: Q-Q plot of the Young's modulus considering the normal distribution adjusted to: (a) entire data; and (b) lower tail (20^{th}).

The statistic values for the Anderson-Darling goodness-of-fit tests are presented in Table 3.6. The shaded cells refer to the tests where the distributions are not re-

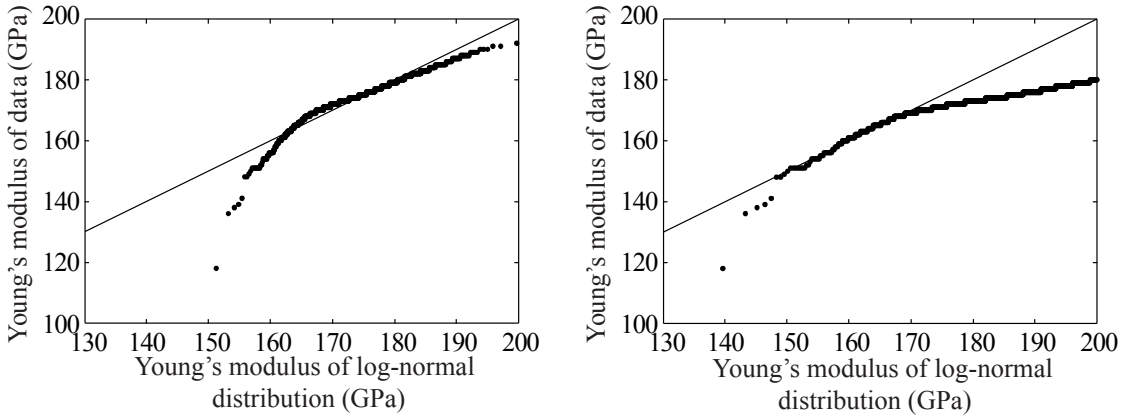

Figure 3.17: Q-Q plot of the Young's modulus considering the log-normal distribution adjusted to: (a) entire data; and (b) lower tail (20^{th}).

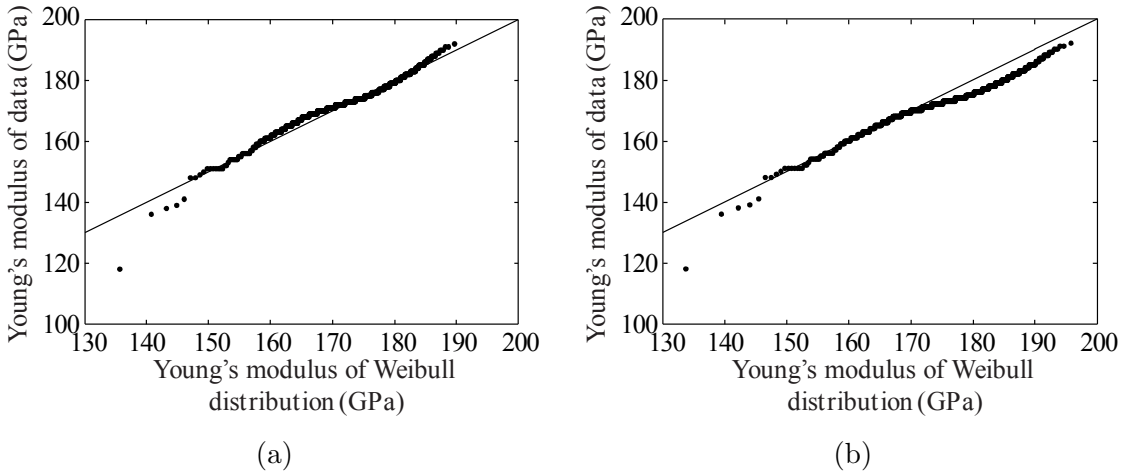

Figure 3.18: Q-Q plot of the Young's modulus considering the Weibull distribution adjusted to: (a) entire data; and (b) lower tail (20^{th}).

jected. The results show that the only distribution where the null hypothesis is not rejected for the highest percentile (25^{th}) is the Weibull. Additionally, this distribution also presents the lowest statistic value, meaning that the average squared distance between the data and the fitted distribution is the smallest.

Based on these results, the Weibull distribution is proposed to model the Young's modulus with the following parameters:

$$E_f \sim \mathrm{W}(\alpha, \beta); \quad \alpha = 26.2 \text{ GPa}; \quad \beta = 180.9 \text{ GPa} \tag{3.14}$$

Table 3.6: Statistical values for the Young's modulus.

Percentil	Normal	Log-normal	Weibull
20	0.279	0.373	0.123
25	0.598	0.696	0.427
30	1.587	1.697	1.327
35	1.587	1.697	1.327
40	4.226	4.351	3.767
100	18.236	23.568	13.678

The Young's modulus corresponding to the 5^{th} percentile of the proposed distribution is 161.5 GPa. The latter value is similar to the 5^{th} percentile of the data (162 GPa). Moreover, results show that the obtained CoV (V=0.04) is very low when compared with the previous results from Atadero (2006) and Zureick et al. (2006).

The adopted distribution is in agreement with the proposal from Zureick et al. (2006). The log-normal distribution was recommended by Atadero (2006), although focusing on the entire data fit procedure.

Ultimate strain

The ultimate strain is an important parameter for structural safety, since the material typically exhibits elastic behaviour until failure. As in the previous case the PDF of this property, illustrated in Figure 3.19, shows that the selected distributions adjusted to the entire sample fit well the data (see Figure 3.19 (a)). Furthermore, normal and log-normal distributions present similar results whereas the Weibull presents the worst adjustment to the lower tail. Thus, a fit to the lowest part of the data was considered (see Figure 3.19 (b)). Here, it is possible to see that all distributions provide good fits to the lower range, whereas the Weibull is the one that presents the best fit to all entire range.

The Q-Q plots computed for this property, are presented in Figures 3.20, 3.21 and 3.22, for the normal, log-normal and Weibull distributions respectively. For the entire sample adjustment (see Figures 3.20 (a), 3.21 (a) and 3.22 (a)) it is possible to confirm that the lowest values are not well represented. A better representation is achieved by the consideration of the adjustment to the lower tail. However, for the

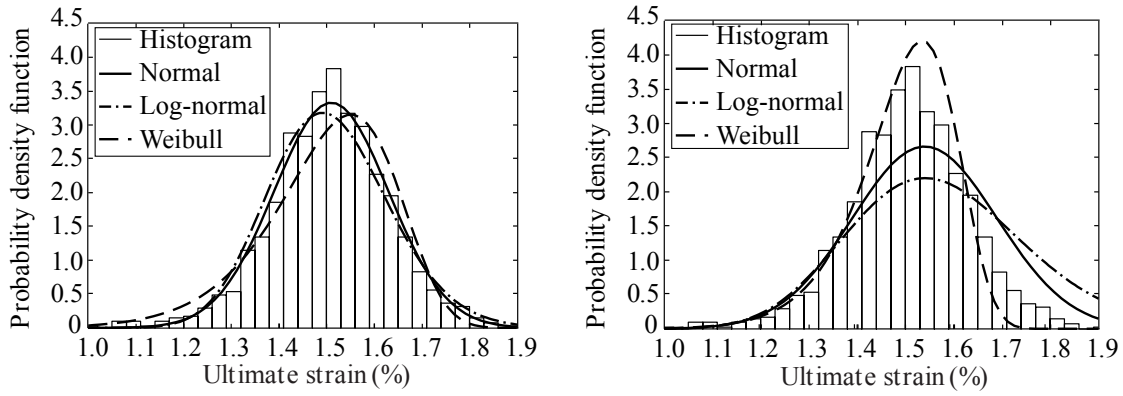

Figure 3.19: PDF for the ultimate strain of: (a) entire data fit; and (b) lower tail fit (20^{th}).

normal and log-normal distributions (see Figures 3.20 (b) and 3.21 (b)) the adjustment is not significantly improved in this area, whereas for the Weibull distribution the same adjustment is greatly improved (see Figure 3.22 (b)). Furthermore, the Weibull distribution presents a better fit for the remaining data.

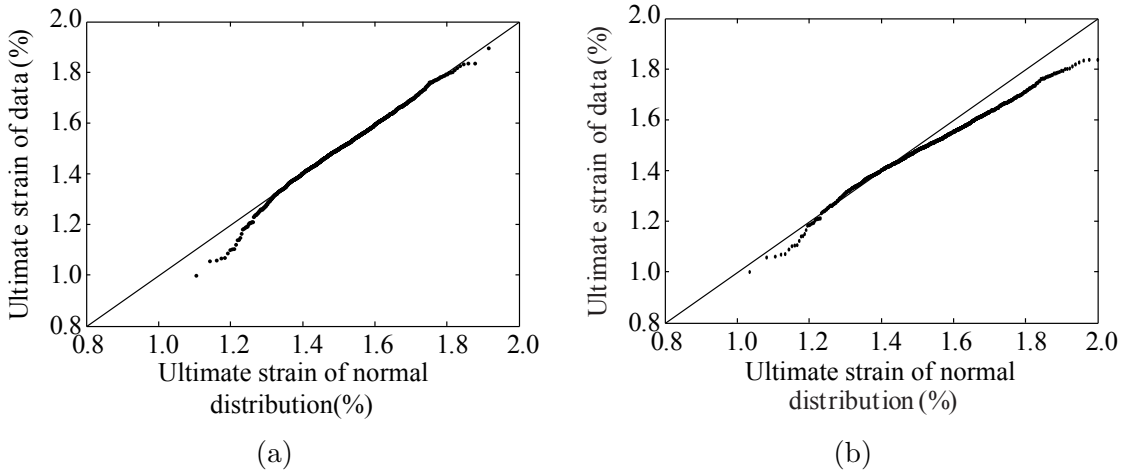

Figure 3.20: Q-Q plot of the ultimate strain considering the normal distribution adjusted to: (a) entire data; and (b) lower tail (20^{th}).

The Anderson-Darling goodness-of-fit tests results are presented in Table 3.7. The Weibull is the only distribution not rejected for the highest percentile (40^{th}), whereas the null hypothesis is rejected for all the distributions adjusted to the entire sample.

Based on the results, the Weibull distribution is proposed to model the ultimate

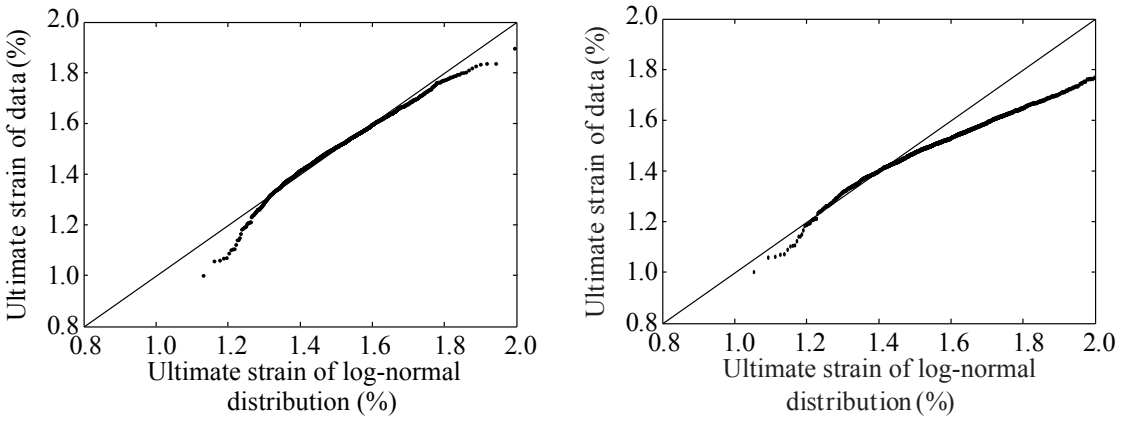

(a) (b)

Figure 3.21: Q-Q plot of the ultimate strain considering the log-normal distribution adjusted to: (a) entire data; and (b) lower tail (20^{th}).

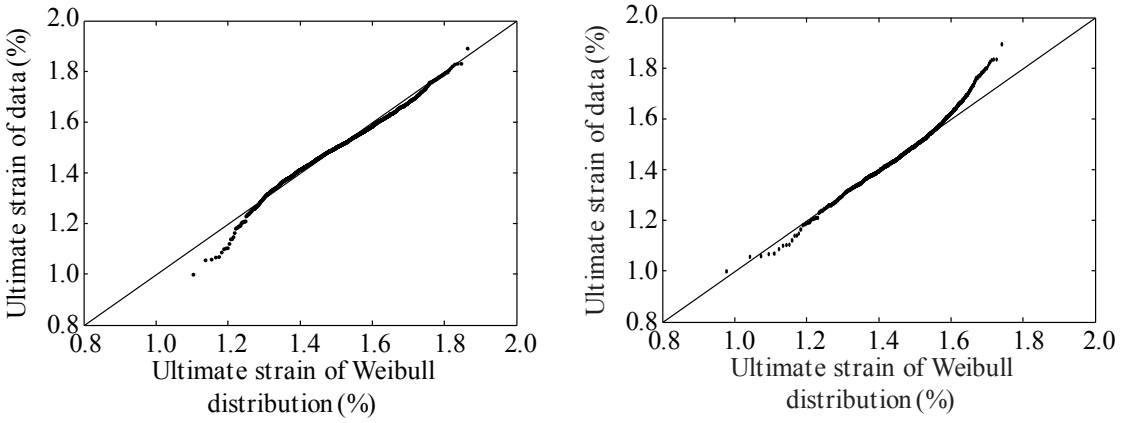

(a) (b)

Figure 3.22: Q-Q plot of the ultimate strain considering the Weibull distribution adjusted to: (a) entire data; and (b) lower tail (20^{th}).

strain, which has a CoV of 0.06 and is defined as follows:

$$\varepsilon_{fu} \sim \mathrm{W}(\alpha, \beta); \quad \alpha = 17.1\%; \quad \beta = 1.5\% \tag{3.15}$$

Tensile strength

The tensile strength can be important in situations where failure occurs by the laminate. This can be critical to situations of pre-stressed CFRP laminates, where

Table 3.7: Statistical values for the ultimate strain.

Percentile	Normal	Log-normal	Weibull
20^{th}	0.206	0.351	0.050
25^{th}	0.237	0.393	0.057
30^{th}	0.433	0.656	0.101
35^{th}	0.771	1.148	0.126
40^{th}	1.371	2.056	0.136
100^{th}	2.5453	5.485	8.9873

the pre-stress often represents a high percentage of the tensile strength (Quantrill and Hollaway, 1998; Triantafillou et al., 1992).

Preliminary results of the distributions adjusted to the entire sample (see Figure 3.23) showed that all selected distributions are unable to provide a good fit to the lower tail range. Figure 3.23 (b) shows the improvement that can be obtained when following the procedure based on fitting the CDF to the lower tail. In both cases, the Weibull distribution has a better approximation to the data than the remaining distributions.

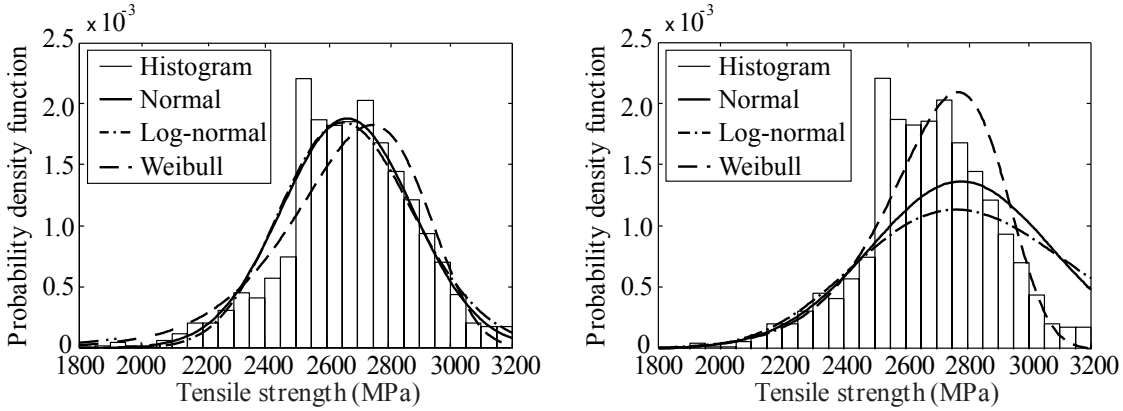

Figure 3.23: PDF for the tensile strength of: (a) entire data fit; and (b) lower tail fit (20^{th}).

The Q-Q plots of normal and log-normal distributions are similar, as shown in Figures 3.24 and 3.25. As expected, it is possible to see in both cases that the adjustment for the entire sample is not suitable for the lower tail region (see Fig-

ures 3.24 (a) and 3.25 (a)). The Weibull distribution, illustrated in Figure 3.26, presents an improvement of the lower tail fit when the adjustment to this region is considered. Furthermore, the remaining data shows a better adjustment when the Weibull distribution is used.

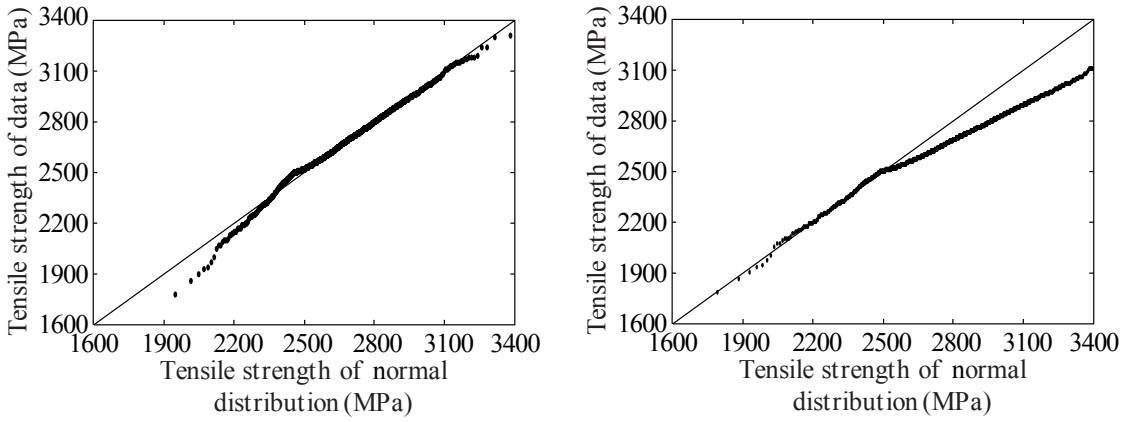

Figure 3.24: Q-Q plot of the tensile strength considering the normal distribution adjusted to: (a) entire data; and (b) lower tail (20^{th}).

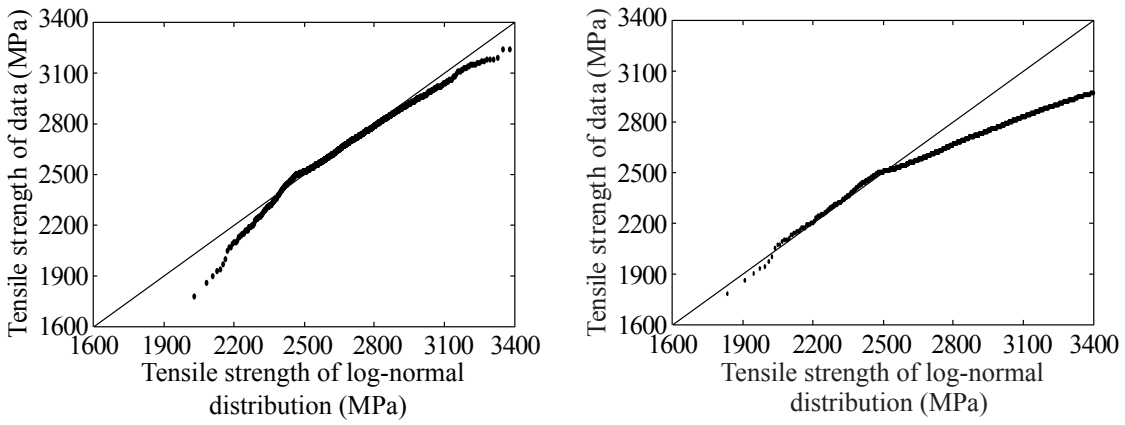

Figure 3.25: Q-Q plot of the tensile strength considering the log-normal distribution adjusted to: (a) entire data; and (b) lower tail (20^{th}).

The performed goodness-of-fit tests considered the statistical values computed in Table 3.8. The results show that none of the distributions are rejected for the 20^{th} and 25^{th} percentiles. Therefore, and since the Weibull distribution is the one that visually presents better results than the others, it is also the distribution proposed

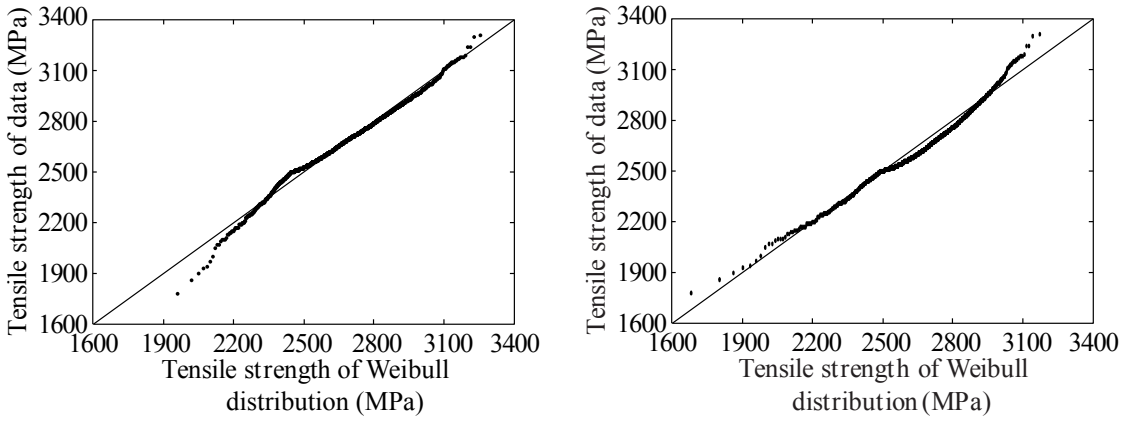

Figure 3.26: Q-Q plot of the tensile strength considering the Weibull distribution adjusted to: (a) entire data; and (b) lower tail (20^{th}).

for the tensile strength with the following parameters:

$$f_f \sim \text{ W}(\alpha, \beta); \quad \alpha = 15.9 \text{ MPa}; \quad \beta = 2777.0 \text{ MPa} \tag{3.16}$$

Table 3.8: Statistical values for the tensile strength.

Percentile	Normal	Log-normal	Weibull
20^{th}	0.050	0.068	0.064
25^{th}	0.342	0.366	0.333
30^{th}	0.894	0.941	0.817
35^{th}	2.518	2.658	2.154
40^{th}	4.160	4.429	3.404
100^{th}	5.453	5.485	9.897

The 5^{th} characteristic value for the proposed distribution is 2304.2 MPa, which is 0.3% higher than the sample value (2299.0 MPa). The CoV is also very small (V=0.08) when compared with the pultruded composite materials presented in Atadero (2006) and Zureick et al. (2006).

The selected distribution is in agreement with the proposals from Atadero (2006) and Zureick et al. (2006) to model tensile strength for the entire sample.

3.4.3 Correlation study

The correlation between the different properties was carried out to identify the dependency between the different variables. Herein, linear regression analyses were performed between the: i) tensile strength and ultimate strain, ii) tensile strength and Young's modulus, iii) Young's modulus and ultimate strain; and iv) all variables considering a three-dimensional linear regression. All results are presented herein.

Tensile strength vs. ultimate strain

Firstly, a linear regression analysis was performed between tensile strength and ultimate strain without constraints. Results show high correlation between these two properties ($r^2 = 0.75$) as illustrated in Figure 3.27 (a). Additionally, the residual standard deviation, which indicates the uncertainty in the proposed model, is 0.062%. Thus, the probabilistic model presented in the following equation can be used to describe the correlation between these properties:

$$\varepsilon_{fu} = 0.17 + 0.0005014 f_f + 0.0618 Z(\%) \tag{3.17}$$

where f_f is in MPa and $Z \sim N(0, 1)$.

Based on the results above, a second correlation analysis was performed constraining the linear regression to the origin. The results are very similar, as shown in Figure 3.27 (b). The latter model presents a residual standard deviation of 0.063% and is defined by the following equation:

$$\varepsilon_{fu} = 0.0005646 f_f + 0.0633 Z(\%) \tag{3.18}$$

where f_f is in MPa and $Z \sim N(0, 1)$.

Since the results between both analyses are very similar and the latter model is simpler, it can be employed whenever these two properties are used simultaneously.

Tensile strength vs. Young's modulus

The correlation between tensile strength and Young's modulus ($r^2 = 0.0095$) is quite

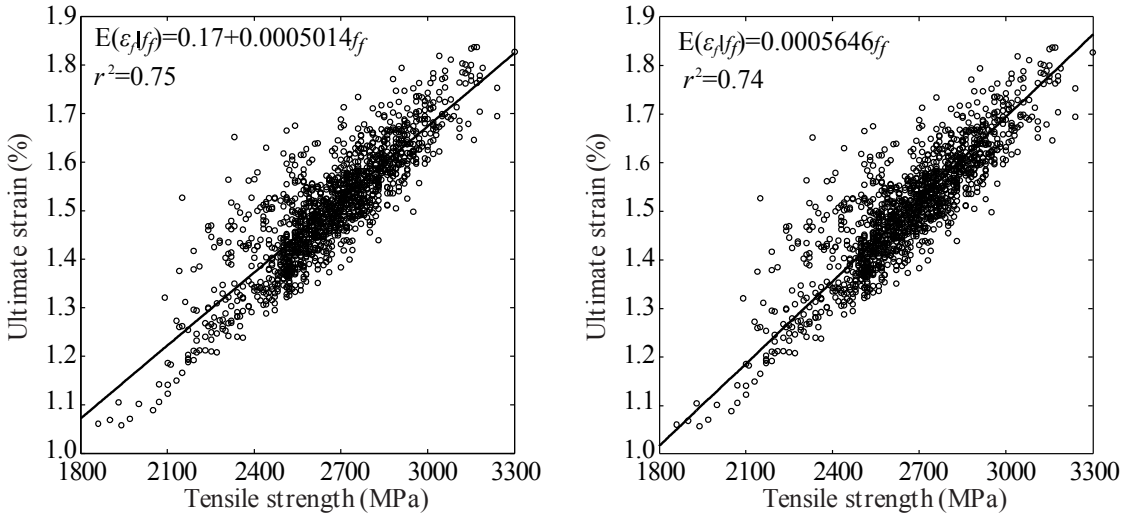

(a) (b)

Figure 3.27: Scatter diagram of tensile strength vs. ultimate strain (f_f, ε_f): (a) regression without constrains; and (b) regression across the origin.

small, showing that these properties can be considered independent, as illustrated in Figure 3.28 (a).

Young's modulus vs. ultimate strain

The last two-dimensional correlation analysis was performed between the Young's modulus and ultimate strain, as shown in Figure 3.28 (b). The low correlation ($r^2 = 0.061$), shows that these two properties can also be considered independent.

Three-dimensional correlation

The three-dimensional analysis performed between all variables is presented in Figure 3.29, where is possible to observe that these three properties are highly correlated, having a $r^2 = 0.8576$. Hence, the correlation between these properties can be described according to the following equation:

$$\varepsilon_f = 1.148 - 0.005915E_f + 0.0005202f_f \tag{3.19}$$

where E_f is in GPa and f_f is in MPa.

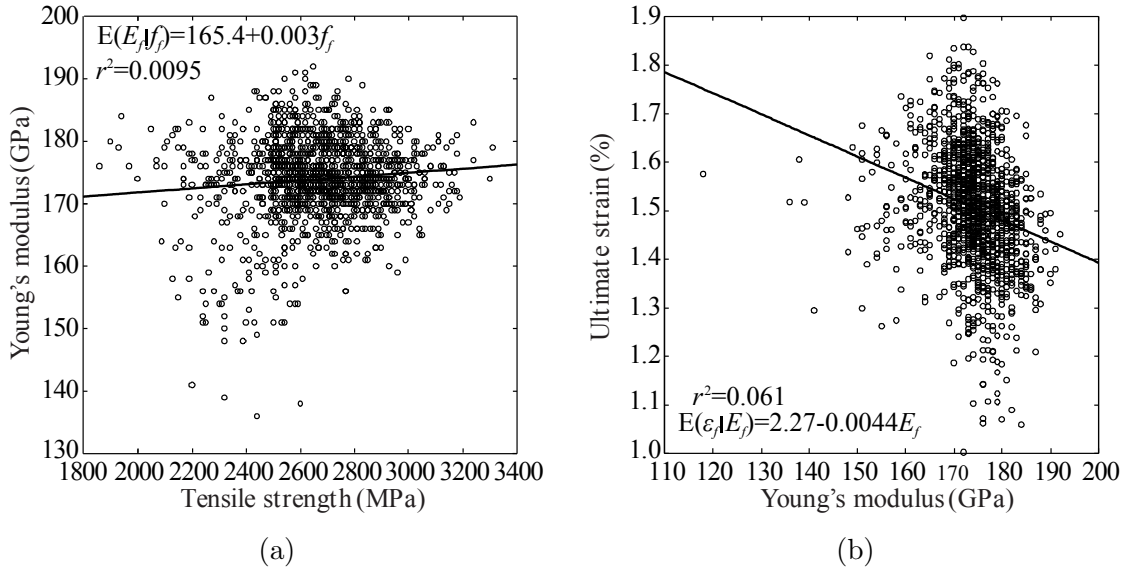

Figure 3.28: Scatter diagram of: (a) tensile strength vs. Young's modulus (f_f, E_f); and (b) Young's modulus vs. ultimate strain (E_f, ε_f).

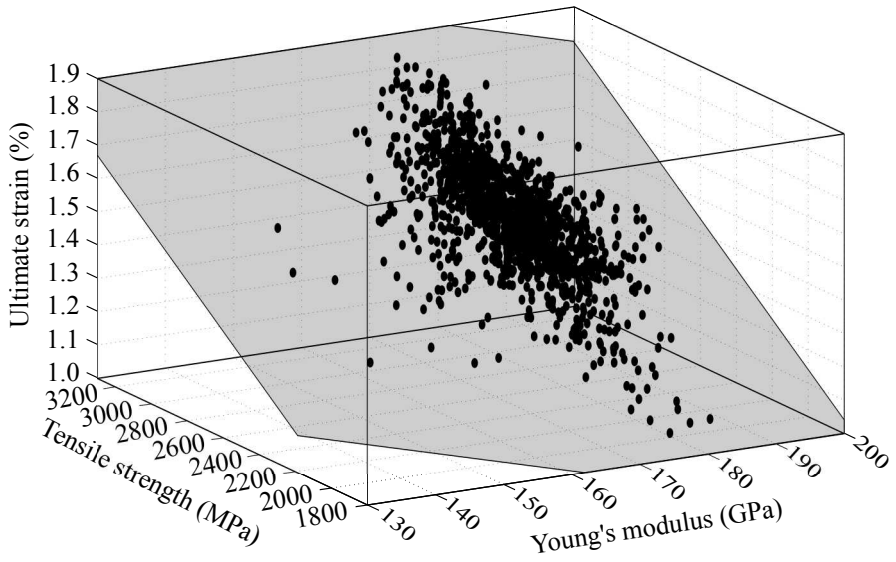

Figure 3.29: Three-dimensional scatter diagram of Young's modulus vs. ultimate strain vs. tensile strength $(E_f, \varepsilon_f, f_f)$.

3.5 Conclusions

In this chapter, statistical models for mechanical properties of CFRP were developed. The probabilistic analysis was based on experimental tests performed over 4 years

for control of S&P Clever Reinforcement Ibérica.

The statistical analysis was made having into account the lower tails. For this reason, besides complete distributions, right censored distributions were additionally considered. The MLE used for timber properties was successfully employed in FRP (Faber et al., 2004). Moreover, the Anderson-Darling goodness-of-fit test was used since it gives more importance to tails. Results show that the Weibull distribution can be adopted to model the Young's modulus, the tensile strength and the ultimate strain of CFRP. A low variability in the materials properties is observed; it is also important to highlight that the lowest CoV was measured in the Young's modulus, which is one of the most important properties for the CFRP. Furthermore, the 5^{th} percentile values of the Young's modulus obtained from experimental data and proposed distribution are similar.

The Weibull distributions proposed herein are consistent with the results proposed by Zureick et al. (2006) and Atadero (2006). For instance, Zureick et al. (2006) proposed the Weibull distribution to model Young's modulus and tensile strength, whereas Atadero (2006) proposed the log-normal distribution for Young's modulus and the Weibull for tensile strength. Although, it is important to highlight that both of these studies were based on small size samples and were performed considering the whole sample.

The correlation analysis show that tensile strength and ultimate strain are strongly correlated, whereas tensile strength and Young's modulus, and Young's modulus and ultimate strain are nearly independent variables.

The presented results do not cover all aspects of uncertainties of CFRP mechanical properties. For instance, uncertainties resulted from different manufacturers or environmental conditions may be interesting to consider. Besides, different fibres or application processes that may lead to change in FRP properties are also important to have into account.

Chapter 4

Numerical and analytical models

4.1 Introduction

As presented in the previous chapter, statistical studies concerning FRP are important to establish a new framework to evaluate the reliability of FRP strengthened RC structures. Reliability analysis can be supported by advanced numerical models capable of simulating the 'real' non-linear structural behaviour to a certain extent. Among several aspects, such as construction sequence, non-linear material behaviour, concrete cracking or FRP-concrete interface, the detailed numerical modelling of these structural elements is a highly complex problem. Furthermore, when a massive number of analyses is needed, as in the case of statistical nature studies, this type of models may fall behind, leaving an open space for analytical models. Nevertheless, the latter models are typically limited for simple structural problems and have underlying assumptions that do not allow tackling complex case scenarios.

In this chapter, the numerical and analytical models used to characterise the structural bending behaviour of PC girders are described. When dealing with FRP strengthened RC elements, the bond between FRP and concrete can be critical. Studies have reported that debond failure occurs frequently and prevents the use of composite in full, leading to sudden mechanisms of failure (Barros et al., 2007; Correia et al., 2015; Fortes et al., 2003; Garden and Hollaway, 1998; Leeming and

Hollaway, 1999; Quantrill and Hollaway, 1998). This makes the FRP-concrete interface to take an important role in the development of both numerical and analytical models.

Several researches have been devoted to predict the behaviour of FRP-concrete interface – e.g., Ali-Ahmad et al. (2006); Chen and Teng (2001); Coronado and Lopez (2010); Lorenzis et al. (2001) – proposing different bond-slip constitutive laws. Additionally, different concrete-FRP bond models have been used in numerical studies with good results. For instance, Coronado and Lopez (2006), Obaidat et al. (2010) and Hu et al. (2004) adopted perfect bond in their study, whereas Wong and Vecchio (2003), Kishi et al. (2005) and Chen et al. (2012) used a linear-elastic law and Wong and Vecchio (2003) a elasto-plastic model. More accurate models were adopted by Niu and Wu (2005) and Aktas and Sumer (2014) using bilinear equations, or by Baky et al. (2007), Lu et al. (2007), Chen et al. (2011) or Zidani et al. (2015) through exponential softening laws.

Besides the modelling of FRP-concrete interface, numerical studies to predict the development of concrete cracks before FRP debond in RC elements have been performed. In FE analysis, concrete cracking is traditionally modelled either by smeared or discrete approaches (Borst et al., 2004). In the former, the deformation due to cracking is treated with a continuum model. As such, the deterioration process is materialised through a constitutive relation, in which case cracks are not numerically solved (Borst et al., 2004). Several studies have used this approach to characterise damage prior to the FRP debonding – see Baky et al. (2007); Chen et al. (2012, 2011); Chen and Pan (2006); Hu et al. (2004); Lu et al. (2007); Rahimi and Hutchinson (2001); Sena-Cruz et al. (2011); Wong and Vecchio (2003); Yang et al. (2009); Zidani et al. (2015). Nevertheless, the fractured behaviour can only be described on average. When failure is caused by localised cracks, the discrete crack approach can provide better results. In this method, cracking is physically modelled by a jump on the displacement (Borst et al., 2004). However, the high number of cracks and the material non-linearity can pose some numerical difficulties that may require the use of specific solution-finding algorithms. Several researchers used this approach to model RC girders strengthened with FRP – e.g., Camata et al. (2007); Kishi et al. (2005); Neto et al. (2009); Niu and Wu (2005); Yang et al. (2003).

Analytical models have been used by designers and researchers to predict the flexural capacity of FRP strengthened concrete beams. The models are based on the equilibrium of stresses and on a linear strain distribution over the beam depth. The debond failure is characterised by a limit strain and the non-linear constitutive behaviour of the material is also considered, usually neglecting the tensile strength of concrete. When a rehabilitation/repair scenario is considered, the existing previously strains at bottom of the beam, are also taken into account. Several researchers have used experimental works to validate analytical models, e.g., Barros et al. (2008); Rezazadeh et al. (2015); Woo et al. (2008); Xue et al. (2010); whereas others have employed analytical models to perform reliability studies, see Atadero and Karbhari (2008); El-Tawil and Okeil (2002); Gomes et al. (2012, 2014a); Pham and Al-Mahaidi (2008); Plevris et al. (1995).

The present chapter refers the main aspects and the underlying choices concerning the adopted models. Numerical and analytical models are described, respectively, in Sections 4.2 and 4.3. Then, the validation of both models is presented in Section 4.4 and the main conclusions are drawn in Section 4.5.

4.2 Discrete crack model

As previously mentioned, smeared and discrete crack models are two different approaches available for simulating concrete fracture. Whereas the first uses continuum models to describe the average fractured behaviour, in the latter approach a discontinuity or crack is introduced as a discrete geometric entity, which is able to simulate material separation. Extensive description concerning the different approaches can be found in the literature, namely on the works from Borst et al. (2004) and Bažant and Oh (1983). In this thesis, a discrete crack model designated by the discrete strong discontinuity approach (DSDA) (Dias-da-Costa et al., 2009) was adopted to model the interaction between concrete cracks and the FRP which may cause it to debond. The DSDA embeds existing discontinuities (or cracks) in regular finite elements and is independent of the selected mesh, which does not have to conform to expected pathways for fracture propagation. In the following sections, the main aspects related with this technique are reviewed.

4.2.1 Governing equations

Governing equations are derived in the scope of strong discontinuities which lead to jumps in the displacement field. The corresponding variational equation for a discontinuity, Γ_d, inside the body Ω is (Dias-da-Costa et al., 2009):

$$-\int_{\Omega\setminus\Gamma_d}(\boldsymbol{\nabla}^{sym}\delta\mathbf{u}):\boldsymbol{\sigma}d\Omega-\int_{\Gamma_d}\delta[\![\mathbf{u}]\!]\cdot\mathbf{t}^{+}d\Gamma+\int_{\Omega\setminus\Gamma_d}\delta\mathbf{u}\cdot\bar{\mathbf{b}}d\Omega+\int_{\Gamma_t}\delta\mathbf{u}\cdot\bar{\mathbf{t}}d\Gamma=0 \quad (4.1)$$

where $\boldsymbol{\sigma}$ is the stress tensor, $[\![\mathbf{u}]\!]$ is the opening of the discontinuity, $\mathbf{t}^{+}$ is the traction at discontinuity, $\mathbf{u}$ is the total displacement, $\bar{\mathbf{b}}$ are the quasi-static forces applied to the body and $\bar{\mathbf{t}}$ are the stresses distributed on the external surface of the body. See main definitions in Figure 4.1.

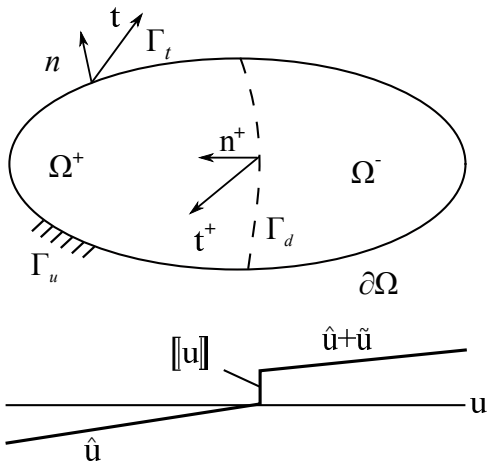

Figure 4.1: Strong discontinuity (Dias-da-Costa et al., 2009).

The total displacement field, $\mathbf{u}$, is considered as the sum of the field of regular displacements, $\hat{\mathbf{u}}$, with the enhanced displacement field, $\tilde{\mathbf{u}}$, the latter solely due to the presence of the discontinuities within the body. Accordingly, the total virtual displacement can be written as:

$$\delta\mathbf{u}=\delta\hat{\mathbf{u}}+\mathscr{H}_{\Gamma_d}\delta\tilde{\mathbf{u}} \quad (4.2)$$

with

$$\mathscr{H}_{\Gamma_d}=\begin{cases}1 & \forall\ x\in\Omega^{+}\\ 0 & \text{otherwise}\end{cases} \quad (4.3)$$

Under the assumption of small displacements, the strain field can be written as:

$$\boldsymbol{\varepsilon} = \boldsymbol{\nabla}^{sym}\mathbf{u} = \boldsymbol{\nabla}^{\boldsymbol{sym}}\hat{\mathbf{u}} + \mathscr{H}_{\Gamma_d}\left(\boldsymbol{\nabla}^{sym}\tilde{\mathbf{u}}\right) + \delta_{\Gamma_d}\left(\llbracket\mathbf{u}\rrbracket \otimes \mathbf{n}^{+}\right)^{sym} \quad \text{in} \quad \boldsymbol{\Omega} \tag{4.4}$$

where δ_{Γ_d} is the Dirac's delta function over the discontinuity.

Following the assumption that the opening of discontinuities is transmitted to the neighbouring material as if it were a rigid body movement, i.e., $\nabla^{sym}\delta\tilde{\mathbf{u}} = 0$, and by replacing Equations (4.2) and (4.4) in Equation (4.1) and by taking progressively $\delta\tilde{\mathbf{u}} = 0$ and $\delta\hat{\mathbf{u}} = 0$, the following simplified equations are obtained:

$$\int_{\Omega\setminus\Gamma_d} (\boldsymbol{\nabla}^{\boldsymbol{sym}}\delta\hat{\mathbf{u}}) : \boldsymbol{\sigma}(\hat{\boldsymbol{\varepsilon}})d\Omega = \int_{\Omega\setminus\Gamma_d} \delta\hat{\mathbf{u}}\cdot\bar{\mathbf{b}}d\Omega + \int_{\Gamma_t} \delta\hat{\mathbf{u}}\cdot\bar{\mathbf{t}}d\Gamma \tag{4.5}$$

and

$$\int_{\Gamma_d} \delta\llbracket\mathbf{u}\rrbracket\cdot\mathbf{t}^{+}d\Gamma = \int_{\Omega^{+}} \delta\tilde{\mathbf{u}}\cdot\bar{\mathbf{b}}d\Omega + \int_{\Gamma_{t^{+}}} \delta\tilde{\mathbf{u}}\cdot\bar{\mathbf{t}}d\Gamma \tag{4.6}$$

4.2.2 Discretisation

In the following sections, two different options to discretise the previous set of equations are followed. In the first case, the use of interface elements is detailed, which can be a rather effective technique in situations where the discontinuity location is known in advance. This occurs when regions of contact between materials, such as FRP and concrete or reinforcements and concrete, need to be modelled. In the second section, elements with embedded discontinuities are addressed and these are the ones that can efficiently be used in the simulation of fracture, since the discontinuity location is not known in advance and typically does not propagate along the edges of the elements.

4.2.2.1 Interface elements

The formulation of an interface element can be found in several references reason why only the main steps are shown here (Kaliakin and Li, 1995; Schellekens and De Borst, 1993). The variational principle for an interface element can be derived from the general variational statement – see Equation (4.1) – by simply removing

all terms related to the bulk:

$$\int_{\Gamma_d} \delta[\![\mathbf{u}]\!] \cdot \mathbf{t}^+ d\Gamma = \int_{\Gamma_d} \delta\mathbf{u} \cdot \bar{\mathbf{t}} d\Gamma \tag{4.7}$$

where $[\![\mathbf{u}]\!]$ represents the opening of the discontinuity, $\mathbf{t}^+$ is the traction at the discontinuity and $\bar{\mathbf{t}}$ are the stresses distributed on the external surface of the body.

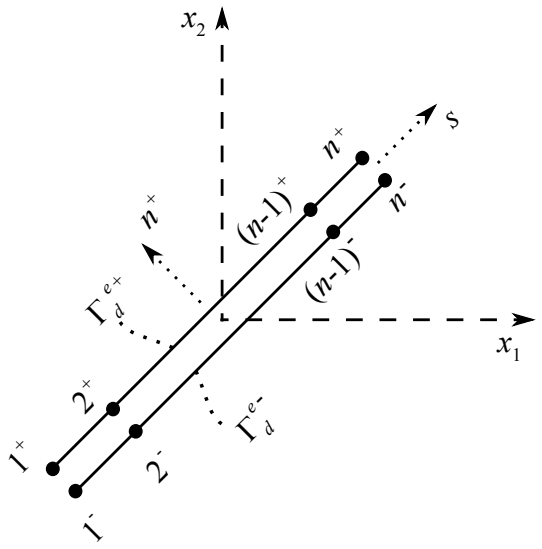

Figure 4.2: Interface elements with n pair of nodes (Dias-da-Costa, 2010).

Assuming the interface element to be composed by n pairs of nodes (see Figure 4.2), the following approximation is adopted for the displacement field within each finite element:

$$[\![\mathbf{u}]\!]^e = \left(\delta\mathbf{u}^{e+} - \delta\mathbf{u}^{e-}\right)|^e_{\Gamma_d} = \mathbf{N}^e_w \left[s(x)\right] \mathbf{w}^e \quad \text{at} \quad \Gamma^e_d \tag{4.8}$$

where $\mathbf{w}^e$ are the nodal jumps and $\mathbf{N}^e_w$ contains the interpolation functions applied to each pair of nodes i along the interface:

$$\mathbf{N}^e_w = \begin{bmatrix} \mathbf{N}^{e1}_w & 0 & \dots & \mathbf{N}^{en}_w & 0 \\ 0 & \mathbf{N}^{e1}_w & \dots & 0 & \mathbf{N}^{en}_w \end{bmatrix} \tag{4.9}$$

The incremental nodal jump is computed as:

$$d\mathbf{w}^e = \mathbf{L}_w d\mathbf{a}^e \tag{4.10}$$

in which $\mathbf{L}_w$ is a $(2n \times 4n)$ matrix defined as:

$$\mathbf{L}_w = \begin{bmatrix} 1 & 0 & -1 & 0 & \dots & 0 & 0 & 0 & 0 \\ 0 & 1 & 0 & -1 & \dots & 0 & 0 & 0 & 0 \\ \vdots & \vdots & \vdots & \vdots & \ddots & \vdots & \vdots & \vdots & \vdots \\ 0 & 0 & 0 & 0 & \dots & 1 & 0 & -1 & 0 \\ 0 & 0 & 0 & 0 & \dots & 0 & 1 & 0 & -1 \end{bmatrix} \tag{4.11}$$

and the incremental nodal displacements are defined according to:

$$d\mathbf{a}^{eT} = \begin{bmatrix} d\mathbf{a}_{1^+}^{eT} & d\mathbf{a}_{1^-}^{eT} & \dots & d\mathbf{a}_{n^+}^{eT} & d\mathbf{a}_{n^-}^{eT} \end{bmatrix} \tag{4.12}$$

The traction-jump law at discontinuity is used to obtain the tractions, from:

$$d\mathbf{t}^e = \mathbf{T}^e d[\![\mathbf{u}]\!]^e = \mathbf{T}^e \mathbf{N}_w^e d\mathbf{w}^e \quad \text{at} \quad \Gamma_d^e \tag{4.13}$$

in which $\mathbf{T}^e$ is the linearised constitutive relationship for the discontinuity.

The variational principle can now be discretised by means of the previous field approximations leading to:

$$\mathbf{K}_{aa}^e d\mathbf{a}^e = d\mathbf{f}^e \tag{4.14}$$

where $\mathbf{K}_{aa}^e$ is the interface element tangential matrix given by:

$$\mathbf{K}_{aa}^e = \int_{\Gamma_d^e} \mathbf{B}^{eT} \mathbf{T}^e \mathbf{B}^e d\Gamma \tag{4.15}$$

where $\mathbf{B}^e = \mathbf{N}_w^e \mathbf{L}_w$.

4.2.2.2 Embedded discontinuities

In the case of the DSDA, the displacement field within each finite element enriched with a discontinuity can be interpolated by (Dias-da-Costa, 2010; Dias-da-Costa et al., 2009):

$$\mathbf{u}^e = \mathbf{N}^e(\boldsymbol{x}) \left(\hat{\mathbf{a}}^e + \mathscr{H}_{\Gamma_d}^e \tilde{\mathbf{a}}^e \right) \quad \text{in} \quad \Omega^e \setminus \Gamma_d^e \tag{4.16}$$

$$[\![\mathbf{u}]\!]^e = \mathbf{N}_w^e \left[s(\boldsymbol{x})\right] \mathbf{w}^e \quad \text{at} \quad \Gamma_d^e \tag{4.17}$$

in which $\mathbf{N}^e$ corresponds to the element shape functions, $\hat{\mathbf{a}}^e$ are the nodal freedom degrees related to $\hat{\mathbf{u}}^e$, $\tilde{\mathbf{a}}^e$ are the enhanced nodal freedom degrees related to $\tilde{\mathbf{u}}^e$, $\mathbf{N}_w^e$ are shape functions and $\mathbf{w}^e$ are the degrees of freedom at both ends of discontinuity. Figures 4.3 and 4.4 show respectively the normal jump and shear band caused by discontinuity.

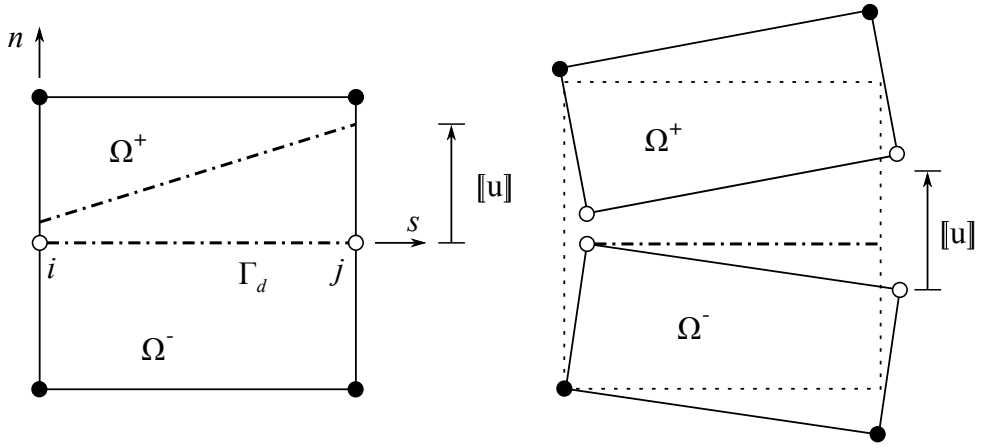

Figure 4.3: Normal opening in a four node element crossed by a discontinuity (Dias-da-Costa et al., 2009).

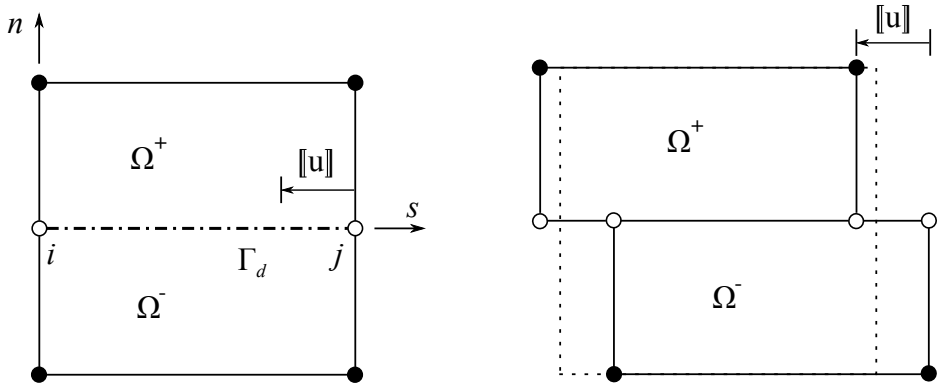

Figure 4.4: Shear band opening in a four node element crossed by a discontinuity (Dias-da-Costa et al., 2009).

The enhanced nodal displacement resulting from the displacement jumps caused by the discontinuity on the surrounding neighbourhood can be assumed as a rigid body

movement computed by:

$$\tilde{\mathbf{a}}^e = \mathbf{M}_w^{ek}\mathbf{w}^e \tag{4.18}$$

where $\mathbf{M}_w^{ek}$ is obtained by stacking in rows the following matrix:

$$\mathbf{M}_w^{e\,T} = \begin{bmatrix} 1 - \frac{(x_2 - x_2^i)\sin\alpha^e}{l_d^e} & \frac{(x_1 - x_1^i)\sin\alpha^e}{l_d^e} \\ \frac{(x_2 - x_2^i)\cos\alpha^e}{l_d^e} & 1 - \frac{(x_1 - x_1^i)\cos\alpha^e}{l_d^e} \\ \frac{(x_2 - x_2^i)\sin\alpha^e}{l_d^e} & -\frac{(x_1 - x_1^i)\sin\alpha^e}{l_d^e} \\ -\frac{(x_2 - x_2^i)\cos\alpha^e}{l_d^e} & \frac{(x_1 - x_1^i)\cos\alpha^e}{l_d^e} \end{bmatrix} \tag{4.19}$$

where (x_1, x_2) are the coordinates of a material point inside the element and α^e and l_d^e are the angle and length of the discontinuity, respectively, as seen in Figure 4.5.

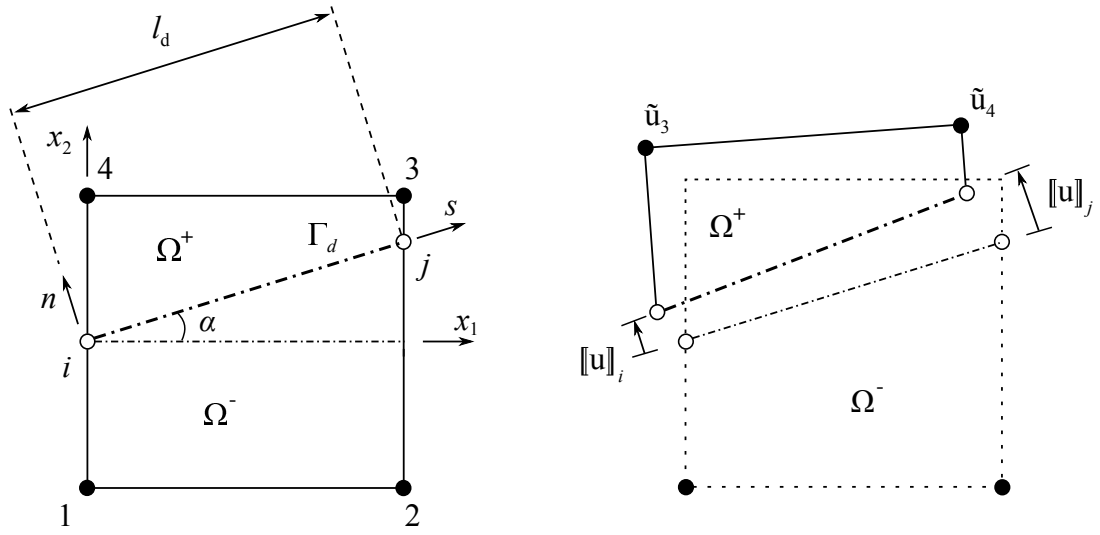

Figure 4.5: Rigid body motion $\tilde{\mathbf{u}}$ caused by discontinuity jumps (Dias-da-Costa et al., 2009).

The regular strain filed is computed by:

$$\hat{\boldsymbol{\varepsilon}}^e = \mathbf{B}^e(\boldsymbol{x})\hat{\mathbf{a}}^e = \mathbf{B}^e\left(\mathbf{a}^e - \mathbf{H}_{\Gamma_d}^e\mathbf{M}_w^{ek}\mathbf{w}^e\right) \quad \text{in} \quad \Omega^e \setminus \Gamma_d^e \tag{4.20}$$

in which $\mathbf{B}^e = \mathbf{L}\mathbf{N}^e$ with $\mathbf{L}$ being the usual differential operator, $\mathbf{a}^e$ are the nodal total obtained displacements and $\mathbf{H}_{\Gamma_d}^e$ is the diagonal matrix containing the Heaviside function calculated for each regular degree of freedom of the element.

The incremental stress field is obtained from:

$$d\boldsymbol{\sigma}^e = \mathbf{D}^e\mathbf{B}^e\left(d\mathbf{a}^e - \mathbf{H}^e_{\Gamma_d}\mathbf{M}^{ek}_w d\mathbf{w}^e\right) \quad \text{in} \quad \Omega^e \setminus \Gamma^e_d \tag{4.21}$$

where $\mathbf{D}^e$ is the tangent stiffness matrix for the bulk.

The tractions at discontinuity are found from the traction-jump law:

$$d\mathbf{t}^e = \mathbf{T}^e\mathbf{N}^e_w d\mathbf{w}^e \quad \text{at} \quad \Gamma^e_d \tag{4.22}$$

in which $\mathbf{T}^e$ is the tangent stiffness matrix for the discontinuity.

Finally, the previous equations can be used to discretise the variational principle in Equations (4.5) and (4.6), which can then be recast as:

$$\begin{bmatrix} \mathbf{K}^e_{\hat{a}\hat{a}} & -\mathbf{K}^e_{aw} \\ 0 & \mathbf{K}^e_d \end{bmatrix} \begin{Bmatrix} d\mathbf{a}^e \\ d\mathbf{w}^e \end{Bmatrix} = \begin{bmatrix} d\hat{\mathbf{f}}^e \\ d\mathbf{f}^e_w \end{bmatrix} \tag{4.23}$$

where

$$\mathbf{K}^e_{aw} = \mathbf{K}^e_{\hat{a}\hat{a}}\mathbf{H}^e_{\Gamma_d}\mathbf{M}^{ek}_w \tag{4.24}$$

and $\mathbf{K}^e_{\hat{a}\hat{a}}$ and $\mathbf{K}^e_d$ are, respectively, the stiffness for the regular FE and discontinuity, $\mathbf{K}^e_{aw}$ is the coupling matrices, and $\hat{\mathbf{f}}^e$ and $\mathbf{f}^e_w$ are the nodal forces, the latter defined by:

$$d\mathbf{f}^e_{w,ext} = d\mathbf{f}^e_w - \left(\mathbf{H}^e_{\Gamma_d}\mathbf{M}^{ek}_w\right)^T d\hat{\mathbf{f}}^e_{ext} \tag{4.25}$$

When all forces are applied exclusively at the nodes of the elements, then it can be shown that $\mathbf{f}^e_w = 0$.

4.2.3 Solution procedure

Solving the system of equations shown in Equation (4.23) requires handling several sources of material non-linearities, such as concrete cracking and crushing, the yielding of steel reinforcements, and the progressive debond along steel- and FRP-concrete interfaces. For this purpose, there are several methods that can be used for obtaining a solution. The *Newton-Raphson* is an incrementally-iterative method

such that within each step of incremental load, the unbalanced forces due to constitutive/material non-linearities are progressively reduced at each iteration. This technique, is quite established and has been improved giving rise to different modified approaches – e.g., the *Modified Newton-Raphson*, *Quasi-Newton* or *Conjugate Newton* (Graça-e-Costa, 2012). There are, however, many situations where more advanced path-following constraints are required to overcome more complex load-displacement curves, such as the ones found in the case of brittle and quasi-brittle materials. One example is the *arc length* method, where specific constraints can be used to deal with severe non-linearities. By using this technique, it becomes possible to enforce the crack growth or even the monotonic growth of the energy dissipated during the analysis (Gutiérrez, 2004; Verhoosel et al., 2009). Yet, even these more advanced techniques often fail to converge and provide reliable solutions in the presence of severe material non-linearities, such as the ones typically found in the simulation of discrete fracture. In these situations, new techniques, such as the *Sequentially Linear Approach* (SLA) or the non-iterative *automatic* method have been successfully proposed (Graça-e-Costa et al., 2013; Roots, 2001). Both methods are based on a series of linear analyses to model the non-linear behaviour without iterations (Graça-e-Costa et al., 2013). The latter method was herein adopted, since it was shown to be robust and provide reliable results with discrete embedded discontinuities (Graça-e Costa et al., 2012).

With the *automatic* approach, and before starting the analysis, all constitutive models are discretised into multilinear branches, hence avoiding the need to iterate at the constitutive level. Each step of analysis is then composed of a trial step, followed by a true step. The trial step starts with load being applied to the structure and the selection of the solution sense. A standard energy criterion is used to find the solution leading to the highest energy release rate (Gutiérrez, 2004; Verhoosel et al., 2009). If no bifurcation points are found during this analysis, meaning that all integration points follow admissible constitutive paths, the trial step becomes the true step and a new step is initiated. In the presence of bifurcation points, transition is made to a total approach, such that the damage is enforced to grow on the points following inadmissible paths. This reduction is defined *a priori* (Graça-e-Costa et al., 2013) A detailed description of the method can be found in Graça-e Costa et al. (2012); Graça-e-Costa et al. (2013).

4.2.4 Constitutive models

This section presents the constitutive models adopted for the simulation of interfaces and discrete cracks.

4.2.4.1 FRP-concrete bond

The interface between concrete and FRP can be modelled using the interface elements formulated earlier equipped with suitable constitutive models. The choice of a constitutive model is a fundamental issue in strengthened RC girders, since debonding of externally bonded FRP may lead to structural failure and this needs to be accurately predicted. There are several models available in the literature, e.g., MC 2010 (2010), Lu et al. (2005a), Lu et al. (2005b), Coronado and Lopez (2010), Benvenuti et al. (2012) or Marfia et al. (2012). The model proposed in MC 2010 (2010) is also used in CEB/FIB (2001) and was developed by Holzenkämpfer (1994). This model is bilinear – see Figure 4.6 – and relates the interface slip, s, with the local bond stress, τ, according to the following equations:

$$\tau = \tau_m \frac{s}{s_m} \quad \text{if} \quad 0 \leq s \leq s_m \tag{4.26}$$

$$\tau = \tau_m - \tau_m \frac{s - s_m}{s_u - s_m} \quad \text{if} \quad s_m \leq s \leq s_u \tag{4.27}$$

where s_m is local slip at maximum local bond stress, τ_m, and s_u is the ultimate local slip.

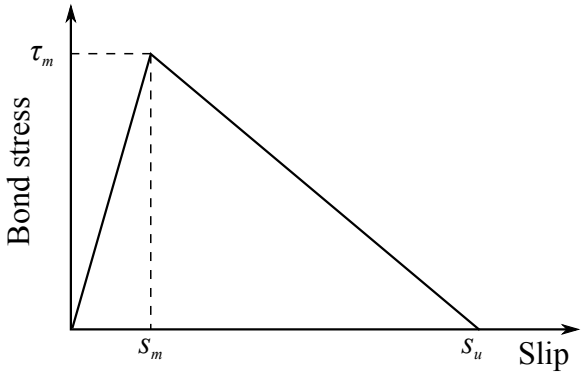

Figure 4.6: Bond stress-slip model (Holzenkämpfer, 1994).

As an alternative to the classical bilinear model presented in Holzenkämpfer (1994), another model proposed by Lu et al. (2005a) is regarded herein in its simplified form. Figure 4.7 (a) shows a comparison between bond-slip curves from a meso-scale FE simulation (Lu et al., 2005a) and the proposed model. From this comparison, it can be seen that the model is more accurate than the bilinear approach, particularly in the softening branch, which is critical for predicting debonding.

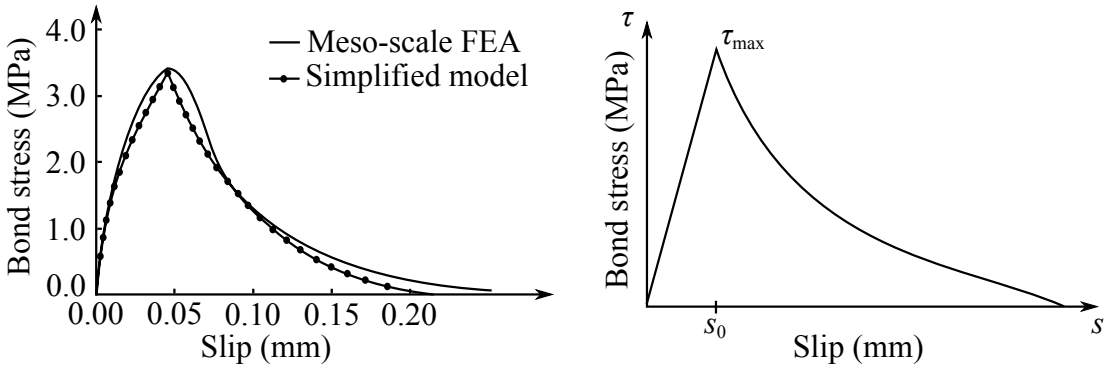

(a) (b)

Figure 4.7: Bond-slip model proposed by Lu et al. (2005a): (a) validation; and (b) bond stress-slip relationship.

The model is defined by the following equations (see Figure 4.7 (b)):

$$\tau = \tau_{max}\sqrt{\frac{s}{s_0}} \quad \text{if} \quad s \leq s_0 \tag{4.28}$$

$$\tau = \tau_{max} e^{-\alpha\left(\frac{s}{s_0}-1\right)} \quad \text{if} \quad s > s_0 \tag{4.29}$$

with

$$s_0 = 0.0195\beta_w f_t \tag{4.30}$$

$$G_f = 0.308\beta_w^2\sqrt{f_t} \tag{4.31}$$

$$\alpha = \frac{1}{\frac{G_f}{\tau_{max}s_0} - \frac{2}{3}} \tag{4.32}$$

$$\beta_w = \sqrt{\frac{2.25 - b_f/b_c}{1.25 + b_f/b_c}} \tag{4.33}$$

$$\tau_{max} = \alpha_1 \beta_w f_t \tag{4.34}$$

where τ_{max} is the maximum local bond stress, s is the local slip, s_0 is the local slip at τ_{max}, f_t is the concrete tensile strength, G_F is the interfacial fracture energy, b_f is the width of FRP plate and b_c is the width of concrete prism.

4.2.4.2 Discrete cracks

In terms of fracture, the use of discrete embedded discontinuities described earlier allows inserting the traction-separation law within each crack element. For this reason, the bulk material (the concrete) is modelled as linear elastic in tension, since the tensile non-linear behaviour will be solely due to the presence of cracks. It becomes critical to identify the moment when a new discontinuity localises or propagates. A simplified approach was herein adopted, where new crack fronts are introduced during the numerical analysis through the centre of each finite element whenever the first principal stress reaches the tensile strength of the material. In the same way, existing fronts are propagated when the first principal stress at the tip reaches the tensile strength of the material. The angle of propagation is always taken as orthogonal to the first principal stress and is kept constant during the analysis and after the onset of cracking. In reality, discontinuities are introduced in the analysis slightly before reaching the tensile strength of the material, typically at around 90% to avoid reaching stresses higher than the material capacity (Dias-da-Costa et al., 2009). As soon as a discontinuity is inserted, a high penalty stiffness is used with the purpose of keeping the discontinuity closed before the tensile strength of the material is finally reached. During this stage, the constitutive model of the discontinuity is given by:

$$\mathbf{t} = \mathbf{T}_{el}\mathbf{w} \tag{4.35}$$

with

$$\mathbf{T}_{el} = \begin{bmatrix} k_n & 0 \\ 0 & k_s \end{bmatrix} \tag{4.36}$$

where $\mathbf{t}$ is the traction vector, $\mathbf{w}$ is the jump vector, and k_n and k_s are the normal and the shear penalties, respectively.

The constitutive relation shown in the previous equations is also adopted in the case of crack closure to avoid the overlapping of crack faces. When the discontinuity opens, a simple mode-I law is followed with a loading function defined as follows (Dias-da-Costa, 2010):

$$f(w_n, \kappa) = w_n - \kappa \tag{4.37}$$

in which the internal variable κ is taken as the maximum normal relative displacement attained, $\max \langle w_n \rangle^+$ (and $\dot{\kappa} \geq 0$). If $f > 0$, loading takes place as well as the evolution of damage ($\dot{\kappa} > 0$), whereas if $f < 0$, closing of the crack occurs and damage does not grow ($\dot{\kappa} = 0$). Different softening laws can be chosen, being the bilinear and exponential laws the most commonly adopted. The bilinear softening is defined by (Rots et al., 1985):

$$t_n = f_{t0} - \frac{3 f_{t0}}{\varepsilon_u} \varepsilon_i \quad \text{if} \quad 0 \leq \varepsilon_i \leq \varepsilon_1 \tag{4.38}$$

$$t_n = \frac{3 f_{t0}}{7 \varepsilon_u} \left[\varepsilon_u - (\varepsilon_i - \varepsilon_1) \right] \quad \text{if} \quad \varepsilon_1 \leq \varepsilon_i \leq \varepsilon_u \tag{4.39}$$

with

$$\varepsilon_u = \frac{54}{15} \frac{g_f}{f_{t0}} \tag{4.40}$$

$$\varepsilon_1 = \frac{2 \varepsilon_u}{9} \tag{4.41}$$

$$f_{t1} = \frac{f_{t0}}{3} \tag{4.42}$$

in which f_{t0} is the initial tensile strength, ε_u is the ultimate strain, g_F results from the division of G_f by the applicable value in the smeared crack approach and ε_1 and f_{t1} are the inflection joint point in the softening.

For the exponential softening, the constitutive relation between the normal traction component, t_n, and the normal relative displacement between crack faces (normal jump), is given by:

$$t_n = f_{t0} e^{\left(-\frac{f_{t0}}{G_F} \kappa \right)} \tag{4.43}$$

where G_F is the fracture energy, defined as the amount of energy consumed for creating a unit area crack surface and f_{t0} is the initial tensile strength of the material.

During the progress of damage in mode-I, the elastic shear stiffness is progressively decreased proportionally to the mode-I secant stiffness.

4.3 Analytical model for flexural behaviour

The analytical model was developed to predict the ultimate load supported by the girder, using a cross-sectional analysis considering the stress-strain diagram shown in Figure 4.8. It was assumed a linear strain distribution over the girder depth and that initially plane sections remain plane after bending. Accordingly, the flexural moment is computed as follows:

$$M = F_c z_c + F_p z_p + F_f z_{fu} \tag{4.44}$$

where F_c is the compressive stress force in the concrete, z_c is the distance from the neutral axis, x, to the concrete force, F_p is the force due to prestressing strands, z_p is the distance between the prestressing strands and the neutral axis, F_f is the force due to CFRP and z_{fu} is the distance from the CFRP to the neutral axis.

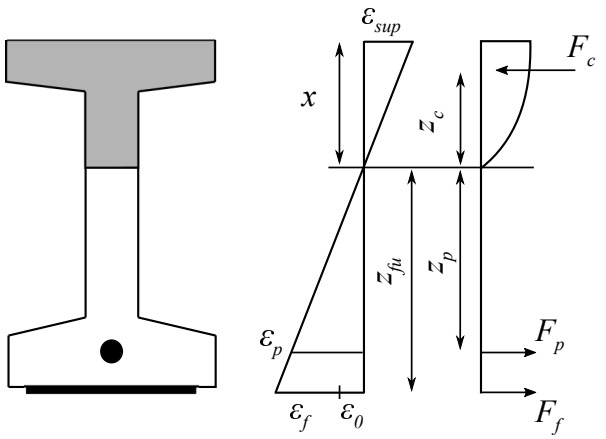

Figure 4.8: Stress-strain diagram for sectional analysis.

Concrete was modelled with the stress-strain relation for non-linear structural analysis from CEN (2004):

$$\frac{\sigma_c}{f_{cm}} = \frac{k\eta - \eta^2}{1 + (k-2)\eta} \tag{4.45}$$

with

$$\eta = \frac{\varepsilon_c}{\varepsilon_{c1}}$$

$$k = 1.05 E_{cm} \frac{|\varepsilon_{c1}|}{f_{cm}}$$

where ε_{c1} is the strain at peak stress according to CEN (2004), E_{cm} is the secant Young's modulus of concrete and f_{cm} is the mean of concrete cylinder compressive strength. Additionally, it should be highlighted that the concrete tensile capacity was neglected.

The balance of forces was determined through an iterative process by enforcing the compatibility while searching for the neutral axis position. This process included two main steps: i) the first was the state before applying the CFRP, where the concrete strain at the bottom fibre was calculated for dead loads; and ii) at failure, where the ultimate moment was calculated. This two-step approach assured that the strengthening process stages of a damaged girder could be properly considered. Failure was assumed to occur when the CFRP fails or when the concrete crushes, after the yielding of prestressing steel, whichever occurs first. The adopted calibration process is summarised in the following:

Before applying the CFRP

1. compute the initial strain at the bottom of the girder:
   (a) estimate the flexural moment, M_E, given by dead loads at strengthening;
   (b) select an initial value for the neutral axis position;
   (c) perform the iterative process to find the balance of forces when the flexural moment, M_G, equals M_E, according to the *Newton-Raphson* method. At each iteration $n+1$, strains are updated using the following relation based on the previous iteration n:

$$\varepsilon_{sup_{n+1}} = \varepsilon_{sup_n} - \left(\frac{N}{\partial N / \partial \varepsilon_{sup}} \right)_n \tag{4.46}$$

   where $N = F_c + F_p$ and ε_{sup} is the strain at the top of the girder.
   (d) after the equilibrium is reached within a certain range, the initial strain at the bottom of the girder, ε_0, is calculated;

After applying the CFRP

2. calculate the ultimate moment at failure:

   (a) select an initial value for the neutral axis position;

   (b) identify the proper failure mode, first by assuming the upper strain to match the ultimate compressive strain in concrete and by computing the strain at CFRP level; if the latter strain is smaller than the CFRP strain limit, design is controlled by concrete crushing. Otherwise, CFRP rupture governs failure. The strain at the CFRP level can be determined according to:

$$\varepsilon_f = \varepsilon_{cu}\frac{z_{fu}}{x} - \varepsilon_0 \tag{4.47}$$

   (c) perform the iterative process having into account the initial strain at the bottom of the girder calculated in the previous step to estimate the strain at the prestressing strand level:

$$\varepsilon_p = \varepsilon_{cu}\frac{z_p}{x} \tag{4.48}$$

   (d) after reaching the equilibrium conditions, determine the ultimate moment, M_R.

4.4 Application example

The models described previously were validated through an application example described in this section, consisting in PC girders produced on a 1/2 scale and experimentally tested until failure. This example is considered to be representative of the problem studied in this thesis.

4.4.1 Description

The experimental data is based on results from Fernandes (2005) and Fernandes et al. (2013). The experiments were conducted on high strength concrete (HSC)

girders, considering: i) non-CFRP strengthened girders – see Figure 4.9; and ii) a CFRP strengthened girder – see Figure 4.10.

(a) (b)

Figure 4.9: Experimental test of HSC girder: (a) test set-up; and (b) failure (Fernandes, 2005).

(a) (b)

Figure 4.10: Experimental test of CFRP strengthened HSC girder: (a) test set-up; and (b) failure.

The beams had an 'I' shaped cross section, as illustrated in Figure 4.11, with a height of 500 mm and a web width of 75 mm. The upper and bottom flanges were 300 mm wide and had a thickness ranging from 60 to 65 mm and 75 to 100 mm, respectively. The active reinforcement was composed by twelve 3/8" prestressing bounded strands at bottom and two 3/8" unbounded post-tension strands at top. The pre- and post-tension strands were initially submitted to tensile stresses of 1430 MPa and 1160 MPa at the age of 5 days.

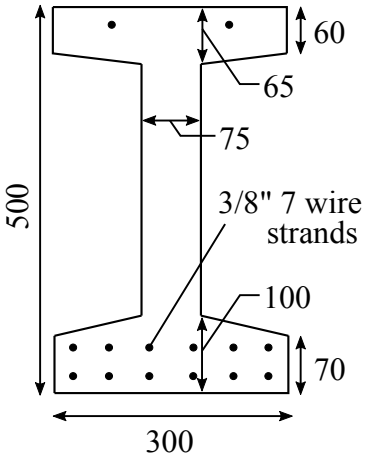

Figure 4.11: Cross-section of the girder (mm) (Fernandes, 2005).

The non-strengthened flexural tests were carried out using two beams at 106 and 131 days of age, whereas the CFRP strengthened test was performed at 7 years of age using one beam. In the strengthened situation, CFRP laminates were anchored at the ends using steel plates and these consisted on two CFK 150/2000 laminates with rectangular cross-sections of 100×1.4 mm^2. In all cases, the specimens were loaded on a four-point bending scheme, as shown in Figure 4.12.

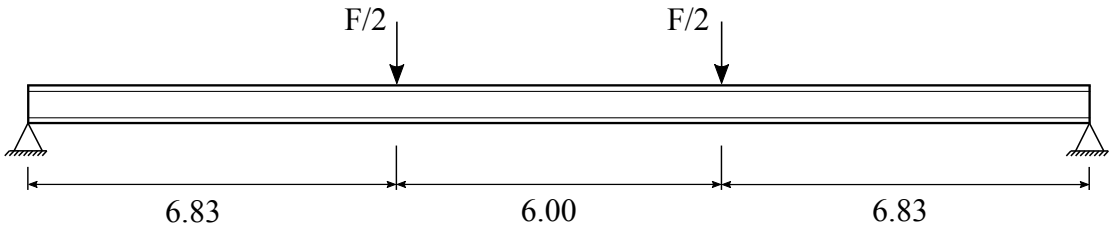

Figure 4.12: Scheme of load and boundary conditions of experimental tests (m) (Fernandes, 2005).

4.4.2 Numerical model

Material properties

The properties for all materials are presented in Table 4.1. The Young's modulus and yield stress of steel reinforcement and prestressing strands were experimentally measured (Fernandes, 2005), whereas the properties of CFRP were adopted according to

the manufacturer (Fernandes et al., 2013). The compressive strength and Young's modulus of concrete were also experimentally obtained, but the fracture energy was estimated according to MC 90 (1991). In terms of constitutive behaviour, the prestressing strands and stirrups were modelled considering a perfect elasto-plastic law, whereas a linear elastic law until failure was adopted for the CFRP laminates. Concrete was considered to follow an elasto-plastic behaviour under compression, according to CEN (2004), and a bilinear softening envelop for fracture as described earlier (see Section 4.2.4.2).

Table 4.1: Material properties for numerical models.

Parameter	Value	Source
Concrete compressive strength, f_{cm}	120 MPa	Fernandes (2005)
Concrete tensile strength, f_{ctm}	5.52 MPa	Fernandes (2005)
Concrete Young's modulus, E_{cm}	59.0 GPa	Fernandes (2005)
Fracture energy, G_f	0.20 N/mm	MC 90 (1991)
Tensile strength of prestressing steel, f_p	1915 MPa	Fernandes (2005)
Prestressing Young's modulus, E_p	200 GPa	Fernandes (2005)
Steel reinforcement tensile strength, f_{ys}	604 MPa	Fernandes (2005)
Steel reinforcement Young's modulus, E_s	192 GPa	Fernandes (2005)
CFRP ultimate strength, f_f	2300 MPa	Fernandes et al. (2013)
CFRP Young's modulus, E_f	165 GPa	Fernandes et al. (2013)

Interfaces

A perfect bond was assumed between concrete and reinforcements, whereas the interface between CFRP and concrete was modelled according to the simplified model proposed by Lu et al. (2005a) and described in Section 4.2.4.1. Laminates were considered to be anchored at both ends with a steel plate, according to Fernandes et al. (2013). The properties of the interfaces are presented in Table 4.2.

Elements and boundary conditions

Bilinear finite elements under a plane stress state were used to model concrete, whereas truss elements were used for prestressing strands, stirrups and CFRP. The resulting mesh – see Figure 4.13 – was composed by 1955 bilinear elements, 1257 and 1390 linear elements for the non-strengthened test and the CFRP-strengthened

Table 4.2: Properties of CFRP-concrete interface.

Parameter	Value	Source
Concrete tensile strength, f_{ctm}	5.52 MPa	Fernandes (2005)
Width of concrete prism, b_c	300 mm	Fernandes (2005)
Width of FRP plate, b_f	280 mm	Fernandes et al. (2013)
α_1	1.5	Lu et al. (2005a)

test, respectively, and 306 interface elements for the non-strengthened test and 439 interface elements for the CFRP strengthened test. Additionally, two load steps were considered: i) pre-stress loads (P_{n}); and ii) failure load (F).

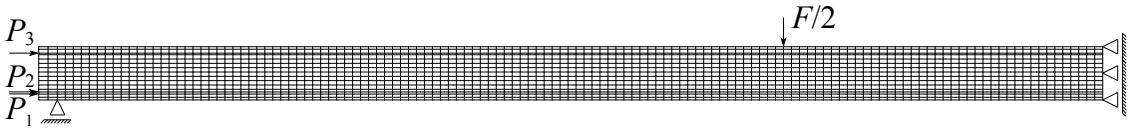

Figure 4.13: FE mesh.

4.4.3 Results

This section presents the main results obtained from the numerical and analytical analysis.

Load/deformation response

The load-displacement curves obtained for the numerical model are fairly close to the experimental envelop as shown in Figure 4.14. In the measurements of the non-strengthened beams – see Figure 4.14 (a) – the failure load is around 135 kN in both experimental tests and numerical simulation. The first cracks appeared at 60 kN, followed by the prestressing steel yielded at 105 kN. Additionally, concrete crushing was found to occur through the analysis of compressive stresses for a vertical mid-span displacement close to 450 mm. Concerning to the CFRP strengthened test – see Figure 4.14 (b) – results show that the ultimate load for the experimental and numerical model is close to 172 kN. Moreover, failure occurred due to concrete crushing after prestressing yield and no debonding of the CFRP was observed for either experimental and numerical analysis.

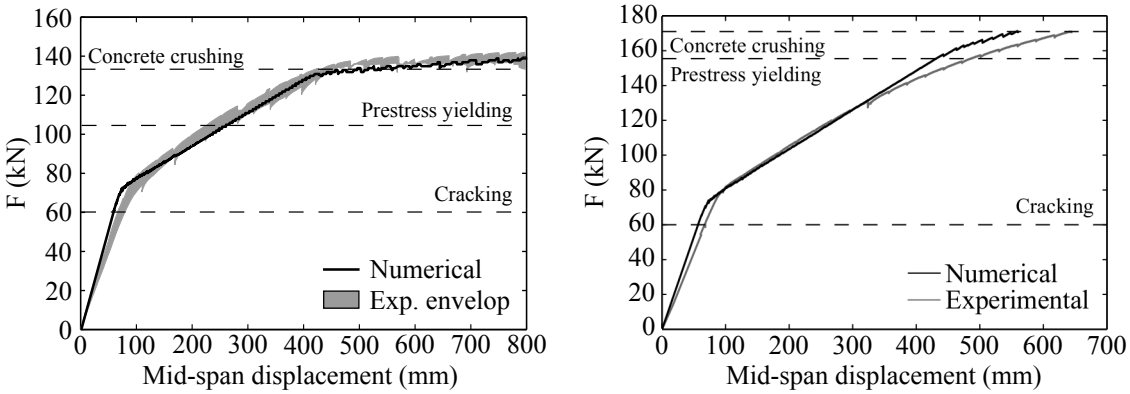

Figure 4.14: Load-displacement curves for: (a) non-strengthened girder; and (b) CFRP strengthened girder.

The analytical model was also validated using the same experiments. Results, present in Table 4.3, show the similarity between experimental and analytical ultimate moment, with a maximum difference of 5% between results.

Table 4.3: Ultimate moment of the girders (kN.m).

	Non-strengthened girder	CFRP strengthened girder
Experimental	558.58–575.63	685.02
Analytical model	576.31	717.20

Crack pattern

The deformed mesh and crack pattern for both non- and CFRP strengthened girders are shown, respectively, in Figures 4.15 and 4.16. As experimentally observed in both tests – Fernandes (2005) and Fernandes et al. (2013) – cracking propagated from the bottom flange and spread towards the web, with the major cracks localising at mid-span.

Computational time

Table 4.4 presents the computational time of each numerical analysis. All models were calculated on an AMD Phenom II X6 1090T, 3.2 GHz 6 cores with 6 MB L3

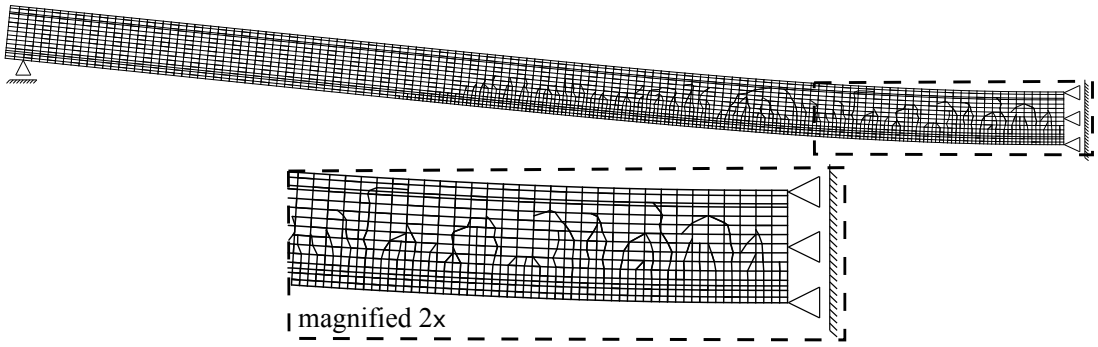

Figure 4.15: Deformed shape and crack pattern at failure of non-strengthened girder.

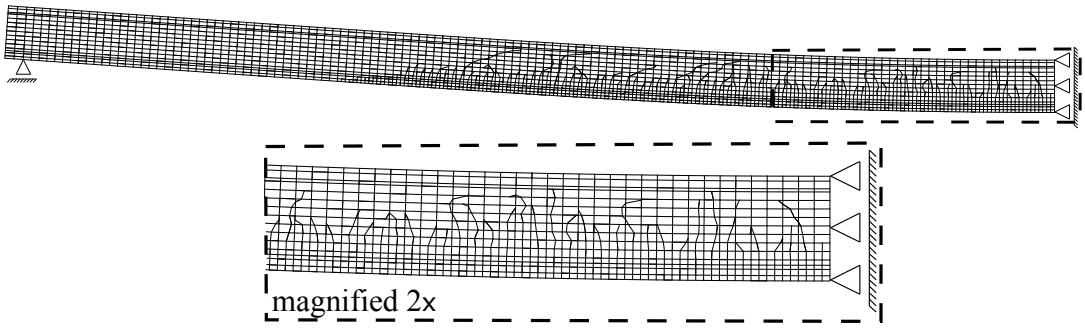

Figure 4.16: Deformed shape and crack pattern at failure of CFRP strengthened girder.

cache 125 W computer. Results show that the calculation time increases when the CFRP is included in the analysis. Nevertheless, when compared with the commercial software Abaqus (2010), the computational time is much smaller in spite of the level of detail in the analysis with discrete model. For instance, the Abaqus (2010) model considering the same mesh and the concrete damaged plasticity model needed more than 6 and 18 hours for the non-strengthened and CFRP strengthened girders respectively, whereas a three dimensional model for the non-strengthened girder exceeded 24 hours – see Gomes et al. (2011). On the other hand, the analytical model is quite fast and provides results in less than one minute.

Table 4.4: Computational time of the numerical analysis (hours).

Non-strengthened girder	CFRP strengthened girder
2:20	4:10

4.5 Conclusions

The analytical and numerical models used in this thesis were described in the present chapter. The models were aimed at predicting the behaviour of RC girders subject to bending and support reliability studies. Experimental results from HSC girders were used for validation purposes. The following main results are highlighted regarding the numerical models:

- the load/displacement curves are similar to the experimental results, including all main features, such as ultimate loads;
- the crack pattern is very realistic and resemble to what was observed during the experiments;
- the FRP-strengthened model requires twice the computational time than the non-strengthened model, but still keeps similar predictive features.

The analytical model based on cross-sectional analysis included several simplifications, which did not prevent from obtaining a good estimate on the ultimate moments. In spite of this, the numerical approach provides more realistic and comprehensive information regarding the non-linear structural response, including the interaction between cracks and CFRP. However, when a high number of analyses is required, such as for statistical analysis, the numerical models can become time-consuming and computationally demanding in comparison to analytical models. Based on this, numerical and analytical models are efficiently combined in Chapter 5, to compute the structural strength for the reliability based calibration of partial safety factors for CFRP. Then, in Chapter 6, only analytical models are used due to the computational time and resources available.

Chapter 5

Calibration of partial safety factors for CFRP

5.1 Introduction

The previous chapters have laid on the background needed for the reliability-based calibration of partial safety factors for CFRP. In this chapter, a calibration procedure of partial safety factors for CFRP of strengthened PC girders based on reliability tools is presented.

Over the years, several researchers have approached this issue. The first study focusing on reliability analysis of RC elements flexurally strengthened with FRP was carried out by Plevris et al. (1995). This study analysed rectangular beams used in buildings and CFRP debonding was neglected. Statistical properties of design variables were adopted from bibliography and models uncertainties were not used. FORM and MCS were adopted to compute structural reliability using analytical models. Results showed that the most relevant properties are concrete strength, CFRP ultimate strain and area (treated as deterministic). Considering a reliability index of 3.0, a general strength reduction factor of 0.85 (ϕ) and a reduction factor

for CFRP of 0.95 (ϕ_{f_c}) were proposed for the following equation:

$$\phi R_n(x_1, x_2, \ldots, \phi_{f_c}\varepsilon^*_{f_c}, \ldots, x_j) \geq \sum_k \gamma_k Q_k \tag{5.1}$$

in which R_n is the nominal strength, x_j are the design variables, $\varepsilon^*_{f_c}$ is the laminate failure strain, γ_k is the load partial factor and Q_k is the load effects. Moreover, for special cases when the partial reduction factor was assumed to be 1.0, the general strength reduction factor for CFRP was 0.80.

Reliability of larger members was studied by Okeil et al. (2002) and El-Tawil and Okeil (2002), by considering bridges with rectangular RC beams and 'I' shaped PC girders strengthened with CFRP, respectively. In both studies, an analytical model considering the material non-linearity and construction sequence, at a sectional level, was adopted. Three levels of damage, corresponding to the losses of 10%, 20% and 30% of the steel reinforcement area were analysed. For each level of damage, CFRP laminates were designed to restore the flexural capacity of the girders and debonding was not considered. All statistical properties of design variables were taken from other studies. Additionally, the CoV adopted for concrete was 0.18, which may be a very high value for PC, whereas a very low value was used for the CoV of CFRP ultimate strain – 0.022. MCS and FORM were used to calibrate the strength reduction factor for a reliability index of 3.75. A reduction factor of 0.85 was recommended by Okeil et al. (2002), whereas El-Tawil and Okeil (2002) suggested the following equation to determine the strength reduction factor:

$$\phi = 1.0 - \frac{M_{CFRP}}{M_{PS}} \geq 0.85 \tag{5.2}$$

where M_{CFRP} and M_{PS} are moments respectively carried by the CFRP and pre-stressing strands. Moreover, reliability was found to increase with the load carried by FRP; this was possible due to the low CoV used for FRP.

Atadero and Karbhari (2008), carried out a reliability study on RC T-beams strengthened with CFRP, to develop a methodology to calibrate reduction factors for flexural strengthening. Twenty bridges, representing the California State, United States of America, built between 1941 to 1976, were considered. FRP degradation and steel reinforcement corrosion were regarded. Debonding was considered based on a sim-

plistic analytical model using fracture energy. Statistical distributions of parameters were taken from bibliography, with the exception of CFRP strength, modulus and thickness. But, excessive CoV values were used for CFRP strength and modulus: 0.05 up to 0.30 and 0.20, respectively. Additionally, no models uncertainties were considered. FORM and MCS were used and different strength reduction factors were computed having into account three reliability indices of 2.5, 3.0 and 3.5. The results showed that the reliability of beams strongly depends on the amount of remaining steel and that the computed reduction factors for CFRP varied between 0.51 to 0.95.

Another study was performed by Pham and Al-Mahaidi (2008) on RC T-beams used for bridges and retrofitted with FRP. This was the first study to consider intermediate span and end debond failure modes, using analytical models. Model errors for debonding were developed and the remaining statistical properties were taken from bibliography. Concrete strength and FRP ultimate strength were assumed to have high CoV (0.20 and 0.12, respectively), and MCS and FORM were used. Two reduction factors were recommended for flexural failure and intermediate span debond, respectively, 0.6 and 0.5, for a target reliability of 3.25. The very low reduction factors reflect the large uncertainty that exists when dealing with FRP composites and debonding.

Paliga et al. (2011) made a reliability study on rectangular RC beams strengthened with CFRP. The results of undamaged, damaged and rehabilitated beams were assessed. To simulate the damaged beams, 30% of loss in tensile reinforcement area was assumed. FE analysis were considered to predict the structural resistance. However, the model was not detailed. MCS was used to compute the strength of the beams, which is a high demanding computational time procedure. It was observed that the debonding phenomenon had a significant influence in the failure load and that the obtained reliability indices for undamaged and rehabilitated beams were similar.

All the above research works were carried out on RC girders strengthened with FRP for studying its reliability and uncertainties influence, considering different cross sections and spans; for instance, Plevris et al. (1995) and Paliga et al. (2011) considered rectangular cross-sections, whereas El-Tawil and Okeil (2002) and Atadero

and Karbhari (2008) considered 'T' shaped cross sections and Okeil et al. (2002) and Pham and Al-Mahaidi (2008) considered 'I' shaped cross sections. MCS and FORM were performed in all studies, with the exception of Paliga et al. (2011) study, which did not use FORM. In these studies, MCS was used to compute the statistical resistance of the strengthened element, and FORM was used considering the random parameters of loads to compute structural reliability. This approach can be used when the number of random variables is high or when convergence is not reached just with FORM. In spite of MCS time requirements to compute small probabilities, the combination between both allows to save time. Moreover, different resistance reduction factors for FRP were suggested; when debonding is not considered, as in El-Tawil and Okeil (2001, 2002); Plevris et al. (1995), the reduction factors are less demanding. Besides, the target reliability and the CoV used to characterise the FRP properties also influences the resistance factors; a high CoV produces higher resistance factors, as in Pham and Al-Mahaidi (2008) that adopted a higher value of FRP strength CoV or in Atadero (2006). However, in spite of the efforts made, several limitations can be found, such as:

- the authors did not have access to reliable FRP statistical models; in fact, the only study that used statistical distributions proposed by the authors was carried out by Atadero and Karbhari (2008) – although, with small samples sizes (see Section 3.4);
- no degradation was considered in the studies from Plevris et al. (1995) and Pham and Al-Mahaidi (2008), when it is important for strengthening of existing structures. On the other hand, the studies conducted by Okeil et al. (2002), El-Tawil and Okeil (2002), Atadero and Karbhari (2008), Paliga et al. (2011) considered degradation by reducing the steel reinforcement area;
- all studies used analytical models at a sectional level, neglecting the remaining structural behaviour, with the exception of Paliga et al. (2011);
- Atadero (2006) was the only author that took into account the structural ageing. The remaining authors considered current codes to construct the studied cases;
- models uncertainties were neglected in all studies, with the exception of El-Tawil and Okeil (2001) and El-Tawil and Okeil (2002).

This chapter attempts to answer some limitations highlighted in the previous reliability studies and to describe a reliability-based partial safety factors calibration process for CFRP. First, Section 5.2 briefly introduces the most relevant existing design guidelines used for the design of strengthening with FRP. Then, the procedure used for the calibration of CFRP partial safety factors is discussed in Section 5.3. Finally, the results and main conclusions are drawn in Sections 5.4 and 5.5.

5.2 FRP strengthening design

During the last decades several design guidelines have been developed to support the standardisation of the use of externally bonded FRP. Some of the most widely used can be divided according to the area of representation as:

1 - Europe

Externally Bonded FRP Reinforcement for RC Structures - International Federation for Structural Concrete, (CEB/FIB, 2001). This guideline is in accordance with the CEN (2002a) philosophy;

Guide for the Design and Construction of Externally Bonded FRP Systems for Strengthening Concrete Structures - National Research Council, Advisory Committee on Technical Recommendations for Construction, (CNR, 2013);

2 - United Kingdom

Design Guidance for Strengthening Concrete Structures using Fibre Composite Materials - Technical Report No. 55, The concrete Society Committee, (TR-55, 2000);

3 - United States of America

Guide for the Design and Construction of Externally Bonded FRP Systems for Strengthening Concrete Structures - ACI 440.2R-08, American Concrete Institute, (ACI 440, 2008);

Guide Specifications for Design of Bonded FRP Systems for Repair and Strengthening of Concrete Bridge Elements - AASHTO, American Association of State Highway and Transportation Officials, (ASHTO, 2012);

4 - Canada

Strengthening reinforced concrete structures with externally-bonded fibre reinforced polymers - No. 4, ISIS Canada Corporation, The Canadian Network of Centres of Excellence on Intelligent Sensing for Innovative Structures (ISIS, 2001);

5 - Japan

Recommendations for upgrading of concrete structures with use of continuous fiber sheets - Concrete Series No. 41, Japanese Society of Civil Engineers, (JSCE, 2001).

The existing design guidelines follow similar approaches based on the limit state theory. According to the guideline, the safety or reduction factors are either applied to the overall resistance or to each different material, as respectively described:

$$\phi R(X_j) \geq \sum \gamma_i Q_i \tag{5.3}$$

and

$$\sum R\left(\frac{X_j}{\gamma_m}\right) \geq \sum \gamma_i Q_i \tag{5.4}$$

where ϕ is the general resistance factor, R is the function relating the properties to the strength, X_j are the nominal properties of materials, γ_m are the partial safety factors of each property, Q_i is the load effects and γ_i are the load partial safety factors. In Equation (5.3) the composite properties are affected by a reduction factor ϕ_f. Additionally, the former equation is used in ACI 440 (2008), ASHTO (2012) and ISIS (2001), whereas the last equation is used in CEB/FIB (2001), CNR (2013), TR-55 (2000) and JSCE (2001).

The corresponding design values used in the Equations (5.3) and (5.4) are respectively computed according to:

$$R_d = \phi R(X_j) \tag{5.5}$$

and

$$R_d = R\left(\frac{R_j}{\gamma_j}\right) \tag{5.6}$$

The latter values are determined using the safety (reduction) factor and the characteristic value. The former aims at taking into account several issues, such as environmental degradation, material properties, type of application, type of failure or manufacturing process, whereas the characteristic value is defined from tests results properties.

A summary of the requirements in terms of CFRP safety or reduction factors from CEB/FIB (2001), CNR (2013), TR-55 (2000), ACI 440 (2008), ASHTO (2012), ISIS (2001) and JSCE (2001) is shown in Table 5.1.

Table 5.1: Summary of safety or reduction factors.

Design guideline	Safety factor or reduction factor
CEB/FIB (2001)	γ_f= 1.20 to 1.35
CNR (2013)	γ_f= 1.10 to 1.50
TR-55 (2000)	γ_f= 1.10 to 3.50
ACI 440 (2008)	ϕ_f= 0.85 to 0.95
ASHTO (2012)	ϕ_f= 0.85
ISIS (2001)	ϕ_f = 0.75
JSCE (2001)	γ_f = 1.20 to 1.30

The choice partial safety factors according to CEB/FIB (2001) depends on the type of fibre (glass, aramid or carbon) and its application (prefabricated laminates or wet lay-up sheets), with safety factors for laminates being lower than for wet lay-up sheets. This approach can be easily explained, since the latter system typically presents higher uncertainties related with its application. In terms of the fibres, lower safety factors are found on carbon, whereas the glass are the ones presenting the highest safety factors.

The factors proposed in CNR (2013) depend on the type of failure (FRP rupture or debonding), being proposed higher safety factors for debond failure, since the associated strength models present higher uncertainties. When certification systems are in place, the safety factors can be smaller because the uncertainties are more limited.

TR-55 (2000) partial safety factors depend on the type of fibre (glass, aramid or carbon) and type of system (plates, sheets, tapes or prefabricated shells), and are

computed based on the following three set of factors:

$$\gamma_f = \gamma_{mf}\gamma_{mm}\gamma_{mE} \tag{5.7}$$

where γ_{mf} is the partial safety factor for the strength at the ultimate limit state, γ_{mm} is the partial safety factor for type of system and γ_{mE} is the partial safety factor for the Young's modulus at the ultimate limit state. The lowest factors are applied to carbon, whereas glass fibres have the highest factors.

The American guideline ACI 440 (2008) uses reduction factors instead of safety partial factors. The factors dependent on the type of fibre (glass, aramid, carbon) and the type of exposure conditions (interior, exterior – bridges, piers or open garages – or aggressive environments – chemical, plants and waste water treatment plants). This guideline considers the higher reduction factor for carbon and the lower for aramid. Moreover, as the environment conditions get more aggressive the reduction factors decrease. On the other hand, the American guideline ASHTO (2012) recommends a fixed value for factor of EBR FRP.

The reduction factor present in the Canadian guideline ISIS (2001) is based on the variability of the material characteristics, type of fibres (glass, aramid, carbon) and effect of sustained loads. Nevertheless, for all type of fibres the same factor is suggested.

The Japanese guideline JSCE (2001), recommends safety factors according to the type of verification: safety and restorability of serviceability. Furthermore, for safety and restorability the material factor varies according to the designer knowledge.

As it becomes clear from the previous paragraphs, all design guidelines provide different approaches for defining the partial safety factors. For instance, the CEB/FIB (2001) gives more importance to the type of fibre and application, whereas the CNR (2013) focus the type of failure and certification when defining the factors. The only guideline considering the environmental aspects is the American ACI 440 (2008). Additionally, ISIS (2001) considers only one reduction factor, whereas the JSCE (2001) does not present any criteria of choice rather than subjectivity.

The approach for specifying the characteristic values is similar in all codes, being this value defined based on a certain percentile from test results, with most guidelines setting a minimum of 20 to 30 experimental tests (Atadero, 2006). The characteristic values can be calculated using the following equation:

$$x_c = \mu_x - n\sigma_x \tag{5.8}$$

where x_c is the characteristic value, μ_x is the calculated mean, σ_x is the calculated standard deviation and n is a constant that varies according to the guideline – see Table 5.2. When n equals 1.64, this corresponds to the 5^{th} percentile assuming a normal distribution. It should be highlighted that characteristic values are defined for the ultimate tensile strength or strain, but the mean value is usually considered for the Young's modulus.

Table 5.2: Parameters used for calculating the characteristic values according to a guideline for normal distributions.

Design guideline	n
CEB/FIB (2001)	1.64
CNR (2013)	1.64
TR-55 (2000)	2
ACI 440 (2008)	3
ASHTO (2012)	1.22
ISIS (2001)	1.64
JSCE (2001)	3

5.3 Procedure of calibration

The procedure used for the calibration of the CFRP partial safety factors proposed herein and shown in Figure 5.1, was based on the current Portuguese structural context, in which a large number of RC structures were built during the last four decades using the Portuguese codes RSA (1983) and REBAP (1985). The visible ageing of these structural elements leads to the need of its strengthening, often using FRP and designed according to CEN (2002b) – the European code that is replacing the national one. This procedure follows the technique described in Gayton et al. (2004) and has as main objective the optimisation of the partial safety

factors for CFRP of RC girders, γ_f.

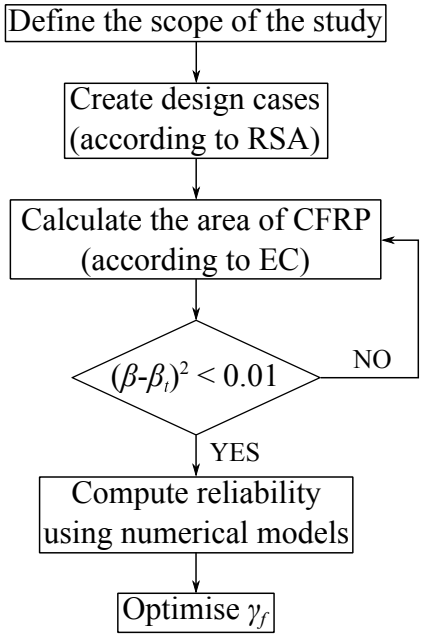

Figure 5.1: Calibration procedure flowchart.

The three first steps are related with design procedures. The first step is to define the scope of study. The definition of type of structures or failure mode helps limiting the range of cases to which partial safety factors will be applied to. Moreover, a structural reliability study depends on many distinct factors, such as structural elements or materials, among others. Its definition are of utmost importance to compute proper results for each situation. The range of calibration of this study was limited to PC girders of concrete bridges, that were strengthened using CFRP laminates.

The second step is to set ordinary design cases that may be representative of the calibration range. In this case, the selected bridges were designed according to the Portuguese code RSA (1983).

The next step is to include the CFRP laminates in the design. This process is executed taking into account the European code CEN (2002b). This option was adopted since the Portuguese code – RSA (1983) – is being replaced by the European code. The area of CFRP is calculated so that the reliability index can reach the demands of CEN (2002a). Further details about designs procedures are described in Section 5.3.1.

The fourth step consists in computing the reliability for each case using the software FERUM, followed by the optimisation of partial safety factors for CFRP, γ_f. Both steps are discussed in Section 5.3.2.

5.3.1 Range of calibration

The calibration range was restricted to PC girders used for roadway bridges. The studied example is illustrated in Figure 5.2. It consisted in a bridge with three girders, with one traffic lane in each direction and one side-walk on each side. Three bridges were designed using the Portuguese codes RSA (1983) and REBAP (1985) to link mid-size towns in Portugal (with around 150.000 citizens). The resistance was calculated using the analytical model described in Section 4.3, whereas the design loads were computed using a routine created for Matlab (Hanselman, 2013). A summary of the resistances (M_{Rd}) and loads (M_{Sd}) used for design is shown in Table 5.3.

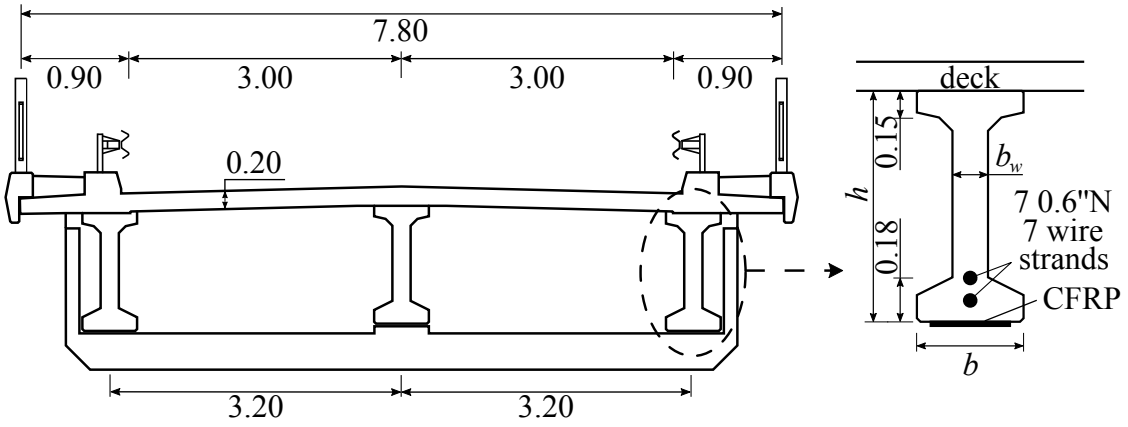

Figure 5.2: Bridge cross-section and details of the exterior girder (m).

Table 5.3: Summary of bridges design.

Bridge	M_{Rd} (kN.m)	M_{Sd} (kN.m)
B13	1942.36	1919.13
B16	2798.28	2792.14
B19	3654.21	3629.24

The most unfavourable girder was considered for the study, which corresponded to

an exterior beam. All girders were 'I' shaped and designed using PC. The active reinforcement consisted in two prestressing bounded strands composed by seven 0.6"N strings submitted to a tensile stress of 1200 MPa. Additionally, simple supported girders with spans, L, varying between 13.0 to 19.0 m were taken into account. The geometry of girders is presented in Table 5.4, whereas the material properties are described in Table 5.5.

Table 5.4: Geometry of girders (m).

Bridge	h	b	b_w	L
B13	0.6	0.4	0.15	13.0
B16	0.9	0.6	0.20	16.0
B19	1.2	0.6	0.20	19.0

Table 5.5: Materials properties of girders.

Property	Value
Concrete compressive strength, f_{cm}	43.0 MPa
Concrete tensile strength, f_{ctm}	3.2 MPa
Concrete Young's modulus, E_{cm}	34.0 GPa
0.1% proof-stress of prestressing steel, $f_{p0.1}$	1640.0 MPa
Prestressing Young's modulus, E_p	200.0 GPa
Steel reinforcement strength, f_y	500.0 MPa
Steel reinforcement Young's modulus, E_s	200.0 GPa
CFRP strength, f_f	2300.0 MPa
CFRP Young's modulus, E_f	165.0 GPa

For each design case, six levels of damage were considered by assuming the loss of prestressing strands area. The levels of lost area accounted for representative scenarios of damage, e.g., corrosion or vandalism. Thus, the lost areas were 10%, 20% and 30% of the total area of one level (Dx) or both levels (2Dx) of strands, as summarised in Table 5.6.

The calibration was be performed for a target reliability, β_t, of 4.3. According to CEN (2002b) this value corresponds to a level of high economical, social and environmental consequences, the one appropriated for bridges.

The rehabilitation or upgrade process of the PC girders was considered to be done

Table 5.6: Cases of structural deterioration.

Case	% of steel lost	A_p (mm^2)
D0	0	2240
D1	10	2142
D2	20	2044
D3	30	1946
2D1	2×10	2044
2D2	2×20	1848
2D3	2×30	1652

using CFRP laminates properly anchored at the ends. Since the weakest point in EBR FRP concrete elements is the bond layer between concrete and FRP, the use of an anchorage device allows to prevent premature failures and to obtain the maximum benefit from the CFRP strengthening (Spadea et al., 1998). This topic is important for the calibration process of the partial safety factors of FRP, since only the failure mode associated with FRP rupture was taken into account. Thus, in accordance with the case of study presented in Section 4.4, a steel plate anchorage was considered – see Figure 5.3. The number of laminates and steel plates is directly dependent on the generated study cases. Moreover, the use of this type of anchorages has proven to prevent premature debonding by several studies (e.g., Garden and Hollaway (1998); Quantrill and Hollaway (1998)).

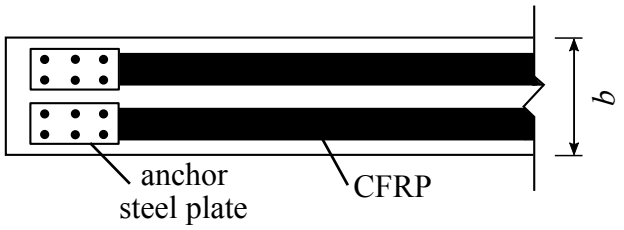

Figure 5.3: Steel plates anchorage.

5.3.1.1 Traffic load models

Different codes use distinct load models for traffic, commonly described either by concentrated loads or uniformly distributed loads. The loads intensity used in each code should reflect the real loading conditions that are practised in a country.

Two load models were used in this thesis: i) RSA (1983); and ii) CEN (2002b). The choice of these models was related with the fact that currently the majority of bridges built in Portugal during the last 40 years were designed using the Portuguese RSA (1983) and that presently this code is being replaced by the European CEN (2002b). The models used herein are described in the following:

RSA (1983)

The traffic models defined in this code were developed in the 1960s. The code considered two load models: i) the vehicle load; and ii) the knife load – see Figures 5.4 and 5.5, respectively. The vehicle model consists of three concentrated loads representing a three-axle vehicle and corresponding dynamic effects. The knife model is composed by a uniformly distributed load and a knife load. The characteristic values are presented in Table 5.7, where Class 1 and Class 2 correspond to intense and light traffic scenarios. The load should be placed at the most unfavourable position of the bridge deck.

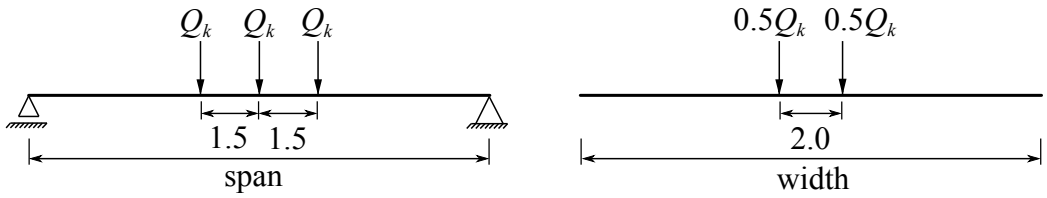

Figure 5.4: RSA vehicle model of highway traffic loads (m) (RSA, 1983).

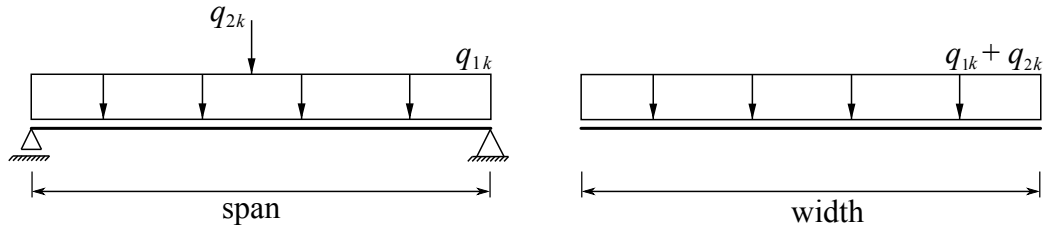

Figure 5.5: RSA knife model of highway traffic loads (RSA, 1983).

CEN (2002b)

The European code CEN (2002b) was developed in the 1980s. The principal load model (LM1) is shown in Figure 5.6. Loads should be placed at the bridge deck according to lanes of 3 meters each across the bridge width. The most unfavourable

Table 5.7: Characteristic values of RSA (1983) loads.

Bridge class	Concentrated load Q_k (kN)	Distributed load q_{1k} (kN/m^2)	Distributed load q_{2k} (kN/m)
Class 1	200	4.0	50
Class 2	100	3.0	30

one corresponds to Lane 1, whereas the second most unfavourable is Lane 2 and the third most unfavourable is Lane 3, etc. Furthermore, the model is composed by two concentrated loads representing two-axle vehicles and distributed loads. The characteristic values, presented in Table 5.8, already consider the dynamic effects.

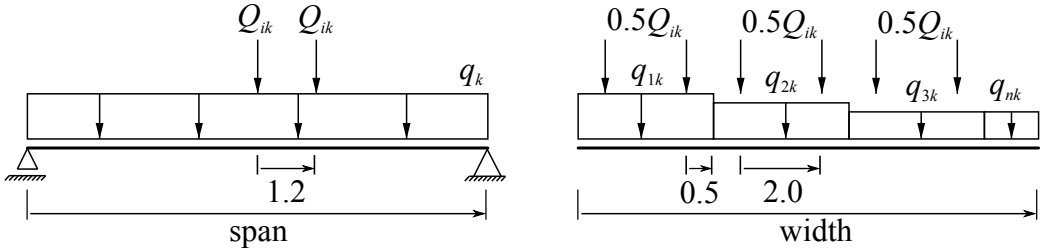

Figure 5.6: EC principal model (LM1) of highway traffic loads (m)(CEN, 2002b).

Table 5.8: Characteristic values of CEN (2002b) loads.

Location	Concentrated loads Q_{ik} (kN)	Distributed loads q_{ik} (kN/m^2)
Lane 1	300	9.0
Lane 2	200	2.5
Lane 3	100	2.5
Other lanes, n	0	2.5
Remaining area	0	2.5

Comparison of traffic models

The comparison of the two previous models assumes significance since the Portuguese code RSA (1983) is being replaced by the European CEN (2002b). Figure 5.7 shows the bending moment as a function of bridge length. As shown, the bending moment calculated according to CEN (2002b) – EC – is much higher than the one calculated according to any models from RSA (1983). Moreover, the knife

model is the one that presents lower bending moments. Table 5.9 shows the ratio between girders live and dead moments for the RSA (1983) vehicle and CEN (2002b) models. The live load moment was calculated considering the live loads from each code, whereas dead load moment was calculated having into account the loads due to self-weight, sidewalks, guard rail and asphalt. For both examples the importance of live load moment is higher when the span length is lower.

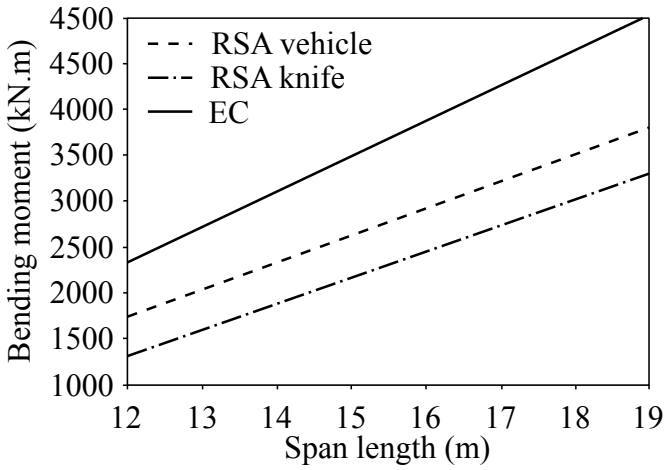

Figure 5.7: Bending moment for different load models.

Table 5.9: Comparison of bending moments according to RSA (1983) and CEN (2002b).

Bridge	M_L/M_D	
	RSA	EC
B13	2.00	3.01
B16	1.45	2.25
B19	1.20	1.92

Results indicate that bridges designed using RSA (1983) do not satisfy the requirements of CEN (2002b), having a lower safety margin. Nevertheless, this does not mean that the bridges designed according RSA (1983) are not safe. Furthermore, it is important to highlight that the models used in RSA (1983) have already 50 years and were developed in a different economic environment. On the other hand, the load models developed for CEN (2002b) considered countries from the centre of Europe, where traffic is more intense than in the peripheral countries, such as Portugal.

In this thesis, the option to use both codes seemed to be a reasonable choice since the bridges made in the last 40 years at Portugal were designed using RSA (1983), that presents lower load demands when compared with the European CEN (2002b). For this reason the last code was used for the strengthening design.

5.3.1.2 Numerical models

The adopted models were obtained by scaling the model validated with experimental results in Section 4.4. Two load steps were considered: i) a step for applying prestressing and dead loads, to account for the existing strain at the bottom of the girder before applying the CFRP; and ii) a step for the traffic loads after CFRP strengthening. The deck of the bridge was also included. Figure 5.8 shows the typical load-displacement curve from numerical results. Failure occurred by the rupture of the CFRP, following stirrups and prestressing steel yield. No debonding was observed since the CFRP was anchored at the ends. Moreover, concrete did not crush due to the area of the deck, which reduces the compressive stresses particularly when compared with the originally validated model.

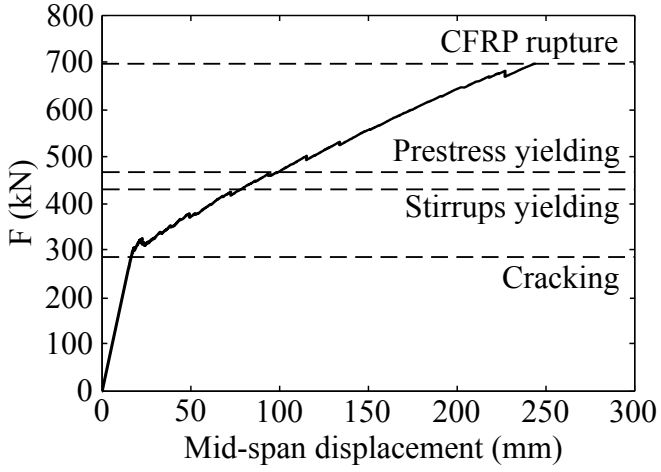

Figure 5.8: Typically load-displacement curve for the studied cases.

The typical crack patterns over the girder are illustrated in Figure 5.9. Concrete cracking started at a 20 mm vertical displacement at mid-span, and cracks begun to form first at mid-span. At the moment of failure, the crack pattern practically extended to half of the girder length. It should be emphasised that not all cracks

shown in the maps are effectively active; in fact, only few tend to be active and propagate through the web.

5.3.2 Reliability analysis

Reliability analysis were performed using the First Order Reliability Method (FORM) (Melchers, 1999) combined with the Response Surface Method (RSM) (Bucher, 2009). The software FERUM (Finite Element Reliability using Matlab) was used to run the FORM, whereas RSM was implemented in Matlab (Hanselman, 2013).

The structural safety performance was measured according to reliability index, β, and failure probability, P_f. The limit state function, G, was set as the difference between the resistance and standardised traffic loads, as follows:

$$G = \gamma_{mtl} - \gamma_{tl} \tag{5.9}$$

where γ_{mtl} is the maximum traffic load scale factor supported by the girder obtained using the analytical and FE models and γ_{tl} is the regulatory traffic load scale factor. The model uncertainties were considered according to:

$$G = \gamma_{mtl}(\theta_E) \times \theta_R - \gamma_{tl} \tag{5.10}$$

where θ_R is the resistance model uncertainty and θ_E is the load model uncertainty. The resistance uncertainty was directly multiplied by the scale factor, whereas the load uncertainty was assigned to numerical model to affect not only the traffic loads but also the remaining loads.

The maximum traffic scale factor was obtained from the analytical or the numerical models ultimate load, being a function of all remaining random variables, including dead loads. Thus, the limit state function can be described as:

$$G = \gamma_{mtl}(\theta_E; v_1; v_2; v_3; ...; v_n) \times \theta_R - \gamma_{tl} \tag{5.11}$$

where v are the statistical variables.

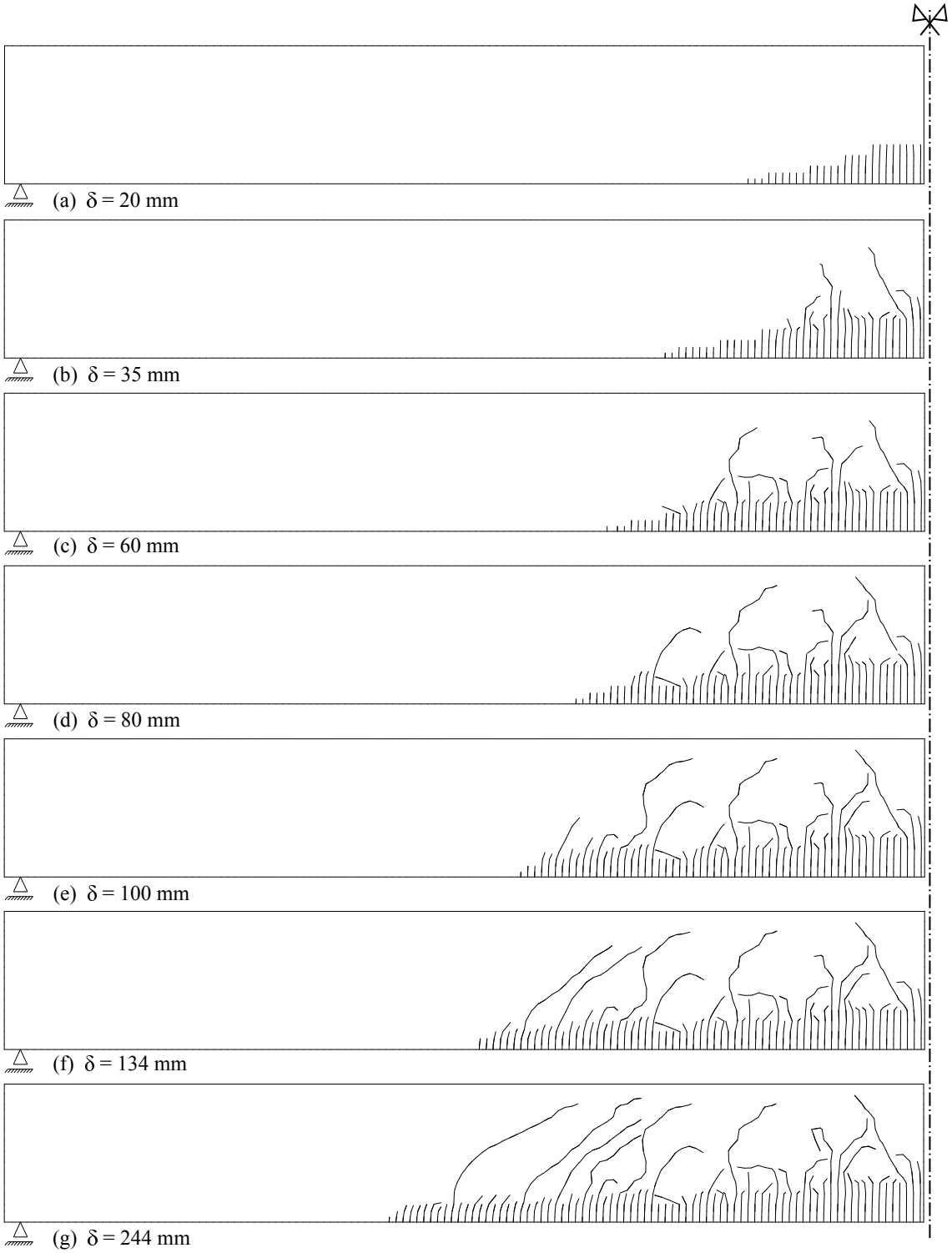

Figure 5.9: Crack pattern for different values of mid-span vertical displacement.

5.3.2.1 Random variables

The use of numerical models for reliability analysis is a high computational demanding task. Thus, the number of random variables should be minimised, to keep the cost at an acceptable level, as much as possible.

Existing studies showed that the concrete compressive strength, f_c, concrete Young's modulus, E_c, and prestressing Young's modulus, E_p, are not relevant variables for this type of analysis, whereas prestressing strength, f_p, CFRP strength, f_f, resistance model uncertainties, θ_R, traffic loads, γ_{tl}, dead loads, γ_{dl}, concrete self-weight, γ_c, and load model uncertainties, θ_E, are relevant variables (Gomes et al., 2014a,b).

In this thesis, the resistance model was described by the prestressing strength, f_p, CFRP strength, f_f, and resistance model uncertainties, θ_R. On the other hand, the load model was described by traffic loads scale factor, γ_{tl}, dead loads, γ_{dl}, concrete self-weight, γ_c, and load model uncertainties, θ_E. Table 5.10 summarises the probabilistic models described in the following.

Table 5.10: Statistical properties of random variables used in reliability analysis.

Variable	Units	Mean	Standard deviation	Distribution type
Prestressing strength, f_p	MPa	1674.0	50.0	Normal
CFRP strength, f_f	MPa	2686.4	207.77	Weibull
Resistance model uncertainties, θ_R	-	1.0	0.10	Log-normal
Traffic loads, γ_{tl}	-	0.84	0.084	Gumbel
Dead loads, γ_{dl}	kN/m	10.37	1.04	Normal
Concrete self-weight, γ_c	kN/m^3	25.0	1.0	Normal
Load model uncertainties, θ_E	-	1.0	0.10	Log-normal

Prestressing strength

The prestressing strength was characterised according to Jacinto et al. (2012). In this study, distributions were fit for 131 samples tested in Laboratório Nacional de

Engenharia Civil (LNEC). A normal distribution with a CoV of 3% was adopted.

CFRP strength

CFRP strength was considered in line with Gomes et al. (2013), described in Chapter 3.

Traffic loads

For statistical purposes the characteristic values of the traffic loads, Q, were assumed to have a normal distribution according to Vejdirektoratet (2004). Considering that the nominal values corresponded to a 95^{th} quantile and that the bridge lifetime horizon was defined as 50 years, the maximum loads tended asymptotically for a Gumbel distribution with mean and standard values (Ang and Tang, 2007) as:

$$\mu = u_n + \frac{\gamma}{\alpha_n} \tag{5.12}$$

$$\sigma = \frac{\pi}{\sqrt{6}\alpha_n} \tag{5.13}$$

where γ is the Euler of 0.57722, n is the time in years, u_n is the shape parameter and α_n is the scale parameter.

The characteristic value of traffic loads from Gumbel distribution was found according to the following equation:

$$\mu_{tl} = \frac{Q_k}{1 + 1.866V_{tl}} \tag{5.14}$$

where μ_{tl} and V_{tl} are respectively the mean and the CoV of Q_k.

In this thesis the problem was simplified by assuming that the 95^{th} percentile loads scale factor was equal to 1, regardless the nature of traffic load. A Gumbel distribution and a CoV of 0.10 were adopted (Wisniéwski, 2007).

Dead loads

Dead loads corresponding to the weight of the sidewalks, guard rail and asphalt were

considered to be uniformly distributed over the girder with a mean of 10.37 kN/m. A normal distribution and a CoV of 0.10 were considered in agreement with Vejdirektoratet (2004).

Concrete self-weight

Concrete self-weight was considered to be 25 kN/m^3. A normal distribution with a CoV of 0.04 was considered (JCSS, 2001).

Model uncertainties

The statistical parameters for both model uncertainties were adopted following the JCSS (2001). These variables have into account either the uncertainties that are not considered and which affect the model behaviour or the unknown suitability of the model for the required reasons. For both variables a log-normal distribution with 0.10 of CoV was taken into account.

5.3.2.2 Analysis procedure

A hybrid process was taken into account through the consideration of analytical and numerical models. The adoption of this method allows to save time, given the high demands of the computational effort needed for each numerical analysis – see Section 4.4.3. Thus, in a first cycle, the analytical models were adopted to perform the CFRP strengthening area calculation, by limiting the analysis at a sectional level. At this stage the non-linear structural behaviour is not relevant yet. Then, the numerical models were used to compute the CFRP partial safety factors used as reference for the optimum partial safety factor calculated according to what described in Section 5.3.2.3. These models allow to account the non-linear behaviour existing in FRP strengthened PC girders. The proposed procedure is described in the following and shown in Figure 5.10.

Firstly, the analysis domain and objectives are outlined, consisting in the definition of calibration range (Section 5.3.1), the analytical and numerical models (Chapter 4), the limit state function (Section 5.3.2), all parameters and statistical variables (Section 5.3.2.1) and the reliability objective by an expected target reliability index.

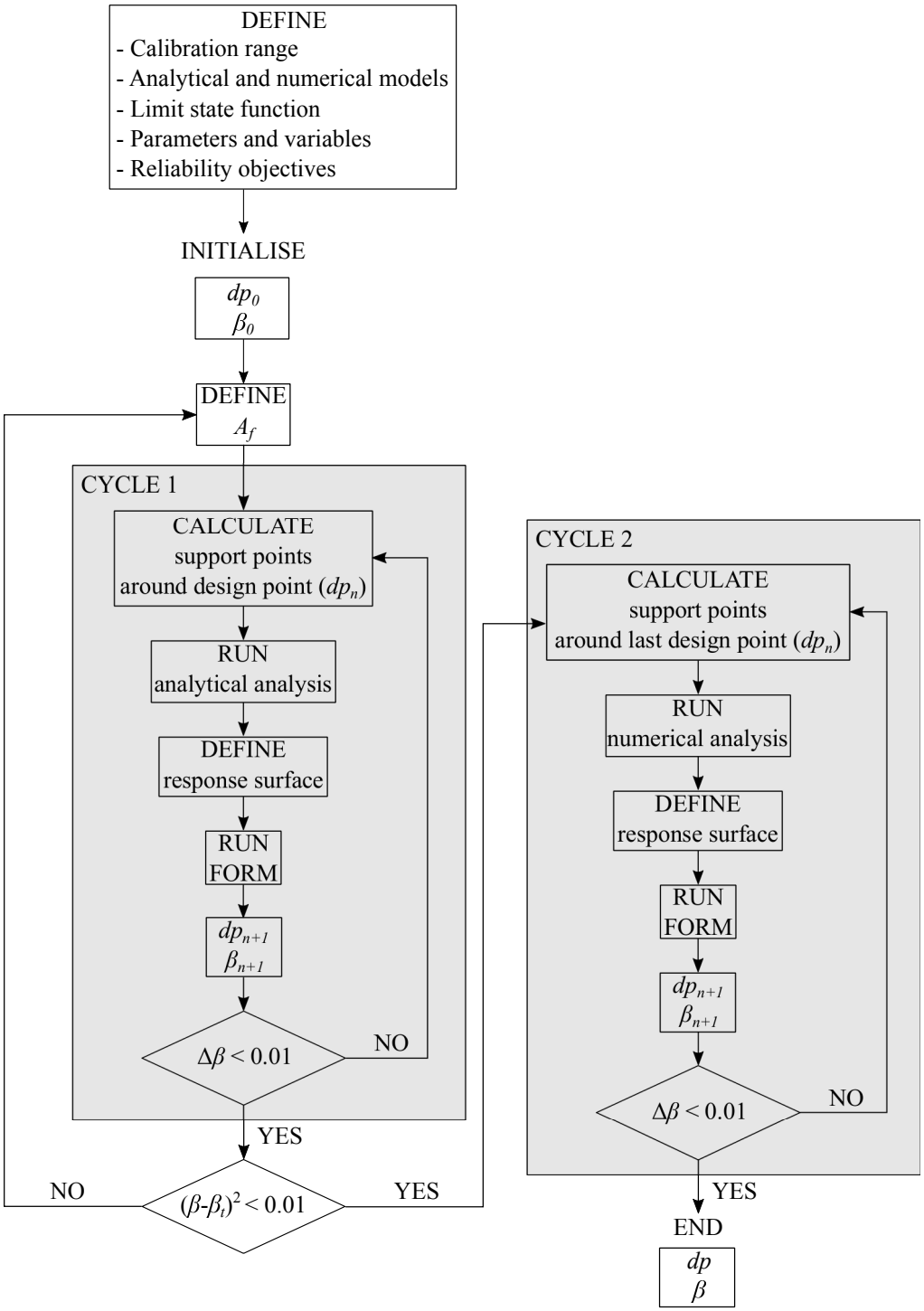

Figure 5.10: Reliability analysis procedure flowchart.

1st cycle

The first cycle consists in the calculation of the strengthening area of CFRP, A_f. It starts with the initialisation of the design points, dp_0, and reliability index, β_0, by assuming the mean values of the random variables and a target reliability index of 4.3, according to CEN (2002a). Then, the RSM (described in Section 2.3.4) is used to define the response surface for FORM analysis, by obtaining a close response to the maximum load scale factor at the design point, dp_n; in the approach used herein the response was calculated around the design and support points. For the studied case, since five random variables were considered to define the surface, ten support points were taken into account around the design point.

The analytical models are then used to run all the analysis necessary to define the response surfaces. Subsequently, FORM analysis are performed and new design points, d_{n+1}, and reliability index, β_{n+1}, are computed. This procedure is repeated until convergence is reached, defined as a reliability index relative change between iteration (smaller than 1%). Each time convergence is not reached, the new response surface is calculated based on the last computed design points.

This first cycle ends by checking if the area of CFRP can satisfy the objective of reaching the target reliability index. If the square of the difference between the reliability index and target reliability index is below 1%, the objective is achieved. Otherwise, the CFRP area needs to be adjusted and the first cycle needs to be repeated until the target reliability index is attained.

2nd cycle

The second cycle is similar to the previous, but numerical models are considered at this stage, and the analysis starts from the last computed design points. The procedure is repeated until convergence is reached. The outputs are the reliability index, β, and the design points, dp. The CFRP partial safety factors computed with the numerical models results are used as reference for the calibrated partial safety factor calculated according to what described in the next section.

5.3.2.3 Calibration process of partial safety factors for CFRP

The objective of the calibration process – see Figure 5.11 – is to compute reliability-based CFRP partial safety factors, γ_f, presented in a format suitable to implementation in codes. By this, the presented factor is obtained using analytical models and related with the partial safety factors obtained with numerical models and described previously. In the end, the optimum partial safety factor is calculated based on the results from all cases.

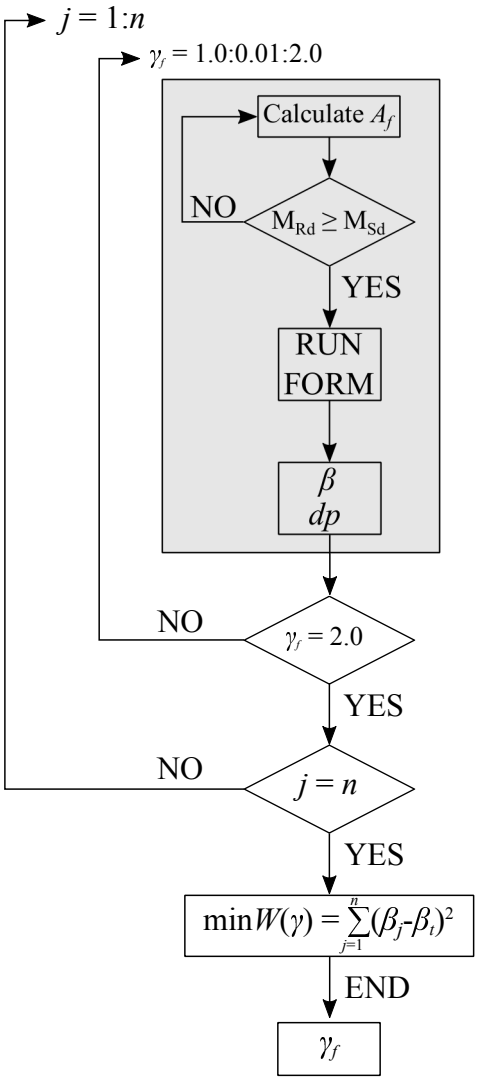

Figure 5.11: Optimisation procedure flowchart.

The calibration process, presented in Figure 5.11, consists in the search of the CFRP

partial safety factor that leads to the reliability index closest to the target reliability. The process starts by the CFRP area calculation needed for the design, having into account the mandatory partial safety factors for prestressing strength, concrete compressive strength, dead loads and live loads – 1.15, 1.50, 1.35 and 1.50 – and by assuming the value of the CFRP partial safety factor to vary between 1.0 and 2.0. Then, for each case, the reliability index is computed and for each girder a plot such as presented in Figure 5.12 is obtained. After all design cases are treated, i.e., $j = n$, the optimum CFRP partial safety factor is computed according to Faber and Sorensen (2002), by undertaking the subsequent condition:

$$\min W(\gamma) = \sum_{j=1}^{n} (\beta_j - \beta_t)^2 \tag{5.16}$$

in which γ is the calibrated partial safety factor and n is the number of studied cases, i.e., girders.

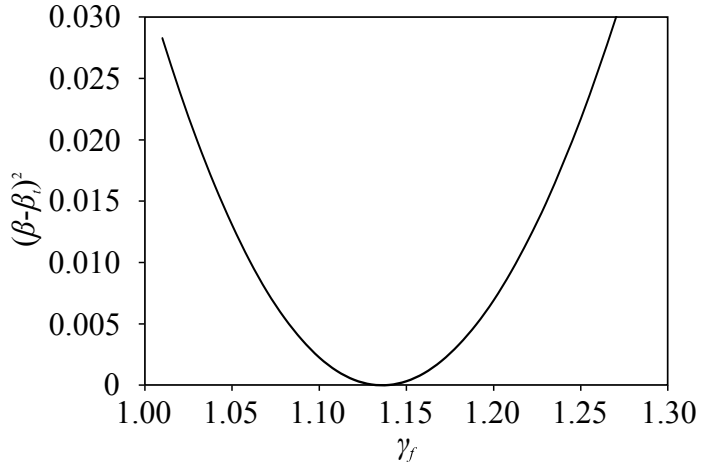

Figure 5.12: Example of plot used for calibration.

5.4 Results

The presented results are organised according to the two following stages of procedure: i) prior to the CFRP reinforcement area calculation – non-strengthened

girders; and ii) after the calibration procedure – strengthened girders.

5.4.1 Non-strengthened girders

Figure 5.13 shows the variation of reliability index, β, as a function of prestressing area, A_p, for RSA (1983) and CEN (2002b). In both cases, the reliability index increases with the amount of prestressing area. However, and as expected, reliability values shown in Figure 5.13 (a) are higher than the ones shown in Figure 5.13 (b), for the same level of prestressing area. In some cases, these differences can reach more than 200%, as seen when A_p is 1652 mm^2. For A_p equal to 2240 mm^2, it reaches 63%. These differences are related with the traffic load models recommended in the codes and that are more demanding in the CEN (2002b). Additionally, results show that reliability is strongly influenced by the prestressing area.

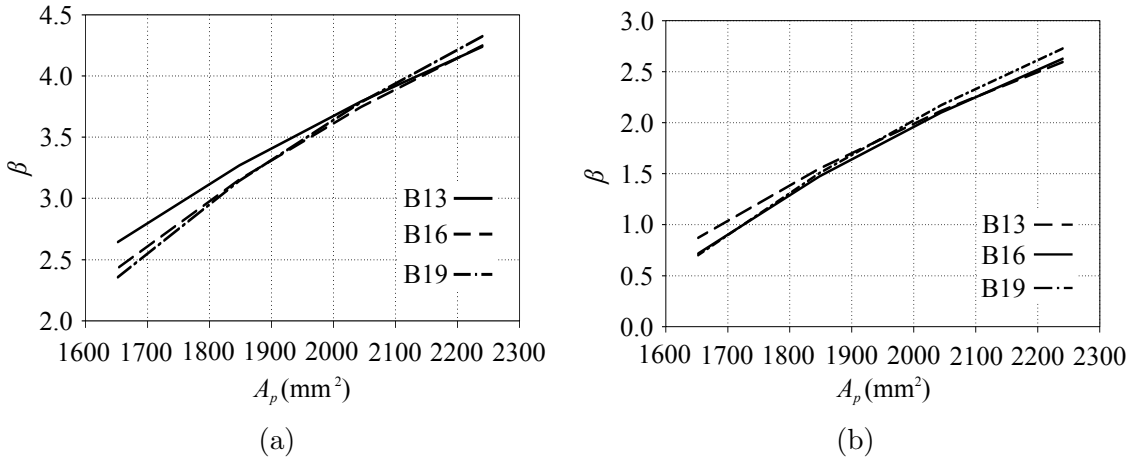

Figure 5.13: Variation of β as a function of A_p when using: (a) RSA (1983); and (b) CEN (2002b).

Figure 5.14 shows the sensitivity plot for both traffic load models. The most important variable is the traffic load, γ_{tl}, followed by the load and resistance uncertainties, θ_E and θ_R. The dead loads, γ_{dl}, and the concrete self-weight, γ_c, show a reduced influence in general. The prestressing strength, f_p, shows a sensitivity factor close to 0.18. Additionally, in spite of the traffic load models differences already described, results between codes are similar.

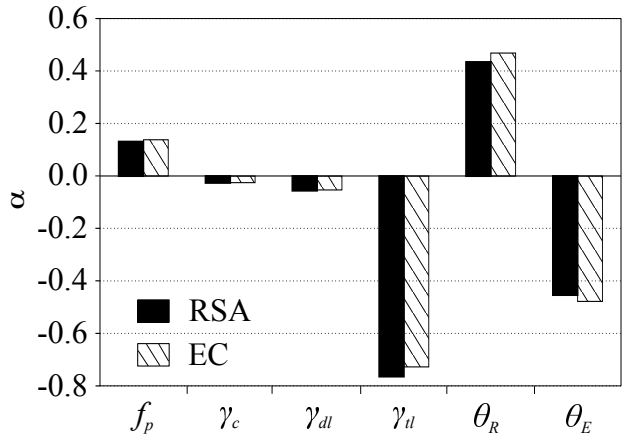

Figure 5.14: Cosines direction at design point using RSA (1983) and CEN (2002b).

The results presented here strengthen the fact that RSA (1983) is less conservative than CEN (2002b), as previously described in Section 5.3.1.1.

5.4.2 Strengthened girders

5.4.2.1 Strengthening area

The CFRP area was calculated according to what described in the first cycle of the procedure in Section 5.3.2.2. The computed areas for each case are summarised on Table 5.11.

The area of CFRP assures the girders to have sufficient flexural capacity to resist the code loads. In the most degraded situations, e.g., B13-2D3, the strengthening can increase the flexural capacity of the girders up to 74%, restoring its capability of full use according to the CEN (2002b) requirements. On the other hand, when the girders are not damaged the flexural capacity is upgraded to a maximum of 25%, reflecting the increment given by CEN (2002b) provisions. The high capacity restored is related to the fact that the girders were initially designed using the RSA (1983) and then repaired considering the CEN (2002b).

Table 5.11: Summary of bridges for calibration.

Bridge	% of steel loss	A_p (mm^2)	A_f (mm^2)	Flexural resistance (kN.m)	
				Initial	Strengthened
B13	0	2240	477	2352.1	2902.2
B13-D1	10	2142	531	2238.8	2903.8
B13-D2	20	2044	586	2125.1	2907.7
B13-D3	30	1946	641	2011.1	2913.9
B13-2D1	2×10	2044	586	2135.0	2907.5
B13-2D2	2×20	1848	688	1916.4	2922.0
B13-2D3	2×30	1652	781	1696.4	2944.6
B16	0	2240	453	3336.4	4181.4
B16-D1	10	2142	508	3173.9	4186.4
B16-D2	20	2044	570	3011.0	4194.2
B16-D3	30	1946	625	2847.8	4202.2
B16-2D1	2×10	2044	563	3020.9	4192.8
B16-2D2	2×20	1848	672	2703.9	4213.4
B16-2D3	2×30	1652	781	2385.4	4254.1
B19	0	2240	445	4353.5	5445.9
B19-D1	10	2142	508	4140.2	5453.0
B19-D2	20	2044	563	3926.4	5463.4
B19-D3	30	1946	625	3712.3	5477.7
B19-2D1	2×10	2044	563	3936.3	5440.8
B19-2D2	2×20	1848	680	3517.6	5471.8
B19-2D3	2×30	1652	789	3097.4	5533.2

5.4.2.2 Sensitive analysis

The relative importance of the seven random variables considered in the reliability study is discussed herein. Results are based on the cosines direction at design points in the normalised space – see Figures 5.15, 5.16 and 5.17, regarding bridges B13, B16 and B19, respectively. Moreover, for each random variable the several different cases scenario of prestressing loss are presented. The bar at leftmost corresponds to the highest prestressing area level and the bar at the rightmost corresponds to the lowest prestressing steel level.

As previously discussed in Section 5.4.1, traffic loads, γ_{tl}, play a fundamental role in the analysis once its importance reaches almost -0.80 in some cases. Furthermore,

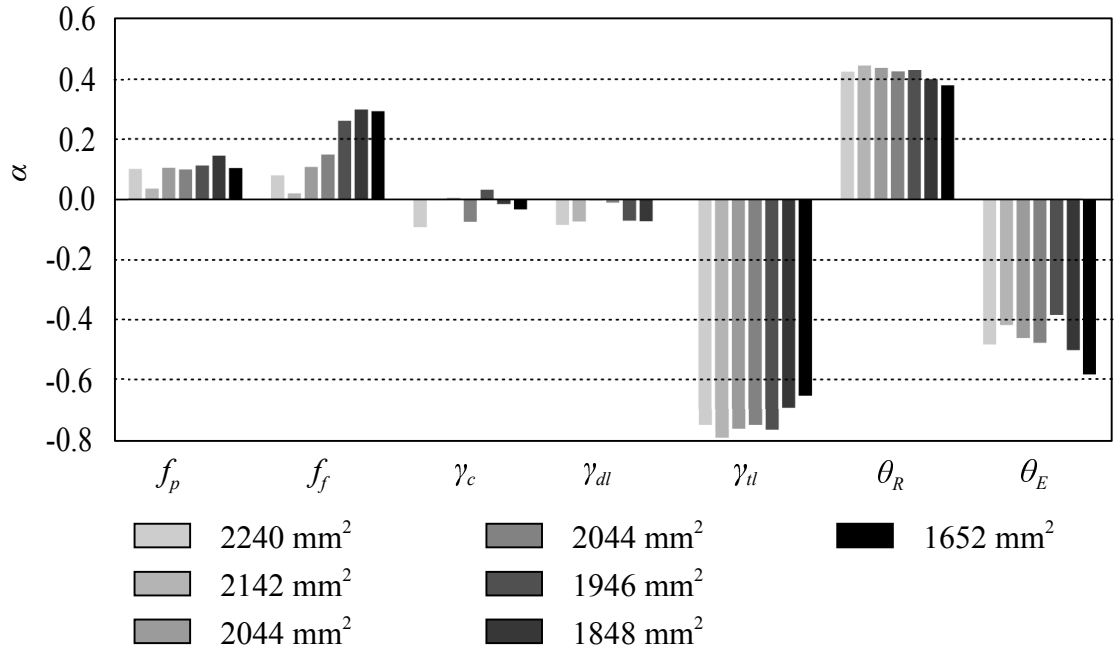

Figure 5.15: Cosines direction at design point as a function of the prestressing area of bridge B13.

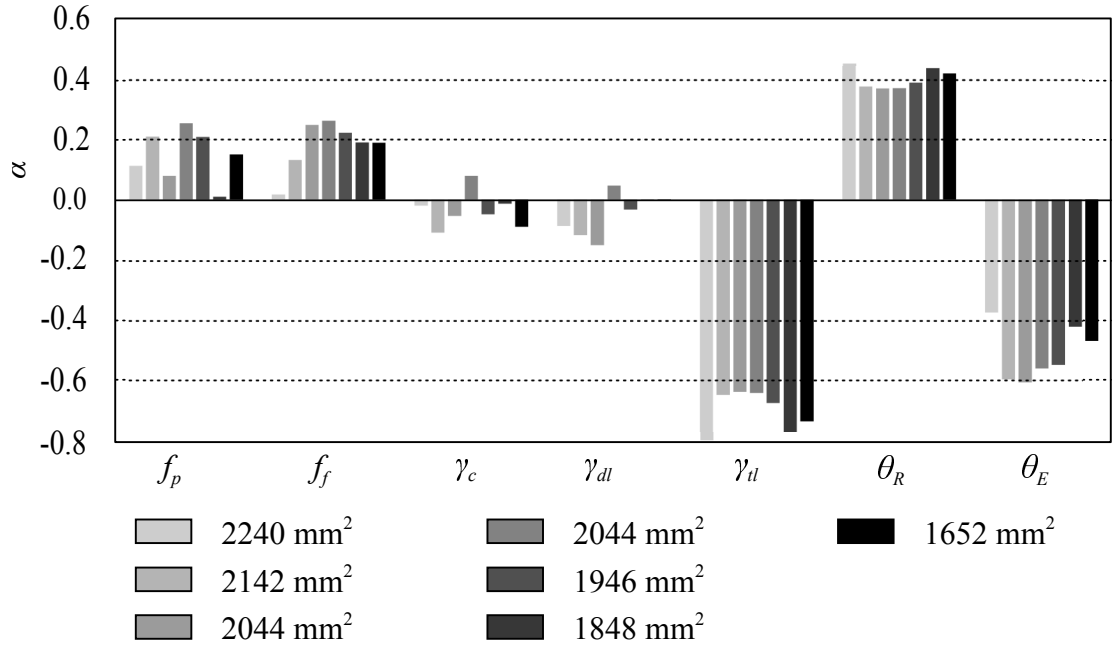

Figure 5.16: Cosines direction at design point as a function of the prestressing area of bridge B16.

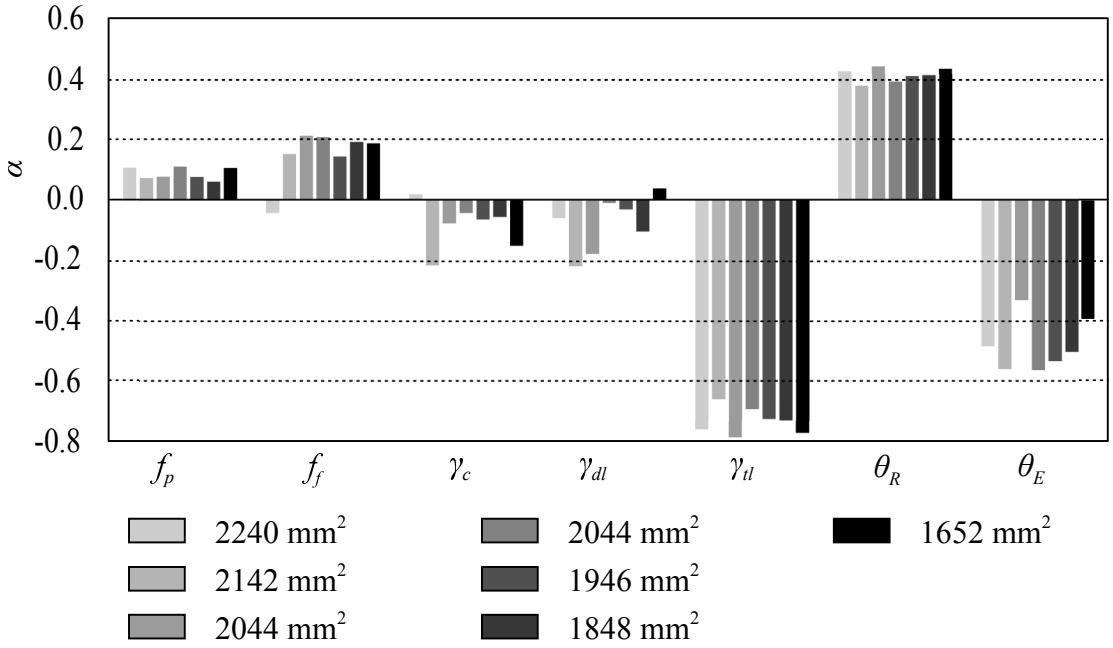

Figure 5.17: Cosines direction at design point as a function of the prestressing area of bridge B19.

it is possible to see that in all analysis this variable is the most significant. The load uncertainties variable, θ_E, is also an important variable since its weight ranges approximately from -0.40 to -0.60. In respect to the other loads, namely concrete self-weight, γ_c, and dead loads, γ_{dl}, both of them present lower sensitivity factors, always less than -0.15 with the exception of some cases shown in Figure 5.17. On the other hand, the resistance parameter showing the highest importance is the resistance uncertainty, θ_R, presenting values around 0.40 for all analysis. The prestressing strength, f_p, shows values nearly 0.10 for the bridges B13 and B19, and in some cases can reach 0.20 for bridge B16. The CFRP strength, f_f, exhibits values up to 0.30, assuming greater importance than the prestressing strength in the majority of the analysis. This may be related with the loss of prestressing area.

In some cases, the cosines sign does not correspond to the expected, i.e., the resistance variables assume positive values and the loads variables assume negative values. This error occurs due to possible deviations in numerical results that are used to build the response surface, particularly in less important variables that do not have a strong impact in reliability results. Nevertheless, this can be easily controlled by increasing the number of support points for the construction of the surface.

5.4.2.3 Calibration analysis

The results of the calibration procedure described in Section 5.3.2.3 are shown herein. Firstly, the design points used for calibration are presented. Then, the partial safety factors computed for all variables and used as a reference to calibrate the model and the CFRP partial safety optimisation results are showed and discussed; and finally, the computed factor is validated.

Design points

Table 5.12 shows the reliability index and design points used for the calibration of CFRP partial safety factors, i.e, the cases for which the CFRP area leads to values closest to the target reliability index. Reliability indices are slightly higher than the target reliability index considered to strengthen the girders – 4.3. This occurs because the design points used for the calibration were determined using numerical models, which computes a higher reliability index when compared with analytical models used to calculate the needed CFRP area. Nevertheless, the deviation is at most 6%, and the reliability index is higher than the target, meaning that the designs are safe and can be used for the calibration of CFRP partial safety factors.

The design values, present in Table 5.12, show that almost all resistance variables, f_p, f_f and θ_R present lower values when compared with variables mean values – 1674.0 MPa, 2686.4 MPa, 1.0. On the other hand, the load variables, γ_c, γ_{dl}, γ_{tl} and θ_E, tend to present higher values when compared with variables mean values – 25.0 kN/m^3, 10.37 kN/m, 0.84, 1.0. These results are just not observed when the cosines sign presents a different direction than expected. Moreover, traffic loads exhibit the higher deviation, showing its importance for the calibration process.

Partial safety factors

Table 5.13 presents the partial safety factors calculated for all variables using numerical models. The values of $f_{pk} = 1632.0$ MPa, $f_{fk} = 2304.2$ MPa, $\gamma_{ck} = 25.0$ kN/m^3, $\gamma_{dlk} = 10.83$ kN/m, were considered for its calculation (Gomes et al., 2013; Jacinto et al., 2012). The partial safety factor of prestressing strength is slightly higher to the one adopted in CEN (2002a) – 1.15 – and close to the self-concrete weight and

Table 5.12: Reliability index and design points used for calibration.

Bridge	β	f_p^* (MPa)	f_f^* (MPa)	γ_c^* (kN/m^3)	γ_{dl}^* (kN/m)	γ_{tl}^*	θ_R^*	θ_E^*
B13	4.36	1651.90	2639.70	25.40	11.23	1.41	0.78	1.29
B13-D1	4.38	1666.10	2676.20	25.01	11.17	1.48	0.77	1.25
B13-D2	4.35	1648.40	2538.90	24.98	10.58	1.42	0.78	1.27
B13-D3	4.41	1649.20	2512.30	25.32	10.64	1.42	0.78	1.28
B13-2D1	4.32	1652.50	2470.90	24.86	10.98	1.42	0.78	1.24
B13-2D2	4.33	1643.70	2398.30	25.06	11.13	1.32	0.80	1.29
B13-2D3	4.34	1651.40	2405.00	25.14	10.32	1.28	0.80	1.34
B16	4.43	1649.30	2679.20	25.09	11.25	1.51	0.77	1.23
B16-D1	4.47	1627.40	2585.10	25.49	11.40	1.30	0.80	1.36
B16-D2	4.57	1656.15	2444.55	25.25	11.58	1.30	0.80	1.38
B16-D3	4.65	1615.30	2420.80	24.64	10.60	1.32	0.79	1.35
B16-2D1	4.44	1627.90	2484.10	25.22	10.99	1.33	0.79	1.33
B16-2D2	4.62	1671.80	2512.40	25.06	10.84	1.49	0.77	1.27
B16-2D3	4.42	1641.00	2524.00	25.40	10.82	1.41	0.78	1.29
B19	4.58	1649.30	2752.30	24.91	11.12	1.48	0.77	1.30
B19-D1	4.45	1657.50	2561.40	25.95	11.87	1.31	0.80	1.34
B19-D2	4.45	1656.50	2493.10	25.34	11.68	1.48	0.77	1.21
B19-D3	4.57	1648.50	2492.10	25.19	10.87	1.38	0.79	1.35
B19-2D1	4.53	1656.40	2567.90	25.28	10.97	1.42	0.78	1.33
B19-2D2	4.53	1660.00	2513.30	25.25	11.33	1.42	0.78	1.31
B19-2D3	4.48	1650.00	2521.00	25.67	10.64	1.47	0.77	1.24

dead loads – 1.35. The presented partial safety factors for CFRP correspond to the reliability indices shown in Table 5.12. Additionally, the partial safety factor of traffic loads refers to the uniform and concentrated loads, and is not affected by its characteristic values, reason why it presents such a high large value.

CFRP partial safety factor optimisation

Figure 5.18 shows the sum of squared errors as a function of the partial safety factor for CFRP, γ_f. The objective deviation reaches a minimum when the partial safety factor is 1.13, being the most appropriate factor for the chosen target reliability index.

The results are consistent with the CFRP partial safety factors computed using

Table 5.13: Partial safety factors.

Bridge	γ_p	γ_f	γ_c	γ_{dl}	γ_Q
B13	1.27	1.12	1.31	1.34	1.82
B13-D1	1.27	1.12	1.25	1.29	1.85
B13-D2	1.27	1.16	1.27	1.24	1.81
B13-D3	1.27	1.17	1.30	1.26	1.81
B13-2D1	1.27	1.19	1.23	1.25	1.76
B13-2D2	1.25	1.21	1.29	1.33	1.70
B13-2D3	1.23	1.19	1.35	1.28	1.72
B16	1.29	1.12	1.24	1.28	1.86
B16-D1	1.26	1.12	1.39	1.43	1.77
B16-D2	1.23	1.18	1.39	1.47	1.80
B16-D3	1.27	1.20	1.33	1.33	1.78
B16-2D1	1.27	1.18	1.34	1.35	1.77
B16-2D2	1.26	1.18	1.27	1.27	1.89
B16-2D3	1.27	1.17	1.28	1.28	1.81
B19	1.28	1.09	1.30	1.34	1.93
B19-D1	1.23	1.13	1.39	1.47	1.75
B19-D2	1.28	1.20	1.22	1.30	1.79
B19-D3	1.26	1.18	1.36	1.35	1.86
B19-2D1	1.26	1.15	1.34	1.34	1.88
B19-2D2	1.26	1.18	1.32	1.37	1.86
B19-2D3	1.28	1.18	1.28	1.22	1.83
maximum	1.29	1.21	1.39	1.47	1.93
minimum	1.23	1.09	1.22	1.22	1.70

the numerical model and presented in Table 5.13. In fact, it is possible to observe that the CFRP optimum factor calculated with analytical models and considering the mandatory partial safety factors for prestressing strength, concrete compressive strength, dead loads and live loads, is within the range of values presented – 1.09 to 1.21.

The values recommended in design guides are also similar to the computed partial safety factor. For instance, for the design of concrete structures using CFRP end anchored laminates, CEB/FIB (2001) recommends the use of a safety factor of 1.20, higher than to the calibration results. On the other hand, CNR (2013) recommends a factor of 1.10, below to the suggested one, and TR-55 (2000) is more conservative, suggesting a factor of 1.54 for this type of strengthening.

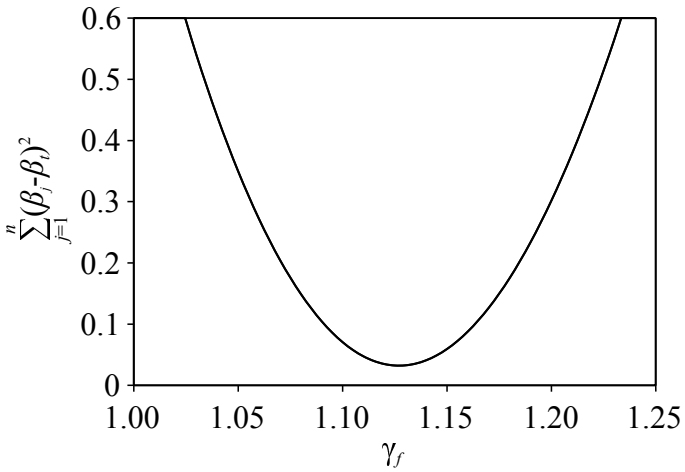

Figure 5.18: Optimum partial safety factor for CFRP, γ_f.

Partial safety factors checking

The computed partial safety factor was validated by comparing the amount of area used for the calibration process (see Table 5.11), with the amount of area computed during a design process for the same girders and considering: i) the computed partial safety factor – 1.13; and ii) the regulatory prestressing strength, concrete compressive strength, dead loads and live loads partial safety factors – 1.15, 1.35, 1.35 and 1.50.

Table 5.14: CFRP area calculated with the recommended γ_f.

Bridge	A_f (mm^2)	Bridge	A_f (mm^2)	Bridge	A_f (mm^2)
B13	472	B16	469	B19	481
B13-D1	532	B16-D1	533	B19-D1	545
B13-D2	591	B16-D2	595	B19-D2	608
B13-D3	649	B16-D3	655	B19-D3	670
B13-2D1	586	B16-2D1	590	B19-2D1	606
B13-2D2	694	B16-2D2	706	B19-2D2	726
B13-2D3	803	B16-2D3	815	B19-2D3	839

Results show that the area used for calibration is up to 15% lower than the area used for design. This confirms that the adopted factor falls within the safety region, since a larger CFRP area is needed to perform the design than for the calibration.

5.5 Conclusions

In this chapter a process to compute partial safety factors of CFRP laminates considering degraded structures was presented. The method combined analytical and numerical models to reduce computational costs and to consider the non-linear structural behaviour existing in FRP strengthened PC girders when the ULS is reached.

Several cases of study consisting in simple supported PC girders representative of the typical Portuguese construction used for bridges during the last 40 years were considered. The Portuguese code RSA (1983) was used for the design, whereas the European code CEN (2002b) was considered for the strengthening process. The analysis allowed to conclude that CEN (2002b) is more conservative than RSA (1983) and that the safety margin of Portuguese bridges are lower than the required in CEN (2002a). This is related with the fact that the RSA (1983) was developed in the 1960s in a setting where traffic needs were significantly different than the current requirements, whereas CEN (2002b) was developed taking into account traffic measures from the centre of Europe, where traffic is more intense than border countries.

Results show that the flexurally capacity of the PC girders can be upgraded up to 74% and 25% for the degraded and non-degraded girders, respectively, allowing to restore the capacity of the girders according to CEN (2002b) requirements.

The sensitivity analysis allows to verify that traffic loads and models uncertainties are extremely important for the calibration process, assuming high values when compared with dead loads, concrete self-weight or prestressing strength. Thus, the CoV for traffic loads should be chosen carefully. Additionally, prestressing strength and CFRP strength variables are fundamental to have into account since failure occurs by CFRP rupture after prestressing yield.

The computed partial safety factor for CFRP – 1.13 – is close with what recommended in CNR (2013) – 1.10 – and is lower than what recommended in CEB/FIB (2001) – 1.20. It is important to highlight that these factors are in accordance with what computed using validated numerical models, that consider the non-linear structural behaviour of CFRP strengthened girders.

These results allow to conclude that the use of the RSM combined with FORM to consider non-linear analysis to model PC structural behaviour, is a good approach to adopt for reliability analysis and to compute CFRP partial safety factors.

Chapter 6

Time-dependent reliability analysis considering steel corrosion and CFRP strength degradation

6.1 Introduction

In the reliability analysis described in Chapter 5, several predefined levels of structural degradation were assumed. This chapter presents a procedure for reliability studies considering the structural element strength reduction as a function of time, that can help the decision making process during the maintenance practice of existing concrete heritage (Melchers, 1999).

Time-dependent flexural reliability analysis of RC beams has been widely studied in the last decades by several researchers that consider steel reinforcement general and pitting corrosion as time-dependent random variables – e.g., Stewart and Rosowsky (1998a); Val and Melchers (1997); Val et al. (1998); Vu and Stewart (2000) – concluding that reliability strongly decreases due to corrosion, and that the pitting corrosion, the distance from the coast line and concrete cover are important parameters for reliability. However, these studies are limited to consider that corrosion only occurs at the mid-span section, neglecting the spacial spread of pitting corro-

sion that exists over the reinforcement length. Stewart (2004) proposed to study the flexural time-dependent reliability taking into account the spatial variability of pitting corrosion, by dividing the structural element – beam – into several segments. For each segment, different levels of pitting corrosion were randomly included to simulate the non-homogeneous corrosion phenomenon along the beam, i.e., spatial variability of corrosion. Reliability was computed considering a series system of statistically independent segments. This procedure has been adopted by several researchers, such as Darmawan and Stewart (2007a); Stewart and Al-Harthy (2008); Stewart and Mullard (2007); Stewart and Suo (2009), Stewart (2009, 2012); Val (2007), showing that probabilities of failure considering series reliability are higher when compared with the ones based only on the most unfavourable situation – the failure caused by the reinforcement rupture at mid-span – see Figure 6.1.

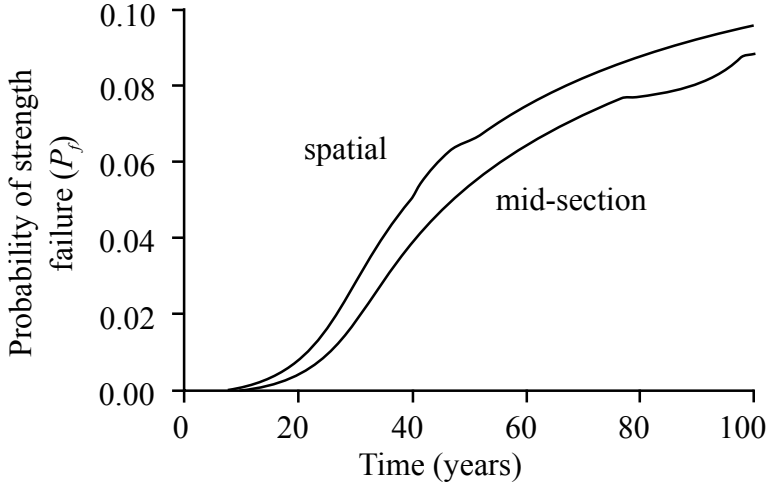

Figure 6.1: Probability of failure for spatial and mid-section corrosion (Darmawan and Stewart, 2007a).

Besides the time-dependent reliability studies for the non-strengthened beams, little efforts have been made to extend the same to FRP strengthened RC beams. So far, the only study regarding to time-variant flexural reliability of RC beams with CFRP as EBR was carried out by Bigaud and Ali (2014). The time-dependent reliability was calculated first for the non-strengthened scenario and then for the strengthened and degraded beams. Nevertheless, the spatial corrosion was not considered.

The aforementioned studies were mainly devoted to highways girders or bridges designed with the ASHTO LRFD (2002). Moreover, only one study considered a pos-

sible rehabilitation/repair scenario during the time-dependent analysis, whereas the remaining authors just regarded the structural degradation over time. Despite the huge progress made in structural reliability of RC beams, some limitations remain:

- only one study – see Bigaud and Ali (2014) – considered a rehabilitation scenario, that includes the use of CFRP;
- reliability is computed based on steel reduction area at mid-span or on the series system reliability, neglecting correlation between segments;
- the uncertainties for load and resistance models were not taken into account in the majority of studies. However, as seen in Chapter 5, these parameters are important and cannot be neglected;
- the corrosion model error was not considered in several studies, e.g., Val and Melchers (1997) or Stewart and Al-Harthy (2008);
- the corrosion initiation time is neglected in Val and Melchers (1997) and Val et al. (1998);

This chapter presents a time-dependent flexural reliability analysis of a PC girder, considering: i) corrosion time and spatial variability, ii) a rehabilitation scenario using CFRP laminates; and iii) the use of the Ditlevsen (1979) bounds to enhance series reliability of PC girders. The corrosion of steel reinforcement is briefly described in Section 6.2. Then, Section 6.3 introduces all stages of the adopted procedure. Finally, results and conclusions are shown in Sections 6.4 and 6.5, respectively.

6.2 Corrosion of RC structures

One of the major causes for RC structures degradation is corrosion of steel reinforcement. Although this process presents a slow progression, when not detected it can lead to structural collapse, as in the case of a pedestrian bride at Concorde, United States of America – see Figure 6.2 – that failed due to prestressing strands pitting corrosion (Faber, 2005). As a consequence, more than one hundred people got injured and millions of dollars had to be paid in compensations.

Figure 6.2: Concorde bridge collapse due to pitting corrosion (Faber, 2005).

In the following a brief introduction to the mechanics of corrosion, its initiation and propagation time and its effect on RC structures is presented.

6.2.1 Corrosion mechanism of reinforcing steel in concrete

The corrosion of steel in concrete – see Figure 6.3 – is a chemical process associated with the transfer of electrons from the anodes to the cathodes. It is an electrochemical process divided into two reactions: i) the anodic reaction, that consists in the oxidation of iron (Fe) to form ferrous ions (Fe^{2+}) (ACI Committee 222, 2001):

$$2Fe \rightarrow 2Fe^{2+} + 4e^{-} \tag{6.1}$$

and ii) the cathodic reaction that consists in the formation of hydroxyl ions (OH^{-}) based on a reduction reaction from the combination of water (H_2O), oxygen (O_2) and the released electrons from Equation (6.1):

$$2H_2O + O_2 + 4e^{-} \rightarrow 4OH^{-} \tag{6.2}$$

The anodic product reacts with the ions formed cathodically to produce the fer-

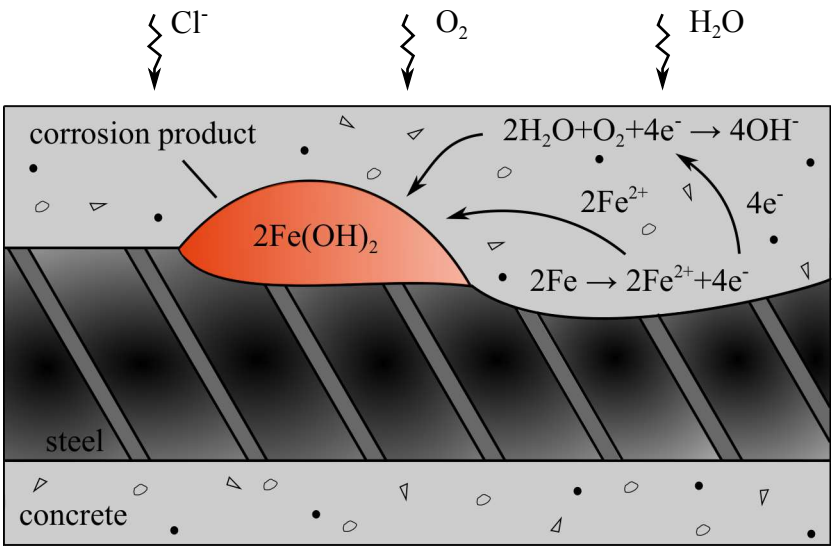

Figure 6.3: Corrosion mechanism of RC (adapted from PCA (2013)).

rous hydroxide:

$$2Fe^{2+} + 4OH^{-} \rightarrow 2Fe(OH)_2 \tag{6.3}$$

When the product from the previous equation reacts with oxygen, forms the hydrated ferric oxide ($Fe_2O_3H_2O$) – the red-brown rust – and water:

$$4Fe(OH)_2 + O_2 \rightarrow Fe_2O_3H_2O + 2H_2O \tag{6.4}$$

These reactions are dependent on the products present in concrete and need oxygen and water to occur. Normally, concrete exhibits an alkaline environment that prevents reinforcement corrosion, given a thin protection of ferric oxide that surrounds steel. In some cases corrosion in concrete may occur due to the pH reduction given the carbon dioxide (CO_2) penetration (ACI Committee 440, 1996). This phenomenon is known as carbonation and consists in the reaction of the atmospheric carbon dioxide with the calcium hydroxides ($Ca(OH)_2$) present in cement past (PCA, 2013):

$$CO_2 + Ca(OH)_2 \rightarrow CaCO_3 + H_2O \tag{6.5}$$

From this reaction results calcium carbonate, water and a pH reduction as low as

8.5 (PCA, 2013). Nevertheless, the major cause for RC corrosion is the penetration of chloride ions. Concrete structures are frequently exposed to chlorides (e.g., deicing salts, seawater or concrete admixtures) and these can react with the ferrous ions present in concrete to form ferrous chloride (ACI Committee 222, 2001; PCA, 2013):

$$Fe^{2+} + 2Cl^{-} \rightarrow FeCl_2 \tag{6.6}$$

When water is available, ferrous hydroxide is produced:

$$FeCl_2 + 2H_2O \rightarrow Fe(OH)_2 + 2HCl \tag{6.7}$$

In this thesis, the corrosion caused by chloride ions was taken into account since this is the most common cause of corrosion documented for RC structures (ACI Committee 222, 2001; PCA, 2013). The adopted models are described in the following.

6.2.2 Corrosion initiation and propagation

The deterioration process caused by corrosion in RC structures can be divided according to the structural lifetime as shown in Figure 6.4.

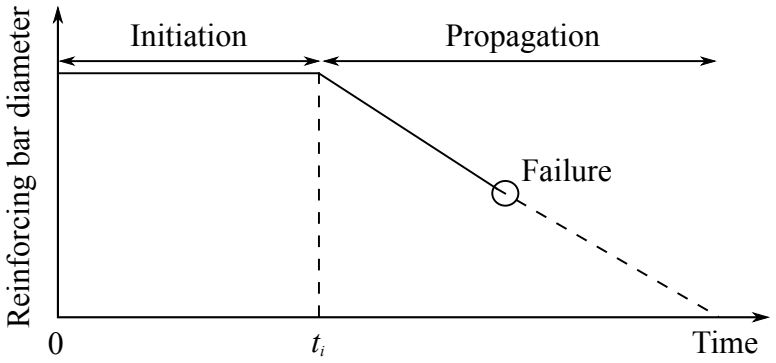

Figure 6.4: Lifetime of corroded RC structures (Stewart and Rosowsky, 1998a).

Initiation time

During the initiation period, corrosion starts at a very slow rate and no deterioration

signs are expected. Environmental agents, such as water, oxygen, carbon dioxide and chlorides start to penetrate the concrete layer.

The initiation time, t_i, is the time necessary for the chloride ions concentration at the contact surface of steel to reach a threshold value, C_{th}, as shown in Figure 6.5. The diffusion process of chloride ions can be computed according to Fick's second law (Stewart and Rosowsky, 1998a):

$$\frac{\partial C(x,t)}{\partial t} = D_{cl}\frac{\partial^2 C(x,t)}{\partial x^2} \tag{6.8}$$

where $C(x,t)$ is the chloride ion concentration at time t and at distance, x, from the surface and D_{cl} is the chloride diffusion coefficient.

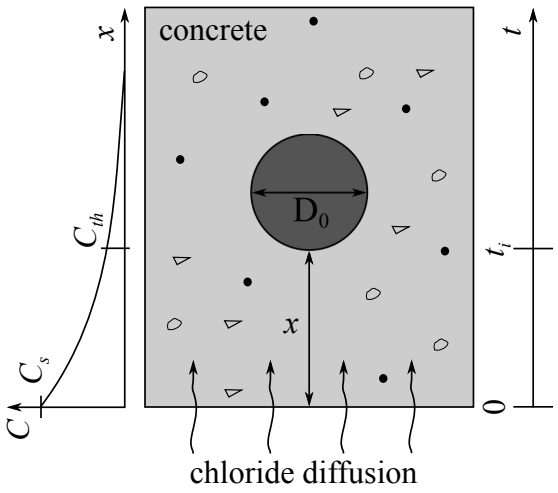

Figure 6.5: Chloride diffusion process of corrosion initiation.

The chloride concentration is considered null at time zero and it can be computed as:

$$C(x,t) = C_s\left[1 - erf\left(\frac{x}{2\sqrt{D_{cl}t}}\right)\right] \tag{6.9}$$

where C is the chloride concentration at time t and depth x, C_s is the chloride concentration on concrete surface, *erf* is the error function and D_{cl} is the chloride diffusion coefficient. The last coefficient is strongly affected by time of exposure, temperature and relative humidity (Val and Trapper, 2008), whereas the chloride concentration on concrete surface can be considered according to the distance from

the coast:

$$C_s(d) = \begin{cases} 2.95 & \text{if} \quad d \leq 0.1 \text{ km} \\ 1.15 - 1.81\log_{10}(d) & \text{if} \quad 0.1 < d < 2.84 \text{ km} \\ 0.35 & \text{if } d > 2.84 \text{ km} \end{cases} \tag{6.10}$$

where d is the distance in km.

Propagation period

The propagation period occurs after the steel protection starts to deteriorate and gives place to corrosion at a much higher rate. This period ends when structure fails or is repaired.

Corrosion is simulated based on the steel diameter bar reduction as a function of corrosion rate. This parameter is not straightforward and depends on several factors, such as the available water and oxygen surrounding the reinforcement, the relative humidity, the temperature or the water-cement ration. Vu and Stewart (2000) proposed an empirical time-dependent model to compute corrosion rate:

$$i_{corr}(t) = i_{corr}(1)0.85t^{-0.29} \tag{6.11}$$

where t is time in years and $i_{corr}(1)$ is the corrosion current at the first year after the corrosion initiation time, given by:

$$i_{corr}(1) = \frac{37.8(1 + wc)^{-1.64}}{c} \tag{6.12}$$

in which wc is the water-cement ration and c is the concrete cover. These equations were developed based on experiments considering a relative humidity of 75% and a temperature of 20°C.

During this stage, corrosion propagation may occur uniformly along the bar or concentrate at specific locations. When corrosion extends uniformly to a large area, it is denoted generalised corrosion – usually caused by carbonation. On the other hand, when it is more pronounced on a specific localisation, even when generalised corrosion occurs, it is known as pitting corrosion. This type of corrosion is more

likely to occur due to chloride attack. Moreover, pitting corrosion is common in prestressing steel and is spatially and temporarily variable (Darmawan and Stewart, 2007b).

Several factors can influence corrosion parameters, such as the water-cement ratio, the cement composition, the aggregate size, construction practices, the concrete cover, environmental conditions, admixtures, temperature, pH change due to carbonation, among others (ACI Committee 222, 2001; Stewart and Rosowsky, 1998a). Since these parameters are hard to predict accurately, either in time or space, a probabilistic approach, such as the one used herein, can allow the explicit consideration of uncertainty.

6.2.3 Effect of corrosion in RC elements in bending

In the last decades, strong efforts have been made to better understand the effect of corrosion on RC structures, including: i) experimental investigations (Al-Sulaimani et al., 1990; Almusallam et al., 1996; Cabrera, 1996; Khan et al., 2012; Menoufy and Soudki, 2004; Rinaldi et al., 2010; Rodriguez et al., 1997; Torres-Acosta et al., 2007), ii) local inspections (Bruce et al., 2008); and iii) data collection from instrumented structures (Anderson and Vesterinen, 2006). From these results several observations have been reported, such as the reduction of steel reinforcement cross area, concrete cracking and bond loss between steel and concrete. The reduction of steel reinforcement area is one of the most important since it drastically decreases the resistance of structural elements. In fact, this can be even more concerning in the case of prestressing strands, in which the local reduction of the cross section may lead to premature steel failure (PCA, 2013). Models have been developed to try estimating the reduction of cross section of steel bars, e.g., Val and Melchers (1997), Vu and Stewart (2000), Darmawan and Stewart (2007a) or Darmawan and Stewart (2007b).

Concrete cracking is also a common effect of corrosion. It occurs because the products resulting from corrosion have a greater specific volume when compared with the reinforcement lost, as shown in Figure 6.6. For instance, the hydrated ferric oxide ($Fe(OH)_3 3H_2O$) has a volume seven times larger than iron (Fe). Thus, concrete

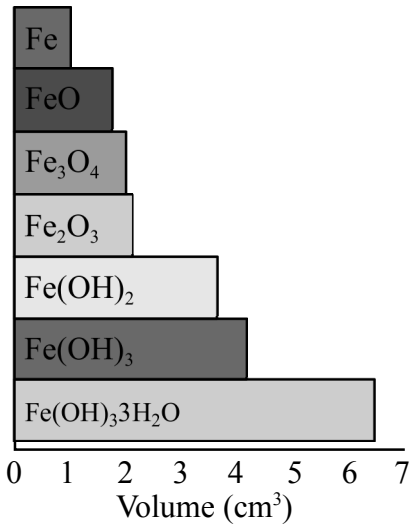

Figure 6.6: Iron and its products relative volume (ACI Committee 222, 2001).

cracks under internal stresses. Additionally, when cracks reach the surface of concrete, a new path is created for the ingression of several agents that can accelerate corrosion. In scenarios of extensive cracking, the spalling of concrete may also occur, leaving reinforcement exposed to environmental agents (ACI Committee 222, 2001).

The bond between concrete and reinforcement is lost when the iron oxides from corrosion starts to form. Usually, when corrosion initiates and cracking has not yet occurred, the bond strength may increase (CEB/FIB, 2000). Then, it quickly decreases as a result of concrete cracking. Several experimental studies have evaluated the loss in flexural capacity resulting from corrosion, see Almusallam et al. (1996); Menoufy and Soudki (2004); Rinaldi et al. (2010). Figure 6.7 shows a representative example of the flexural strength reduction as a function of corrosion for PC beams with rectangular cross section (Rinaldi et al., 2010). No bond loss at the extremities of the strands was considered and the artificial pitting corrosion was generated by an electrolytic process. The load carrying capacity reduces with corrosion increasing, with both failure mode and structural response changing from concrete crushing to strand failure, and ductile to brittle, respectively. It was concluded that the behaviour evaluation of prestressed corroding elements is extremely complex, since corrosion is not uniform and generates localised strains and stresses that can enhance a premature failure.

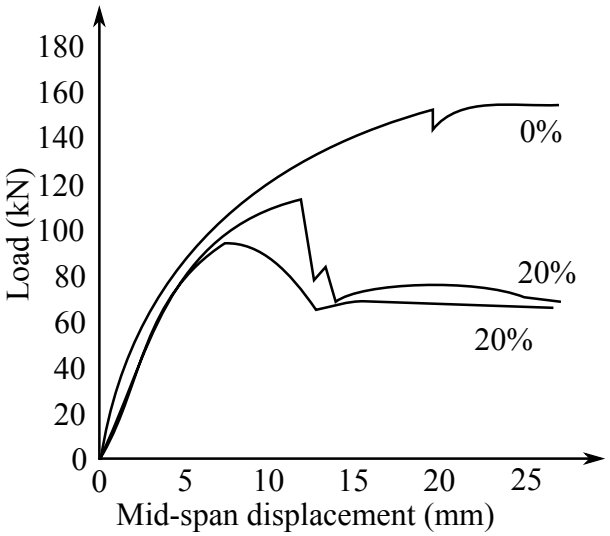

Figure 6.7: Load vs. mid-span curves for PC girders with 0% and 20% of corroded steel reinforcement area (adapted from Rinaldi et al. (2010)).

Menoufy and Soudki (2004) studied the capability of FRP to restore the flexural capacity of pitting corrosion damaged 'T' shaped girders. Results show that CFRP succeeded in restoring the capacity of corroding girders. However, the reduction in ductility is not restored.

6.3 Procedure overview

The procedure developed to compute the time-dependent reliability is shown in Figure 6.8. The first step consists in the definition of the scope of the study. The type of structure, including material, geometry, failure mode and support conditions are set, including the geographical and ageing context. In this study, a CFRP strengthened PC girder used for bridges in Portugal was considered.

The second step is related with the development of design cases that can represent the study scope. The girders design was made using the Portuguese code RSA (1983). Further details are described in Section 6.3.1.

The next step is the definition of the degradation scenario. RC structures can often involve several sources of degradation, such as chloride contamination, carbonation

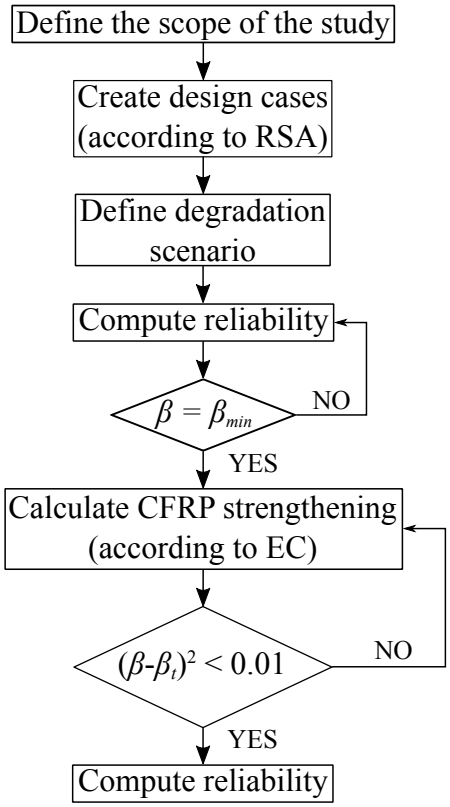

Figure 6.8: Time-dependent reliability procedure.

or fatigue. Steel degradation due to corrosion and FRP degradation were herein considered. More details are described in Section 6.3.2.1.

The fourth step consists in the time-dependent reliability computation. From this step forward, the quantified traffic loads are stipulated according to the European code CEN (2002b), because this code is going to replace RSA (1983). Then, when the minimum reliability index, β_{min}, is reached – i.e., the minimum acceptable level of structural safety measured from the reliability index – CFRP laminates are included in the design. The cross section area of CFRP is determined using FORM, until the target reliability index, β_t, is achieved.

Finally, in the last step, the time-dependent reliability analysis for the strengthened structure is computed. The strength limit state, the statistical variables and the analysis procedure are described in Sections 6.3.2.2, 6.3.2.3 and 6.3.2.4, respectively.

6.3.1 Range of Calibration

The calibration range is constrained to PC girders typically adopted in Portuguese highways. The analysis procedure was applied to a simply supported girder of a bridge with two traffic lanes and two side-walks – see Figure 6.9.

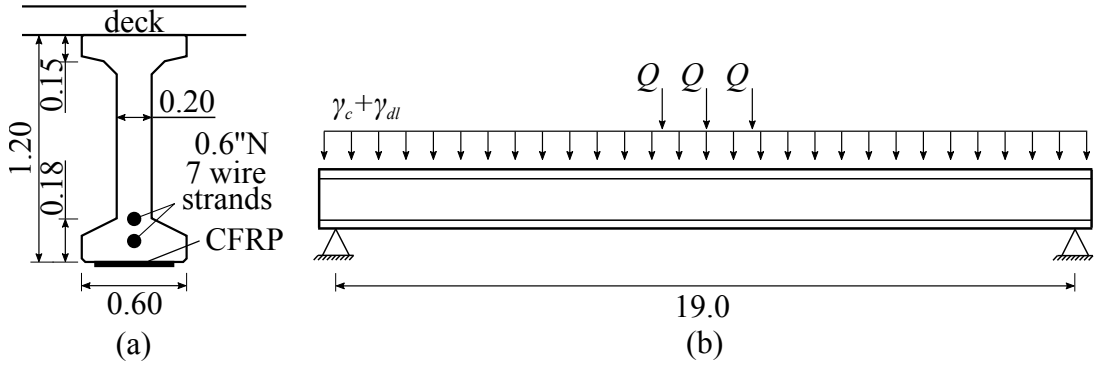

Figure 6.9: Case study: (a) transversal section; and (b) longitudinal section and loading (m).

In order to represent the historical context in Portugal, the girder was designed using the Portuguese code RSA (1983). A scenario of intense traffic was considered adopting a live load, Q, of 200 kN. Additionally, for dead loads, γ_{dl}, and the loads due to concrete self-weight, γ_c, the following values were adopted respectively: 10.37 kN/m and 25 kN/m^3.

The cross section of the girder was designed using the code REBAP (1985) and considering a concrete class of C35/45 and a passive and active steel grades of S500 and Y1860S, receptively. Moreover, strengthening was achieved using CFRP 'CFK 150/2000' laminates. For further details about the design see Section 5.3.1.

6.3.2 Time-dependent analysis

Time-dependent reliability analysis were performed to compute the reliability index, β, and probability of failure, P_f, using FORM (Melchers, 2001) together with RSM (Bucher, 2009).

In the following, a description of the analysis is made, including the adopted degra-

dation models, limit state functions, random variables and implemented procedure.

6.3.2.1 Time-dependent degradation

As stated previously, one of the biggest concerns for prestressing steel structures is related with the corrosion phenomenon that with time leads to structural strength and serviceability reduction (ACI Committee 222, 2001). In the case of FRP strengthened structures, the composite degradation is also important. In the following sections, steel reinforcement and FRP degradation models are described.

Prestressing corrosion

Pitting corrosion is common in prestressing steel due to chloride induced contamination; it can vary in time and space (Darmawan and Stewart, 2007b).

Pitting corrosion was considered according to the model proposed by Val and Melchers (1997). It is time-dependent and assumes the pits to have hemispherical forms, as illustrated in Figure 6.10. Thus, the pit radius, p, can be estimated according to:

$$p(t) = 0.0116 \times (t - t_i) \times i_c \times R \tag{6.13}$$

where t is time, t_i is the time when corrosion starts, i_c is the corrosion rate quantified as a current density and R is the ratio between the maximum pit depth, P_{max}, and the average pit depth, P_{av}.

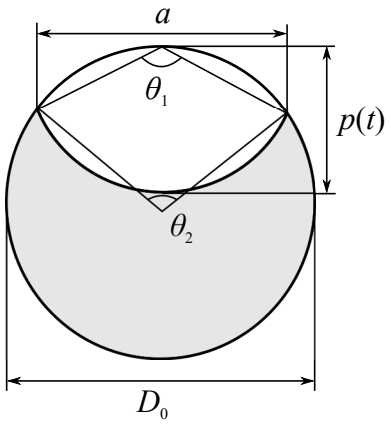

Figure 6.10: Pit corrosion model (Val and Melchers, 1997).

The area of the pit, A_{pit}, can be quantified as:

$$A_{pit}(t) = \begin{cases} \frac{\pi D_0^2}{4} - A_1 - A_2 & \text{if} \quad p(t) \leq \frac{\sqrt{2}}{2} D_0 \\ A_1 - A_2 & \text{if} \quad \frac{\sqrt{2}}{2} D_0 < p(t) \leq D_0 \\ 0 & \text{if} \quad p(t) > D_0 \end{cases} \tag{6.14}$$

with,

$$A_1 = 0.5 \left[\theta_1 \left(\frac{D_0}{2} \right)^2 - a \left| \left(\frac{D_0}{2} \right) - \left(\frac{p(t)^2}{D_0} \right) \right| \right] \tag{6.15}$$

$$A_2 = 0.5 \left[\theta_2 p(t)^2 - a \frac{p(t)^2}{D_0} \right] \tag{6.16}$$

$$a = 2p(t) \sqrt{1 - \left(\frac{p(t)}{D_0} \right)^2} \tag{6.17}$$

$$\theta_1 = 2 \arcsin \left(\frac{2a}{D_0} \right) \tag{6.18}$$

$$\theta_2 = 2 \arcsin \left(\frac{a}{p(t)} \right) \tag{6.19}$$

The spatial variability of corrosion was performed with the method proposed by Stewart (2004). This method assumes that prestressing strands are prone to pitting corrosion over length by dividing reinforcement into several segments – see Figure 6.11 – and by considering different pit depths randomly generated for each segment. Then, the resistance capacity of the girder is computed considering that the tensile capacity of each segment is calculated having into account the prestressing area reduction from the Equation (6.14), in which the correlation between the maximum and average pit depth is randomly generated, forcing the diameter of the pits to vary for each segment along reinforcement.

The length of the segments should model the distance at which pitting corrosion influences the structural safety. This depends on several factors, such as: i) the corroded reinforcement capacity to redistribute stresses to the continuous reinforcement, ii) the reinforcement mechanical behaviour, iii) the reinforcement development length; and iv) the reinforcement geometry and spacing (Stewart, 2009); for what

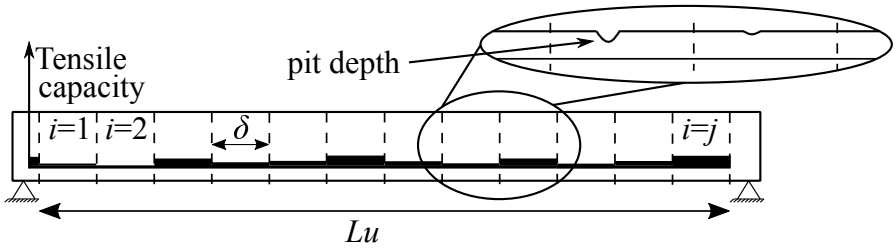

Figure 6.11: Spatial tensile capacity of the girder.

typically varying between 0.1 m and 1.0 m (Stewart, 2004, 2009; Stewart and Al-Harthy, 2008; Val, 2007). In this thesis, the segment length was assumed to be 0.4 m, which is within the range adopted by other authors. Furthermore, this value also leads to an initial reliability index, i.e., when corrosion is not started yet, compatible with the one computed when the series system is not taken into account.

All segments were considered to be statistically independent and random pit depths, R, were generated using a Gumbel distribution based on experimental results from concrete specimens subjected to accelerated corrosion tests made by Stewart and Al-Harthy (2008). The chloride-concrete environment was simulated using an impressed electric current and the maximum pit depths were measured for each 100 mm length of reinforcement. The adopted model is:

$$R \sim \mathrm{G}(\mu, \alpha); \quad \mu = 5.56; \quad \alpha = 1.16 \tag{6.20}$$

FRP degradation

In the last years, experimental studies have been performed to assess the degradation of FRP, such as Abanilla et al. (2006a,b); David and Neuner (2001); Karbhari et al. (2003); Liao (1999); Rivera and Karbhari (2002). This issue is still new in the reliability framework, precluding the existence of probabilistic models for the degradation of FRP.

In this thesis, FRP degradation was included as a deterministic parameter and by considering: i) no degradation; and ii) degradation regarding the Arrhenius rate equation developed by Karbhari and Abanilla (2007) – the same model used by

Atadero and Karbhari (2008) and Ali et al. (2012) – according to the following:

$$\%f_{f_R} = -3.366\ln(t) + 106.07 \tag{6.21}$$

where $\%f_{f_R}$ is the percentage of FRP strength retention and t is time in days.

6.3.2.2 Strength limit state

Reliability was computed considering the beam as a series system, assuming that the safety of the girder depends on several segments. The limit state function, G, is determined for all segments as a function of time, t:

$$G_j(t) = \gamma_{mtl_j}(t) - \gamma_{tl_j} \tag{6.22}$$

where j is the segment, γ_{mtl} is the maximum traffic load scale factor supported by the girder in function of time and γ_{tl} is the traffic load scale factor from codes. The first term is time-dependent and was computed from the maximum capacity predicted with the analytical model. Thus, the limit state function can be expressed as:

$$G_j(t) = \gamma_{mtl_j}(\theta_E; v_1(t); v_2(t); v_3(t); ...v_n(t)) \times \theta_R - \gamma_{tl_j} \tag{6.23}$$

in which θ_E is the load model uncertainty, θ_R is the resistance model uncertainty, v are the statistical variables and n is the maximum number of statistical variables described in next section.

Ditlevsen (1979) bounds were used to compute the probability of failure of a series system, taking into account the correlation between segments or failure modes according to Equation (2.75). For instance, for the system in Figure 6.12, segments correlation can be calculated using the coefficient from Equation (2.73), as:

$$\begin{cases} \rho_{sys_{12}} = \alpha^*_{11}\alpha^*_{21} + \alpha^*_{12}\alpha^*_{22} + \alpha^*_{13}\alpha^*_{23} + \alpha^*_{14}\alpha^*_{24} \\ \rho_{sys_{13}} = \alpha^*_{11}\alpha^*_{31} + \alpha^*_{12}\alpha^*_{32} + \alpha^*_{13}\alpha^*_{33} + \alpha^*_{14}\alpha^*_{34} \\ \rho_{sys_{14}} = \alpha^*_{11}\alpha^*_{41} + \alpha^*_{12}\alpha^*_{42} + \alpha^*_{13}\alpha^*_{43} + \alpha^*_{14}\alpha^*_{44} \\ \rho_{sys_{23}} = \alpha^*_{21}\alpha^*_{31} + \alpha^*_{22}\alpha^*_{32} + \alpha^*_{23}\alpha^*_{33} + \alpha^*_{24}\alpha^*_{34} \\ \rho_{sys_{24}} = \alpha^*_{21}\alpha^*_{41} + \alpha^*_{22}\alpha^*_{42} + \alpha^*_{23}\alpha^*_{43} + \alpha^*_{24}\alpha^*_{44} \\ \rho_{sys_{34}} = \alpha^*_{31}\alpha^*_{41} + \alpha^*_{32}\alpha^*_{42} + \alpha^*_{33}\alpha^*_{43} + \alpha^*_{34}\alpha^*_{44} \end{cases} \tag{6.24}$$

The joint probability of different segments are computed according to Equation (2.72) and the lower and upper probabilities of failure (Equation (2.71)) can be computed according to:

$$P_{f_{lower}} = p_{f_1} + \max\left[p_{f_2} - p_{f_2} \cap p_{f_1}; 0\right] + \max\left[p_{f_3} - p_{f_3} \cap p_{f_2} - p_{f_3} \cap p_{f_1}; 0\right] + \max\left[p_{f_4} - p_{f_4} \cap p_{f_3} - p_{f_4} \cap p_{f_2} - p_{f_4} \cap p_{f_1}; 0\right] \tag{6.25}$$

and

$$P_{f_{upper}} = p_{f_1} + p_{f_2} + p_{f_3} + p_{f_4} + p_{f_2} \cap p_{f_1} - \max\left[p_{f_3} \cap p_{f_2}; p_{f_3} \cap p_{f_1}\right] - \max\left[p_{f_4} \cap p_{f_3}; p_{f_4} \cap p_{f_2}; p_{f_4} \cap p_{f_1}\right] \tag{6.26}$$

The average between the lower and upper probabilities of failure provides a good estimate of the probability of failure of the system.

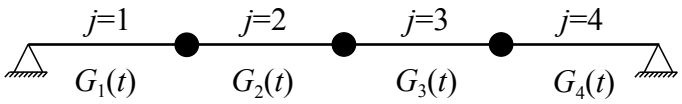

Figure 6.12: Series model with four segments.

For comparative purposes, probabilities of failure were also calculated using the lower and upper bounds for series system according to Equations (2.65) and (2.67).

6.3.2.3 Random variables

As mentioned in Section 5.3.2.1, the number of random variables should be the lowest possible to reduce computational cost. Herein, the variables were divided in three categories: i) resistance, ii) loads; and iii) corrosion. The considered resistance variables were the prestressing strength, f_p, the CFRP strength, f_f, and the resistance model uncertainty, θ_R. The load variables were the traffic load scale factor (see Section 5.3.2.1 for the model description), γ_{tl}, the dead loads, γ_{dl}, the concrete self-weight, γ_c, and the loads model uncertainty, θ_E. Additionally, the random variables associated with corrosion were: the surface chloride concentration, C_s, the threshold chloride concentration, C_{th}, the chloride diffusion coefficient, D_{cl}, the concrete cover, c, the corrosion rate, i_c and the corrosion model error, γ_{ic}. Variables are summarised in Table 6.1.

Several values for the corrosion rate varying from 0.1 to 10 µA/cm^2, have been adopted by authors, e.g., Darmawan and Stewart (2007a,b); Stewart (2004); Vu and Stewart (2000). For most of the analysis the current density is taken as 1 µA/cm^2 (Stewart, 2004). Thus, in this thesis a log-normal distribution with a mean of 1 µA/cm^2 and a CoV of 0.2 was assumed according to the adopted by Val et al. (1998) to analyse the the reliability of highway bridges.

6.3.2.4 Analysis procedure

The time-dependent reliability analysis procedure is illustrated in Figure 6.13. The first step consists in defining the fundamental basis of the time-dependent reliability analysis, namely: the limit state function, the analytical models and the relevant variables for the case study.

The remaining analysis procedure is divided in three main cycles: i) time-dependent reliability analysis of non-strengthened girders, ii) CFRP strengthening area calculation; and iii) time-dependent reliability analysis of the CFRP strengthened girders.

Time-dependent reliability analysis of non-strengthened girders

This step consists in computing the reliability index and probability of failure for the non-strengthened girder considering the corrosion over time. At this stage, the prestressing strength, f_p, the traffic loads, γ_{tl}, the dead loads, γ_{dl}, the concrete self-weight, γ_c, and the resistance and load models uncertainties, θ_R and θ_E, were included. Moreover, the prestressing corrosion is regarded through the strand area reduction as function of time and the spatial randomly generated pit depth over the beam length.

Prior to the first cycle of calculation, the design points, reliability index and time variables are initialised. Then, for each increment of time, t, the reliability index and probability of failure are computed: firstly, the support points around the design point are calculated; then, the maximum traffic load scale factor is obtained for each point using the analytical model – described in Section 4.3 – to define the response surface. The RSM is used with the FORM to compute the design points, d_{n+1},

Table 6.1: Statistical properties of random variables used in time-dependent reliability analysis.

Variable	Units	Mean	Standard deviation	Distribution type	References
Prestressing strength, f_p	MPa	1674.0	50.0	Normal	Jacinto et al. (2012)
CFRP strength, f_f	MPa	2686.4	207.77	Weibull	Gomes et al. (2013)
Resistance model uncertainties, θ_R	-	1.0	0.10	Log-normal	JCSS (2001)
Traffic loads, γ_{tl}	-	0.84	0.084	Gumbel	Wisniéwski (2007)
Dead loads, γ_{dl}	kN/m	10.37	1.04	Normal	Vejdirektoratet (2004)
Concrete self-weight, γ_c	kN/m^3	25.0	1.0	Normal	JCSS (2001)
Load model uncertainties, θ_E	-	1.0	0.10	Log-normal	JCSS (2001)
Surface chloride concentration, C_s	kg/m^3	0.35	0.175	Normal	Bastidas-Arteaga et al. (2009)
Threshold chloride concentration, C_{th}	kg/m^3	1.20	0.228	Normal	Bastidas-Arteaga et al. (2009)
Chloride diffusion coefficient, D_{cl}	cm^2/s	2.0×10^{-8}	4.0×10^{-9}	Normal	Bastidas-Arteaga et al. (2009)
Concrete cover, c	cm	5.0	0.75	Log-normal	Bigaud and Ali (2014)
Corrosion rate, i_c	µA/cm^2	1.0	0.20	Log-normal	Val et al. (1998)
Corrosion model error, γ_{ic}	-	1.0	0.20	Normal	Bigaud and Ali (2014); Stewart and Rosowsky (1998b); Vu and Stewart (2000)

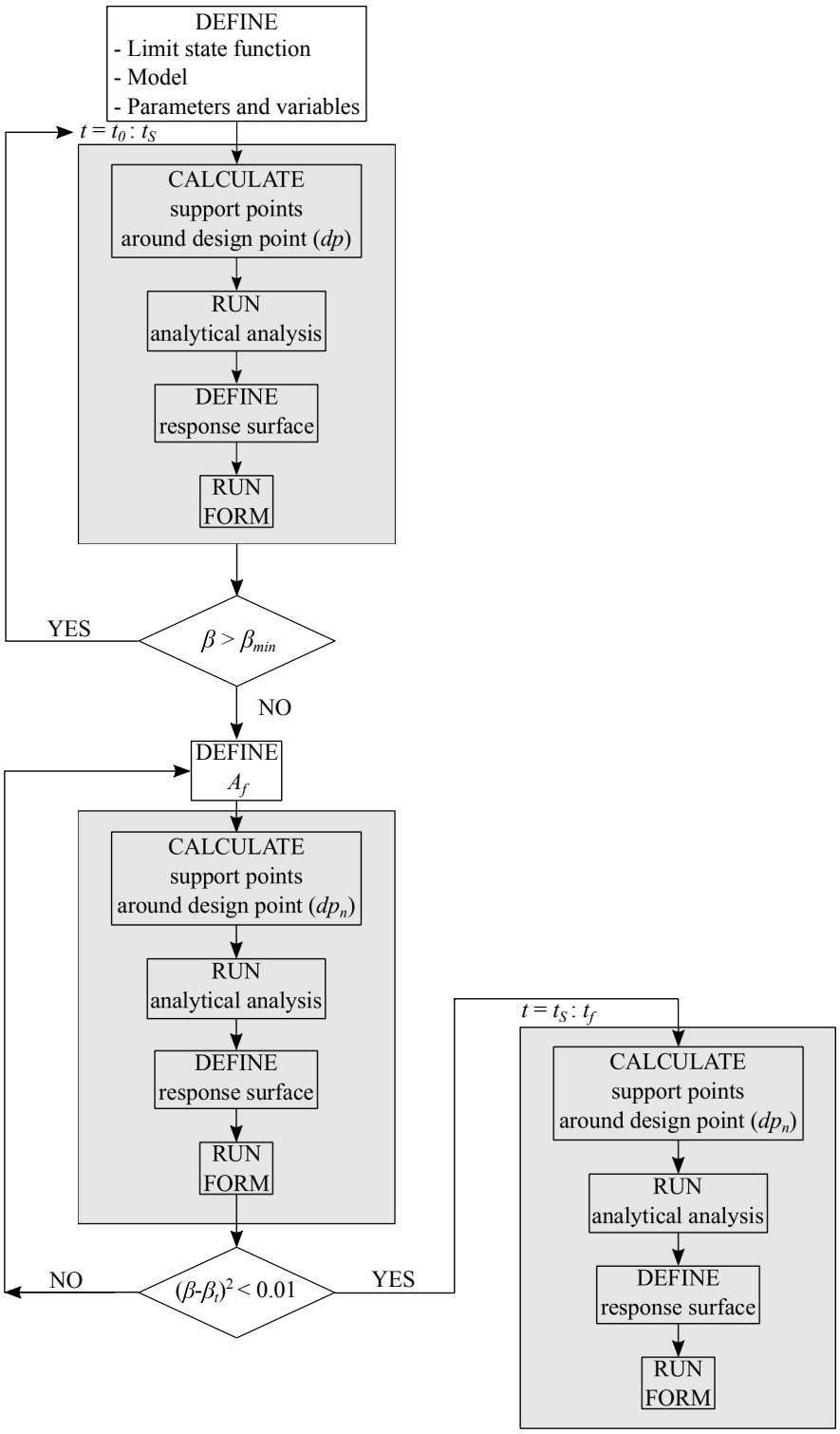

Figure 6.13: Time-dependent reliability analysis procedure flowchart.

and the reliability index, β_{n+1}. In the end of each iteration, convergence is checked by computing the difference between the reliability indices from the previous and present iterations. When this value is higher than 1%, convergence is not achieved and the procedure needs to be repeated. If the converged reliability index is higher than the minimum acceptable reliability index, the cycle is repeated for another time increment. Otherwise, strengthening is considered. In this thesis, the minimum acceptable reliability index was considered to be equal to 2.5, the same value by the ASHTO LRFD (1994) for the strength assessment of bridge members.

CFRP strengthening area calculation

The second cycle consists in the computation of the area required to increase the reliability to an acceptable level. CFRP strength, f_f, random variable is included in the analysis at this stage. Before it starts a value for the area of CFRP is initialised. Then, for different values of the area of CFRP, RSM and FORM are used to compute the design points and reliability index until convergence is reached; when the difference between reliability indices calculated from the previous and present iterations is not higher than 1%. When convergence is verified, it is checked if the area of CFRP can satisfy the objective of safety, which is achieved when the square of the difference between the computed reliability index and the target reliability index is less than 1%. In this thesis, a target reliability index of 3.8 was considered. According to Steenbergen and Vrouwenvelder (2010), this value is acceptable for repair scenarios of structures with very large consequences of failure associated with loss of human lives and economic damage.

Time-dependent reliability analysis of CFRP strengthened girders

The third cycle calculates reliability and probability of failure after the strengthening. The surface chloride concentration, C_s, the threshold chloride concentration, C_{th}, the chloride diffusion coefficient, D_{cl}, the concrete cover, c, the corrosion rate, i_c and the corrosion model error, γ_{ic}, are included at this stage. This cycle takes into consideration corrosion of prestressing steel and the FRP degradation over time. The same steps and convergence criteria considered for the first cycle are adopted herein.

6.4 Results

6.4.1 Reliability analysis of series system

Figure 6.14 shows the probability of failure calculated according to different approaches for reliability analysis of series system, as a function of time for the non-strengthened girder. When segments are considered to be statistically independent, the probability of failure is much higher for the earlier years. The same is not observed when segments are considered fully correlated, in which results are similar to the ones computed according to the Ditlevsen (1979) bounds; in particular in agreement to the lower Ditlevsen (1979) bound. These results show that there exists a big gap between the full correlated and independent segments, what makes this approach not realistic. Moreover, if segments are considered to be statistically independent, the probability of failure corresponds to the weakest segment, which may be conservative for the studied case. On the other hand, when segments are considered to be fully correlated, the probability of failure is much lower, given the fact that it depends on the perfect correlation of all segments.

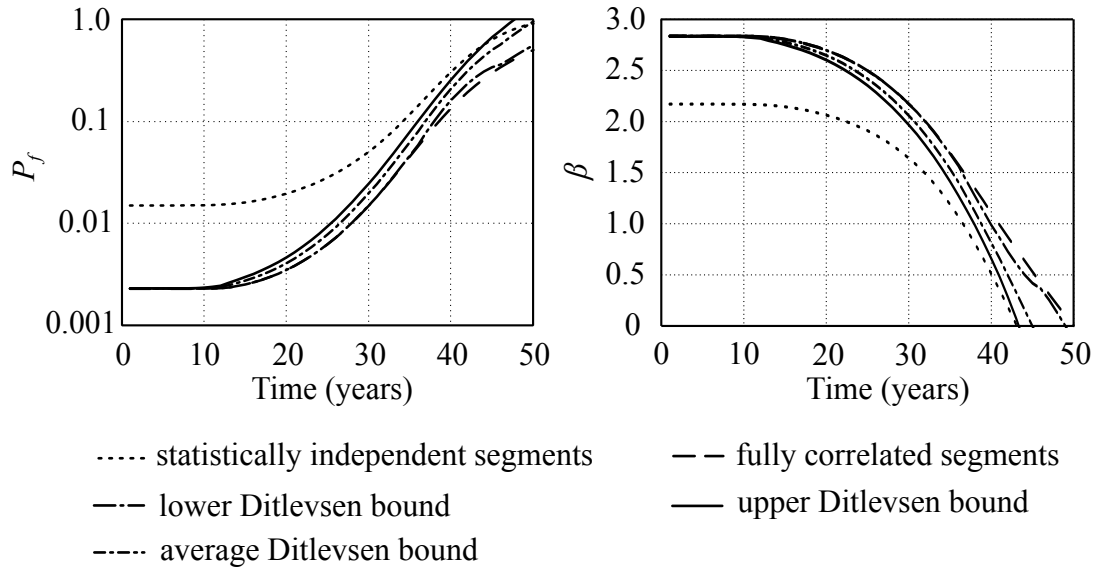

Figure 6.14: Probability of failure (P_f) and reliability index (β) as a function of time for different series reliabilities approaches.

The Ditlevsen (1979) bounds are an alternative way of computing reliability of se-

ries systems by considering the correlation between segments. In Figure 6.14 the probability of failure calculated using the Ditlevsen (1979) upper and lower bounds presents closer results. Additionally, these are less conservative up to 40 years, than the ones determined considering all segments statistically independent. The Ditlevsen (1979) bound corresponding to the average between bounds, shows proximity to results from perfect correlation for almost up to 40 years and statistically independent for the latter years. These results highlight the importance of the correlation segments assessment when dealing with reliability of series systems.

6.4.2 Time-dependent reliability analysis

The time-dependent safety without considering CFRP degradation is illustrated in Figure 6.15. The initial reliability index corresponds to a value of 2.8, below the minimum proposed in CEN (2002a). This is related with the fact that the girder was designed considering the Portuguese code, that, as already mentioned, is less conservative that the European code. Corrosion starts at an age of 11 years, but only becomes more severe after year 20. Then, if no strengthening is considered, the girder reaches a null reliability index at year 45. After chloride induction corrosion starts, the girder safety quickly decreases, as in accordance with the observations of several authors, e.g., Ali et al. (2012), Val et al. (1998) or Darmawan and Stewart (2007b).

The strengthening was calculated when the reliability index reached a minimum value of 2.5 (ASHTO LRFD, 1994), to increase the reliability index up to 3.8 (Steenbergen and Vrouwenvelder, 2010) using strengthening of 340 mm^2. After girders strengthening, the degradation due to corrosion is slightly seen, proving that the determined area of CFRP successfully replaces the reinforcement.

When CFRP degradation is taken into account – see Figure 6.16 – reliability decreases after strengthening, keeping a linear reduction over the years. Moreover, CFRP degradation is not as severe as chloride induction corrosion, as seen by Ali et al. (2012).

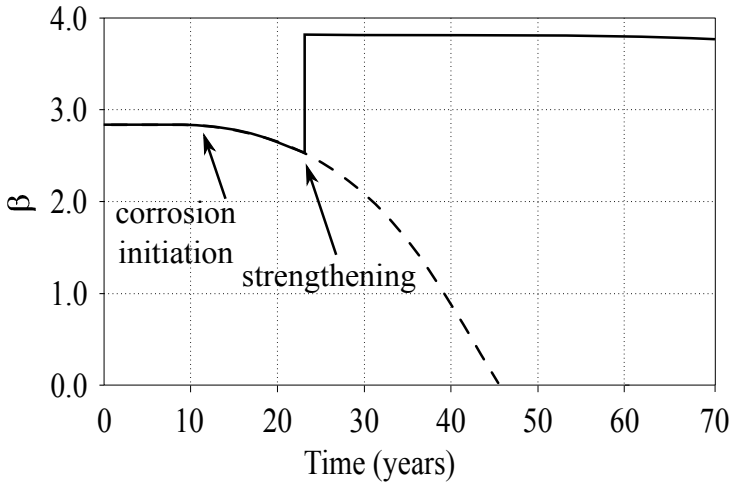

Figure 6.15: Reliability index as a function of time for strengthened section without considering environmental CFRP degradation.

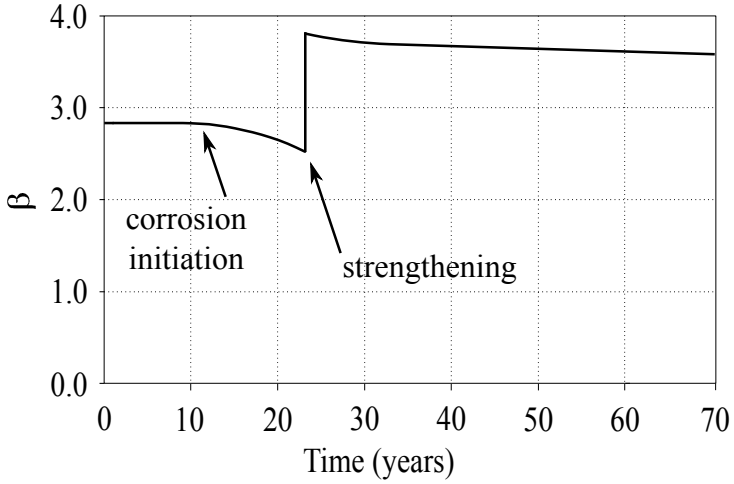

Figure 6.16: Reliability index as a function of time for strengthened section considering environmental CFRP degradation.

6.4.3 Sensitivity analysis

The cosines direction at design point for each random variables as a function of time, are presented in Figure 6.17. The values close to zero present an irrelevant impact on the analysis, whereas cosines close to -1 or 1 have respectively, a significant negative or positive impact.

As shown, traffic loads, γ_{tl}, show the highest weight in the analysis reaching a value

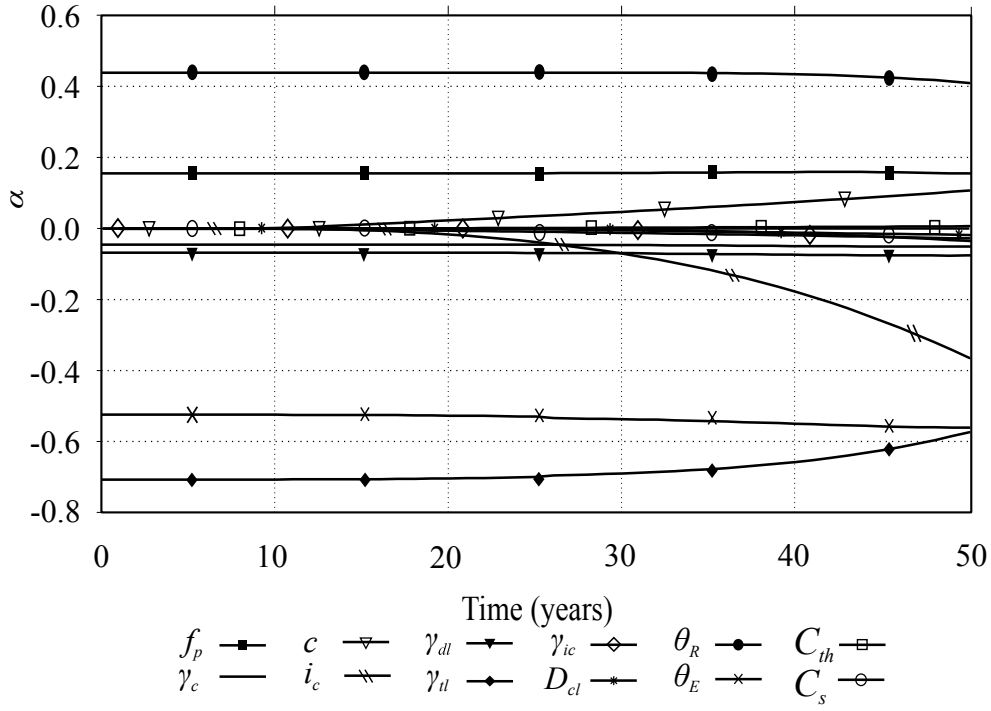

Figure 6.17: Cosines direction at design points as a function of time.

close to -0.7 and exhibiting a reduction of its importance as corrosion increases. The resistance and load models uncertainties, θ_R and θ_S, have cosine values close to 0.42 and -0.55, respectively, and remain almost constant over the analysis. The prestressing strength, f_p, presents values around 0.18, whereas the concrete self-weight, γ_c, and the dead loads, γ_{dl}, present values close to -0.10. On the other hand, the remaining variables, including the surface chloride concentration, C_s, threshold chloride concentration, C_{th}, chloride diffusion coefficient, D_{cl}, and corrosion model error, γ_{ic}, exhibit values close to zero over the analysis. Moreover, after the corrosion initiation, the most important variables related with this phenomenon are the concrete cover, c, and corrosion rate, i_c, that start to increase its weight as corrosion raises, reaching respectively to 0.12 and -0.38 at 50 years.

After the CFRP strengthening, the equilibrium present in the cosines direction changes, since the flexural strength is recovered – see Figure 6.18. As a result, the traffic load, γ_{tl}, increases its importance to values similar to the first years before strengthening, whereas concrete cover, c, and corrosion rate, i_c, decrease its weight to values similar to the one when corrosion is not initiated yet. Additionally,

the CFRP strength, f_f, assumes a weight of 0.10. The computed values remain practically constant over time since degradation is slow – see Figure 6.15.

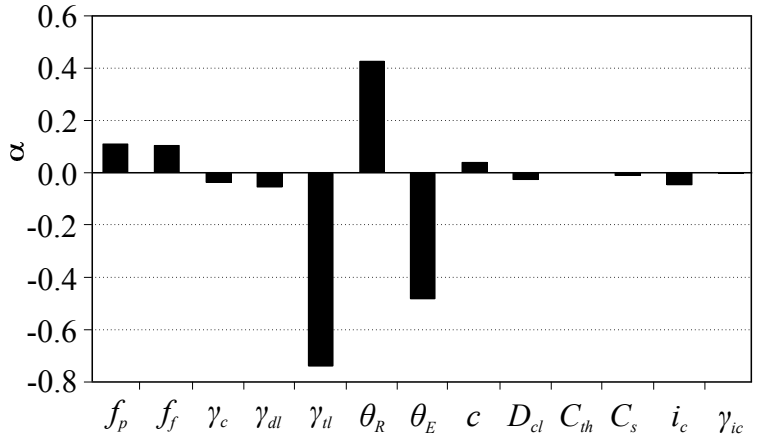

Figure 6.18: Cosines direction at design point for CFRP strengthening girder.

6.5 Conclusions

This chapter presented a time-dependent reliability analysis of CFRP strengthened PC girders considering: i) the spatial and temporal corrosion degradation process, ii) structural strengthening using CFRP, iii) FRP degradation process, iv) reliability of series system; and v) RSA (1983) to perform the design of the girder and CEN (2002b) for the CFRP strengthening.

The reliability of girder was computed considering a series system. Results show that reliability index is more conservative when segments are considered statistically independent. On the other hand, when the Ditlevsen (1979) bounds are considered, reliability index is more conservative than when segments are considered fully correlated, in special for the last years. This shows the importance to include correlation between segments in the analysis.

Results from time-dependent reliability analysis show that corrosion strongly affects the safety of the bridge and that the CFRP strengthening clearly extends structural life. Additionally, the CFRP degradation does not affect reliability as much as corrosion degradation does. The presented results show that corrosion starts after

11 years and the girders should be repaired after 23 years, using a cross-sectional area of CFRP of 340 mm^2. However, the results should not be treated in absolute sense, since the outcomes were computed based on the aforementioned corrosion conditions. Thus, more studies to extend and develop the knowledge about corrosion and FRP degradation must be made.

The sensitivity analysis shows that traffic loads, models uncertainties and corrosion rate are the most important variables for the analysis, followed by prestressing strength and concrete cover. Moreover, when corrosion effects increase, corrosion rate and concrete cover variables increase its importance, whereas traffic loads decrease. After strengthening, a new balance is computed and corrosion rate clearly reduces its importance.

Chapter 7

Closing remarks

7.1 Summary and main conclusions

In this thesis, the reliability of PC girders flexurally strengthened using CFRP is studied. The main objective is to establish a framework to assess the reliability of these structural elements. Concrete bridges using PC girders are an important element of the traffic network heritage. Usually, these structures behave well throughout its service life, when properly constructed and maintained. When subjected to aggressive environments or as a result of poor design or materials, the onset of corrosion can reduce their lifetime. As structures age, governments are faced with the increasing pressure to maintain structural safety within budgetary constrains and to avoid traffic interruptions. Consequently, the use of FRP as EBR as way to address current needs, is becoming more common. However, FRP still remains as a relative new material inside the construction filed, when compared with others, such as concrete or steel.

After a short introduction, in Chapter 2 a literature review on structural reliability, focusing the main issues of this topic is presented. This chapter intends to give the theoretical background that served as the basis of this thesis.

Chapter 3 addresses FRP as a strengthening material within structural reliability context, in which statistical models for composites are fundamental. Following the

existing literature review on the available statistical FRP models in construction field, the need for more robust statistical characterisations was identified.

Statistical models were defined based on an extensive data base – the largest considered so far – for Young's modulus, ultimate strain and tensile strength. The sample characteristics shows that appropriate attention should be given to the lower tail regions, to properly develop statistical models that can be used in reliability studies. In this context, the MLE method was successfully applied to accurately characterise the statistical nature of composites, in particular the region of interest for reliability studies – the lower tail.

Based on the analysis it is concluded that the Weibull distribution can be used to model the studied mechanical properties. The proposed models are in agreement with previous studies based on small sample sizes – see Atadero (2006); Zureick et al. (2006) – or other engineering fields, such as aerospace (Zureick et al., 2006). Moreover, it is important to highlight the low CoV obtained for properties, specially when compared with other studies (Atadero, 2006; Zureick et al., 2006). This may be related with the fact that the studied samples are prefabricated laminates and produced under the same conditions, at the same manufacturer. A properly definition of CoV using reasonable size samples is important, since it strongly influences reliability studies. The correlation analysis shows a strong dependency between tensile strength and ultimate strain, whereas tensile strength and Young's modulus, and ultimate strain and Young's modulus can be considered as independent variables.

In Chapter 4, the adopted numerical and analytical models of FRP strengthening beams are described. The developed FE model intended to simulate the non-linear structural behaviour of PC girders using a discrete crack approach for fracture, and interface elements for simulating FRP-concrete bond. An analytical model based on the sectional analysis method was also considered. Both models were validated based on experimental tests of 1/2 scale HSC girders, showing a good agreement with experimental data.

The developed numerical model allows characterising in a more realistic manner the concrete girders, since it considers the full structural behaviour, whereas the analytical model regards several simplifications and is limited to the sectional analysis. Nevertheless, the former model is computationally much more expensive, which can

be critical when reliability analysis are considered, given the high number of runs needed for each iteration. Based on this, numerical and analytical models were considered in Chapter 5 for the reliability based CFRP partial safety factors calibration, whereas in Chapter 6 the analytical model was used for the time-dependent reliability analysis.

The method presented in Chapter 5 uses a hybrid approach that considers both numerical and analytical models to save computational time, and to attain the non-linear structural behaviour for the calibration of CFRP partial safety factors. The computed reliability index is slightly higher when obtained with numerical model, than when computed using the analytical model, meaning that numerical model predicts higher resistances.

The RSA (1983) and CEN (2002b) codes were adopted at design and strengthening stages, respectively, to replicate real situations that may occur in Portugal. This is considered to be important since the conclusions from Chapter 5 show that the first code is less conservative than the European standard. Moreover, it is already outdated as it was developed in the 1960s, when traffic needs were significantly lower. On the other hand, the latter code may not be the most appropriate for Portugal, because it was developed in the 1990s for the central Europe countries, where needs are different than the border countries.

Several degraded girders rehabilitated with CFRP were considered for the reliability study. It can be concluded that, CFRP strengthening can restore the full structural capacity of girders for acceptable reliability indices compatible with CEN (2002a). The flexural strengthening can increase structural capacity up to 74% for damaged girders, and up to 25% for undamaged girders.

The most important parameters for the analysis are traffic loads, followed by models uncertainties. This means that a correct definition of traffic loads CoV is fundamental, since it can drastically impact results. The resistance variables prestressing strength and CFRP strength present lower importance when compared with the latter variables, but are essential because failure occurs by CFRP rupture after prestressing yield. The less relevant variables are concrete self-weight and dead loads.

The presented results show that a partial safety factor of 1.13 can be used for the

design of the CFRP strengthening for PC concrete girders. This factor is similar to what proposed in several guidelines, such as CNR (2013) or CEB/FIB (2001).

The use of numerical models that have into account structural non-linearities considering strong discontinuities coupled with the FORM, proves to be an useful tool to predict partial safety factors for CFRP. With this approach, the non-linear behaviour existing in concrete due to cracking before FRP debond and in the FRP-concrete interface is considered in detail. Moreover, the method proposed herein can be employed to develop safety factors for existing structures considering several uncertainties sources for FRP. The main limitation is related with the fact that, the required FE analysis are time consuming.

The time-dependent reliability analysis described in Chapters 6 considers the most concerning degradation cause for RC structures – reinforcing corrosion – by using existing analytical models to account for the temporal variation, and by treating spatial variation of pitting corrosion with series system reliability.

The Ditlevsen (1979) bounds allow computing series system reliability by having into account the possible correlations between segments. This consideration assumes a particular importance when pitting corrosion over the beam length is considered, because the definition of the size of segments and the distribution used for model pitting is not straightforward. Therefore, the use of the Ditlevsen (1979) bounds can enhance the reliability computation of PC girders for corrosion spatial variability.

Results allow to conclude that when segments are considered to be statistically independent, the reliability index is much more conservative, than when correlation between segments is considered. On the other hand, the reliability index based on the Ditlevsen (1979) bounds is less conservative, than when fully correlated segments are taken into account, in particular for the last years.

The initial reliability index is low for the CEN (2002a) demands, given to the RSA (1983) requests. Furthermore, pitting corrosion can reduce reliability index to zero, in a period of 30 years after corrosion initiation. On the other hand, CFRP strengthening can replace successfully the lost reinforcement and recover structural reliability for a long period of time, to reliability index values according to ASHTO LRFD (1994). Although, further discussion is needed to establish a proper methodology

to calibrate target reliability index for existing structures.

FRP degradation has reduced impact on the reliability index over time. In this study, this phenomenon was characterised using deterministic variables; but, improved models are needed to statistically characterise FRP degradation for reliability studies.

The traffic loads and models uncertainties are the most relevant variables for this analysis. The importance of traffic loads reduces with corrosion, whereas corrosion rate increases its weight. After the strengthening, variables significance assume values similar to the years before the onset of corrosion, remaining constant until the end of the analysis.

The proposed framework can be used by engineers and researchers as a tool to support decisions for structural maintenance. The use of series system reliability to account spatial corrosion can improve the computation of reliability index when pitting corrosion is considered.

7.2 Contributions to the research field

Several contributions for this research can be highlighted as a result of this thesis, namely:

- **CFRP statistical models**

  new CFRP statistical models based on a large batch of tensile tests have been developed for three relevant mechanical properties: i) Young's modulus, ii) tensile strength; and iii) ultimate strain. Moreover, correlation models between properties have also been proposed;

- **Calibration of CFRP partial safety factors considering reliability analysis**

  a reliability based analysis methodology for CFRP partial safety factors calibration, considering the most relevant uncertainties and the standards contextualisation, has been presented. Furthermore, FE models of PC girders used

for the calibration of CFRP partial safety factors, with strong discontinuities and interface elements that can be used for describing the non-linear behaviour of these structural elements, have been addressed;

- **Time-dependent reliability analysis of PC girders strengthened with CFRP considering steel corrosion and CFRP strength degradation**

  a methodology to assess the time-dependent reliability of PC girders strengthened with CFRP has been proposed, taking into account series reliability for spatial pitting corrosion variation using the Ditlevsen (1979) bounds and CFRP strength degradation.

7.3 Future developments

During the course of writing this thesis, several assumptions were made to overcome the existing limitations, becoming clear that further research is still needed within this subject. The extension of statistical analysis to other data bases containing tensile tests of FRP, including FRP wet-layup sheets made at the application local should be studied. Furthermore, it is important to gather data and develop models, having into account degradation due to real environmental conditions, rather than experimental accelerated laboratory tests.

In this thesis, failure was considered to occur due to FRP rupture after prestressing yield. Nevertheless, the composite debonding is one of the major causes for FRP strengthened structural elements failure. Addressing this failure mode is of great interest for future research in the reliability contextualisation. Moreover, the proposed methodology to assess the time-dependent reliability using analytical models considers the analysis at a sectional level. The application of numerical models that have into account the non-linear structural behaviour should be considered for future research. Also, the use of this type of analysis to predict an optimal time to strengthening can be done.

Bibliography

M. A. Abanilla, V. M. Karbhari, and Y. Li. Interlaminar and intralaminar durability characterization of wet layup carbon/epoxy used in external strengthening. *Composites Part B: Engineering*, 37(7 - 8):650 – 661, 2006a. ISSN 1359-8368. doi: http://dx.doi.org/10.1016/j.compositesb.2006.02.023.

M. A. Abanilla, Y. Li, and V. M. Karbhari. Durability characterization of wet layup graphite/epoxy composites used in external strengthening. *Composites Part B: Engineering*, 37(2 - 3):200 – 212, 2006b. ISSN 1359-8368. doi: http://dx.doi.org/10.1016/j.compositesb.2005.05.016.

Abaqus. Abaqus v.6.10. Dassault Systems/Simulia, USA, 2010.

ACI 440. Guide for the Design and Construction of Externally Bonded FRP Systems for Strengthening Concrete Structures (ACI 440.2R-08). American Concrete Institute, 2008.

ACI Committee 222. Protection of Metals in Concrete Against Corrosion. Technical Report ACI 222R-01, American Concrete Institute, 2001.

ACI Committee 440. State-of-the-Art Report on Fiber Reinforced Plastic (FRP) Reinforcement for Concrete Structures. Technical Report ACI 440R-96, American Concrete Institute, 1996.

M. Aktas and Y. Sumer. Nonlinear finite element analysis of damaged and strengthened reinforced concrete beams. *J. Civ. Eng. Manag.*, 20(2):201–210, 2014.

G. J. Al-Sulaimani, M. Kaleemullah, I. A. Basunbul, and Rasheeduzzafar. Influence of Corrosion and Cracking on Bond Behavior and Strength of Reinforced Concrete Members. *Structural Journal*, 87(2):220–231, 1990.

O. Ali. *Time-dependent reliability of FRP strengthened reinforced concrete beams under coupled corrosion and changing loading effects*. PhD thesis, l'Institut des Sciences et Techniques de l'Ingénieur d'Angers, 2012.

O. Ali, D. Bigaud, and E. Ferrier. Comparative durability analysis of CFRP-strengthened RC highway bridges. *Construction and Building Materials*, 30(0): 629 – 642, 2012. ISSN 0950-0618. doi: http://dx.doi.org/10.1016/j.conbuildmat.2011.12.014.

M. Ali-Ahmad, K. Subramaniam, and M. Ghosn. Experimental Investigation and Fracture Analysis of Debonding between Concrete and FRP Sheets. *J. Eng. Mech.*, 132(9):914–923, 2006.

D. E. Allen. Limit states criteria for structural evaluation of existing buildings. *Canadian Journal of Civil Engineering*, 18(6):995–1004, 1991. doi: 10.1139/l91-122.

A. A. Almusallam, A. S. Al-Gahtani, A. R. Aziz, and Rasheeduzzafar. Effect of reinforcement corrosion on bond strength. *Construction and Building Materials*, 10(2):123 – 129, 1996. ISSN 0950-0618. doi: http://dx.doi.org/10.1016/0950-0618(95)00077-1.

M. Alqam, R. M. Bennett, and A.-H. Zureick. Three-parameter vs. two-parameter Weibull distribution for pultruded composite material properties. *Compos. Struct.*, 58(4):497 – 503, 2002. ISSN 0263-8223. doi: http://dx.doi.org/10.1016/S0263-8223(02)00158-7.

J. E. Anderson and A. Vesterinen. Structural health monitoring systems. Technical report, 2006.

A. Ang and W. Tang. *Probability concepts in engineering: Emphasis on applications in civil & environmental engineering*. John Wiley & Sons, Chichester, 2nd edition, 2007.

A. Ashour, S. El-Refaie, and S. Garrity. Flexural strengthening of RC continuous beams using CFRP laminates. *Cement and Concrete Composites*, 26(7):765 – 775, 2004. ISSN 0958-9465. doi: http://dx.doi.org/10.1016/j.cemconcomp.2003.07.002.

ASHTO. Guide Specifications for Design of Bonded FRP Systems for Repair and Strengthening of Concrete Bridge Elements. American Association of State Transportation and Comunication, 2012.

ASHTO LRFD. Load and Resistance Factor Bridge Design Specifications. American Association of State Transportation and Comunication, 1994.

ASHTO LRFD. Manual for Condition Evaluation and Load and Resistance Factor Rating of Highway Bridges. American Association of State Transportation and Comunication, 2002.

R. A. Atadero. *Development of load and resistance factor design for FRP strengthening of reinforced concrete structures*. PhD thesis, University of California, 2006.

R. A. Atadero and V. M. Karbhari. Calibration of resistance factors for reliability based design of externally-bonded FRP composites. *Compos. Part B-Eng.*, 39(4): 665 – 679, 2008. ISSN 1359-8368.

H. A. Baky, U. A. Ebead, and K. W. Neale. Flexural and Interfacial Behavior of FRP-Strengthened Reinforced Concrete Beams. *Journal of Composites for Construction*, 11(6):629–639, 2007. doi: 10.1061/(ASCE)1090-0268(2007)11:6(629).

P. Balaguru, A. Nanni, and J. Giancaspro. *FRP Composites for Reinforced and Prestressed Concrete Structures: A Guide to Fundamentals and Design for Repair and Retrofit*. Taylor & Francis's Structural Engineering: Mechanics and Design series, 2008.

J. Barros, S. Dias, and J. Lima. Efficacy of CFRP-based techniques for the flexural and shear strengthening of concrete beams. *Cement and Concrete Composites*, 29(3):203 – 217, 2007. ISSN 0958-9465. doi: http://dx.doi.org/10.1016/j.cemconcomp.2006.09.001.

J. Barros, S. Dias, and J. ao Lima. Progress in developing a reliability-based design philosophy for FRP-strengthened concrete structures. In *Fourth International Conference on FRP Composites in Civil Engineering (CICE2008)*, 2008.

E. Bastidas-Arteaga, P. Bressolette, A. Chateauneuf, and M. Sánchez-Silva. Probabilistic lifetime assessment of RC structures under coupled corrosion-fatigue deterioration process. *Structural Safety*, 31(2):84–96, 2009. ISSN 0167-4730.

Z. P. Bažant and B. H. Oh. Crack band theory for fracture of concrete. *Materials and Structures*, 16(3):155–177, 1983. ISSN 1871-6873. doi: 10.1007/BF02486267.

E. Benvenuti, O. Vitarelli, and A. Tralli. Delamination of FRP-reinforced concrete by means of an extended finite element formulation. *Composites Part B: Engineering*, 43(8):3258 – 3269, 2012. ISSN 1359-8368. doi: http://dx.doi.org/10.1016/j.compositesb.2012.02.035.

D. Bigaud and O. Ali. Time-variant flexural reliability of RC beams with externally bonded CFRP under combined fatigue-corrosion actions. *Reliability Engineering & System Safety*, 131(0):257 – 270, 2014. ISSN 0951-8320. doi: http://dx.doi.org/10.1016/j.ress.2014.04.016.

Bikeoff Design Resource. accessed January 2016 . URL `http://www.bikeoff.org/design_resource`.

R. d. Borst, J. J. C. Remmers, A. Needleman, and M.-A. Abellan. Discrete vs smeared crack models for concrete fracture: bridging the gap. *Int. J. Numer. Anal. Met.*, 28(7-8):583–607, 2004. ISSN 1096-9853.

S. M. Bruce, P. S. McCarten, S. A. Freitag, and L. M. Hasson. Deterioration of prestressed concrete bridge beams. Technical Report 337, Land Transport New Zealand, 2008.

C. Bucher. *Computational Analysis of Randomness in Structural Mechanics: Structures and Infrastructures Book Series*, volume 3. 2009.

J. Cabrera. Deterioration of concrete due to reinforcement steel corrosion. *Cement and Concrete Composites*, 18(1):47 – 59, 1996. ISSN 0958-9465. doi: http://dx.doi.org/10.1016/0958-9465(95)00043-7.

G. Camata, E. Spacone, and R. Zarnic. Experimental and nonlinear finite element studies of RC beams strengthened with FRP plates. *Composites Part B: Engineering*, 38(2):277 – 288, 2007. ISSN 1359-8368. doi: http://dx.doi.org/10.1016/j.compositesb.2005.12.003.

CEB/FIB. FIB - Bulletin 10 - Bond of reinforcement in concrete. Fédération internationale du béton (FIB), 2000.

CEB/FIB. FIB - Bulletin 14 - Externally Bonded FRP Reinforcement for RC. Fédération internationale du béton (FIB), 2001.

A. M. Ceci, J. R. Casas, and M. Ghosn. Statistical analysis of existing models for flexural strengthening of concrete bridge beams using FRP sheets. *Construction and Building Materials*, 27(1):490 – 520, 2012. ISSN 0950-0618. doi: http://dx.doi.org/10.1016/j.conbuildmat.2011.07.014.

CEN. EN 1990: Eurocode 0: Basis of Structural Design. European Committee for Standardization, 2002a.

CEN. EN1991-2: Eurocode 1: Actions on Structures - Part 2: Traffic Loads on Bridges. European Committee for Standardization, 2002b.

CEN. EN 1992-1-1: Eurocode 2: design of concrete structures, Part 1-1: General rules and rules for buildings. European Committee for Standardization, 2004.

G. Chen, J. Chen, and J. Teng. On the finite element modelling of RC beams shear-strengthened with FRP. *Constr. Build. Mater.*, 32:13 – 26, 2012. ISSN 0950-0618.

G. M. Chen, J. G. Teng, and J. F. Chen. Finite-Element Modeling of Intermediate Crack Debonding in FRP-Plated RC Beams. *J. Compos. Constr.*, 15(3):339–353, 2011.

J. Chen and W. Pan. Three dimensional stress distribution in FRP-to-concrete bond test specimens. *Construction and Building Materials*, 20(1 - 2):46 – 58, 2006. ISSN 0950-0618. doi: http://dx.doi.org/10.1016/j.conbuildmat.2005.06.037.

J. F. Chen and J. G. Teng. Anchorage Strength Models for FRP and Steel Plates Bonded to Concrete. *Journal of Structural Engineering*, 127(7):784–791, 2001. doi: 10.1061/(ASCE)0733-9445(2001)127:7(784).

CNR. Guide for the Design and Construction of Externally Bonded FRP Systems for Strengthening Existing Structures. National Research Council, Advisory Committee on Technical Recommendations for Constructuion, 2013.

C. A. Coronado and M. M. Lopez. Sensitivity analysis of reinforced concrete beams strengthened with FRP laminates. *Cement. Concrete Aggr.*, 28(1):102 – 114, 2006. ISSN 0958-9465.

C. A. Coronado and M. M. Lopez. Numerical Modeling of Concrete-FRP Debonding Using a Crack Band Approach. *J. Compos. Constr.*, 14(1):11–21, 2010.

L. Correia, T. Teixeira, J. Michels, J. ao A.P.P. Almeida, and J. Sena-Cruz. Flexural behaviour of RC slabs strengthened with prestressed CFRP strips using different anchorage systems. *Composites Part B: Engineering*, 81:158 – 170, 2015. ISSN 1359-8368. doi: http://dx.doi.org/10.1016/j.compositesb.2015.07.011.

CSA. CSA International. Section 16. Canadian Highway Bridge Design Code, 2006.

M. S. Darmawan and M. G. Stewart. Effect of pitting corrosion on capacity of prestressing wires. *Magazine of Concrete Research*, 59:131–139(8), 2007a.

M. S. Darmawan and M. G. Stewart. Spatial time-dependent reliability analysis of corroding pretensioned prestressed concrete bridge girders. *Structural Safety*, 29 (1):16 – 31, 2007b. ISSN 0167-4730. doi: http://dx.doi.org/10.1016/j.strusafe.2005.11.002.

E. David and J. D. Neuner. Environmental durability studies for FRP systems: definition of normal conditions of use of FRP for structural strengthening applications. Honk Kong, 2001.

D. Dias-da-Costa. *Strong Discontinuities in the scope of the Discrete Crack Approach*. PhD thesis, Universidade de Coimbra, Portugal, 2010.

D. Dias-da-Costa, J. Alfaiate, L. Sluys, and E. Júlio. A discrete strong discontinuity approach. *Eng. Fract. Mech.*, 76(9):1176 – 1201, 2009. ISSN 0013-7944.

O. Ditlevsen. Narrow reliability bounds for structural systems. *Journal of Structural Mechanics*, 7(4):453–472, 1979. doi: 10.1080/03601217908905329.

S. El-Tawil and A. Okeil. Design of Concrete Bridge Girders Strengthened with CFRP Laminates. Report, University of Florida, 2001.

S. El-Tawil and A. M. Okeil. LRFD Flexural Provisions for Prestressed Concrete Bridge Girders Strengthened with Carbon Fiber-Reinforced Polymer Laminates. *ACI Struct. J.*, 99(2):181–190, 2002.

B. R. Ellingwood. Probability-based codified design: past accomplishments and future challenges. *Structural Safety*, 13(3):159 – 176, 1994. ISSN 0167-4730. doi: http://dx.doi.org/10.1016/0167-4730(94)90024-8.

B. R. Ellingwood. Reliability-based condition assessment and LRFD for existing structures. *Structural Safety*, 18(2–3):67 – 80, 1996. ISSN 0167-4730. doi: http://dx.doi.org/10.1016/0167-4730(96)00006-9.

B. R. Ellingwood. LRFD: implementing structural reliability in professional practice. *Engineering Structures*, 22(2):106 – 115, 2000. ISSN 0141-0296. doi: http://dx.doi.org/10.1016/S0141-0296(98)00099-6.

B. R. Ellingwood. Acceptable risk bases for design of structures. *Prog. Struct. Eng. Mat.*, 3(2):170–179, 2001. ISSN 1528-2716. doi: 10.1002/pse.78.

A. C. Estes. *A System Reliability Approach to the Lifetime Optimization of Inspection and Repair of HigHigh Bridges*. PhD thesis, University of Colorado, 1997.

M. Faber. *Risk and Safety in Civil, Surveying and Environmental Engineering*. Institute of Structural Engineering - Group Risk and Safety, 2005.

M. H. Faber and J. D. Sorensen. Reliability Beased Code Calibration. 2002.

M. H. Faber, J. Köhler, and J. D. Sorensen. Probabilistic modeling of graded timber material properties. *Struct. Saf.*, 26(3):295 – 309, 2004. ISSN 0167-4730. doi: http://dx.doi.org/10.1016/j.strusafe.2003.08.002.

P. Fernandes. *Vigas de Grande Vão Prefabricadas em Betão de Alta Resistência Pré-Esforçado*. PhD thesis, Universidade de Coimbra, Portugal, 2005.

P. Fernandes, J. Sena-Cruz, C. Fernandes, P. Silva, D. Dias-da-Costa, and E. Júlio. Flexural response of HSC girders strengthened with non- and prestressed CFRP laminates. Guimarães, Portugal, 2013.

FERUM. Finite element reliability using matlab. URL `http://www.ifma.fr/FERUM`.

B. Fischhoff, P. Slovic, S. Lichtenstein, S. Read, and B. Combs. How safe is safe enough? A psychometric study of attitudes towards technological risks

and benefits. *Policy Sciences*, 9(2):127–152, 1978. ISSN 0032-2687. doi: 10.1007/BF00143739.

A. Fortes, J. Barros, and I. Padaratz. Estudo comparativo de três técnicas de reforço à flexão com CFRP. Brasil, 2003.

H. Garden and L. Hollaway. An experimental study of the failure modes of reinforced concrete beams strengthened with prestressed carbon composite plates. *Compos. Part B-Eng.*, 29(4):411 – 424, 1998. ISSN 1359-8368.

N. Gayton, A. Mohamed, J. Sorensen, M. Pendola, and M. Lemaire. Calibration methods for reliability-based design codes. *Struct. Saf.*, 26(1):91 – 121, 2004. ISSN 0167-4730.

S. Gomes, P. Fernandes, D. D. da Costa, and E. Júlio. Numerical study of the flexural behaviour of precast Prestressed high strength concrete beams. Coimbra, Portugal, 2011.

S. Gomes, L. Neves, D. D. da Costa, P. Fernandes, and E. Júlio. Anélise de incertezas na resistência de vigas de betão de alta resistência pré-esforçado. Porto, Portugal, 2012.

S. Gomes, L. Neves, D. D. da Costa, P. Fernandes, and E. Júlio. Probabilistic models for mechanical properties of prefabricated CFRP. Guimarães, Portugal, 2013.

S. Gomes, L. Neves, D. D. da Costa, P. Fernandes, and E. Júlio. Probabilistic Analysis of High Strength Concrete Girders Strengthened with CFRP. Liverpool, United Kingdom, 2014a.

S. Gomes, L. Neves, D. D. da Costa, P. Fernandes, and E. Júlio. Análise Probabilística de Vigas Prefabricadas em Betão Pré-esforçado Reforçadas com Laminados de CFRP. Lisboa, Portugal, 2014b.

G&P intech s.r.l. accessed January 2016 . URL `http://www.english.gpintech.com`.

R. Graça-e Costa, J. Alfaiate, D. Dias-da Costa, and L. J. Sluys. A non-iterative approach for the modelling of quasi-brittle materials. *Int. J. Fracture*, 178(1): 281–298, 2012. ISSN 1573-2673.

R. Graça-e-Costa. *Modelling Nonlinear Fracture Behaviour using Non-iterative Numerical Methods*. PhD thesis, Universidade Técnica de Lisboa, Instituto Superior Técnico, Portugal, 2012.

R. Graça-e-Costa, J. Alfaiate, D. Dias-da-Costa, P. Neto, and L. Sluys. Generalisation of non-iterative methods for the modelling of structures under non-proportional loading. *Int. J. Fracture*, 182(1):21–38, 2013. ISSN 0376-9429.

M. A. Gutiérrez. Energy release control for numerical simulations of failure in quasi-brittle solids. *Communications in Numerical Methods in Engineering*, 20(1):19–29, 2004. ISSN 1099-0887. doi: 10.1002/cnm.649.

A. Haldar and S. Mahadevan. *Reliability Assessment Using Stochastic Finite Element Analysis*. John Wiley & Sons, 2000.

Handbook-MIL 17. *Guidelines for characterization of structural materials*. The Composite Materials Handbook-MIL 17, 2002.

D. Hanselman. *Matlab 6: curso completo*. Prentice Hall, 2013.

K. A. Harries, J. Kasan, and C. Aktas. Repair Method for Prestressed Girder Bridges. Technical Report FHWA-PA-2009-008-PIT 006, University of Pittsburg, 2009.

P. Holzenkämpfer. *Ingenieurmodelle des verbundes geklebter bewehrung für betonbauteile*. PhD thesis, TU Braunschweig, 1994.

H.-T. Hu, F.-M. Lin, and Y.-Y. Jan. Nonlinear finite element analysis of reinforced concrete beams strengthened by fiber-reinforced plastics. *Composite Structures*, 63(3–4):271 – 281, 2004. ISSN 0263-8223. doi: http://dx.doi.org/10.1016/S0263-8223(03)00174-0.

ISIS. Strengthening reinforced concrete structures with externally-bonded fibre reinforced polymers. ISIS Design Manual NO. 4, 2001.

ISIS. Reinforcing concrete structures with fibre reinforced polymers. ISIS Design Manual NO. 3, 2007.

ISO 527-5:2009. Plastic - determination of tensile properties - Part 5: Test ccondition for unidiretional fibre.reinforced plastic composites. European Committee for Standardization, 2009.

L. Jacinto, M. Pipa, L. A. Neves, and L. O. Santos. Probabilistic models for mechanical properties of prestressing strands. *Constr. Build. Mater.*, 36(0):84 – 89, 2012. ISSN 0950-0618.

JCSS. Probabilistic Model Code, 2001. URL `http://www.jcss.byg.dtu.dk/Probabilistic`.

JSCE. Recommendations for upgrading of concrete structures with use of continuous fiber sheets. Japanese Society of Civil Engineers, 2001.

V. Kaliakin and J. Li. Insight into deficiencies associated with commonly used zero-thickness interface elements. *Computers and Geotechnics*, 17(2):225 – 252, 1995. ISSN 0266-352X. doi: http://dx.doi.org/10.1016/0266-352X(95)93870-O.

V. M. Karbhari and M. A. Abanilla. Design factors, reliability, and durability prediction of wet layup carbon/epoxy used in external strengthening. *Composites Part B: Engineering*, 38(1):10 – 23, 2007. ISSN 1359-8368. doi: http://dx.doi.org/10.1016/j.compositesb.2006.06.001.

V. M. Karbhari, J. W. Chin, D. Hunston, B. Benmokrane, T. Juska, R. Morgan, J. J. Lesko, U. Sorathia, and D. Reynaud. Durability Gap Analysis for Fiber-Reinforced Polymer Composites in Civil Infrastructure. *Journal of Composites for Construction*, 7(3):238–247, 2003. doi: 10.1061/(ASCE)1090-0268(2003)7:3(238).

P. L. Kelley, M. L. Brainerd, and M. Vatovec. Design Philosophy for Structural Strengthening with FRP. *Concrete International*, 22(2):77 – 82, 2000.

I. Khan, R. François, and A. Castel. Structural performance of a 26-year-old corroded reinforced concrete beam. *European Journal of Environmental and Civil Engineering*, 16(3-4):440–449, 2012. doi: 10.1080/19648189.2012.667992.

N. Kishi, G. Zhang, and H. Mikami. Numerical Cracking and Debonding Analysis of RC Beams Reinforced with FRP Sheet. *J. Compos. Constr.*, 9(6):507–514, 2005.

M. B. Leeming and L. C. Hollaway. *Strengthening of Reinforced Concrete Structures*. Woodhead Publishing Limited, 1999.

K. Liao. In-situ Strength Degradation of Glass Fibers in a Pultruded Composite by Environmental Aging. *Journal of Materials Science Letters*, 18(10):763–765, 1999. ISSN 1573-4811. doi: 10.1023/A:1006624730257.

D. V. Lindley. *Introduction to probability and statistics*. Cambridge University Press, 1965.

L. Lorenzis, B. Miller, and A. Nanni. Bond of Fiber-Reinforced Polymer Laminates to Concrete. *ACI Materials Journal*, 98(3):256–264, 2001.

X. Lu, J. Teng, L. Ye, and J. Jiang. Bond-slip models for FRP sheets/plates bonded to concrete. *Eng. Struct.*, 27(6):920 – 937, 2005a. ISSN 0141-0296.

X. Lu, L. Ye, J. Teng, and J. Jiang. Meso-scale finite element model for FRP sheets/plates bonded to concrete. *Engineering Structures*, 27(4):564 – 575, 2005b. ISSN 0141-0296. doi: http://dx.doi.org/10.1016/j.engstruct.2004.11.015.

X. Z. Lu, J. G. Teng, L. P. Ye, and J. J. Jiang. Intermediate Crack Debonding in FRP-Strengthened RC Beams: FE Analysis and Strength Model. *Journal of Composites for Construction*, 11(2):161–174, 2007. doi: 10.1061/(ASCE)1090-0268(2007)11:2(161).

S. Marfia, E. Sacco, and J. Toti. A coupled interface-body nonlocal damage model for FRP strengthening detachment. *Computational Mechanics*, 50(3):335–351, 2012. ISSN 1432-0924. doi: 10.1007/s00466-011-0592-7.

MC 2010. Model Code 2010 - Design Manual. CEB/FIP, 2010.

MC 90. Model Code 90 - Design Manual. CEB/FIP, 1991.

R. E. Melchers. *Structural Reliability Analysis and Prediction*. Wiley, 1999.

R. E. Melchers. Assessment of Existing Structures Approaches and Research Needs. *Journal of Structural Engineering*, 127(4):406–411, 2001. doi: 10.1061/(ASCE)0733-9445(2001)127:4(406).

A. E. Menoufy and K. Soudki. Flexural behavior of corroded pretensioned girders repaired with CFRP sheets. *PCI Journal Paper*, 59(2):129.143, 2004. ISSN 0950-0618.

A. Nataf. Determination des distributions dont les merges sont donnees. *Comptes Rendus de l'Academie des Sciences*, 225:42–43, 1962.

P. Neto, J. Alfaiate, and J. Vinagre. Numerical modelling of concrete beams reinforced with pre-stressed CFRP. *Int. J. Fracture*, 157(1-2):159–173, 2009. ISSN 0376-9429.

H. Niu and Z. Wu. Numerical Analysis of Debonding Mechanisms in FRP-Strengthened RC Beams. *Comput-Aided Civ. Inf.*, 20(5):354–368, 2005. ISSN 1467-8667.

A. S. Nowak and K. R. Collins. *Reliability of Structures*. CRC Press, 2012.

Y. T. Obaidat, S. Heyden, and O. Dahlblom. The effect of CFRP and CFRP/concrete interface models when modelling retrofitted RC beams with FEM. *Compos. Struct.*, 92(6):1391 – 1398, 2010. ISSN 0263-8223.

A. M. Okeil, S. El-Tawil, and M. Shahawy. Flexural Reliability of Reinforced Concrete Bridge Girders Strengthened with Carbon Fiber-Reinforced Polymer Laminates. *J. Bridge Eng.*, 7(5):290–299, 2002.

C. M. Paliga, A. C. Filho, M. V. Real, and S. M. C. Diniz. Reliability Analysis Methods Applied to Reinforced Concrete Beams Rehabilitated with CFRP Sheets. *Teoria e Prática na Engenharia Civil*, (17):57–66, 2011.

PCA. Corrosion of embedded metals. *Portland Cement Association*, accessed April 2016 2013. URL `http://www.bikeoff.org/design_resource`.

H. B. Pham and R. Al-Mahaidi. Reliablity analysis of bridge beams retrofitted with fibre reinforced polymers. *Compos. Struct.*, 82(2):177 – 184, 2008. ISSN 0263-8223.

N. Plevris, T. Triantafillou, and D. Veneziano. Reliability of RC Members Strengthened with CFRP Laminates. *J. Struct. Eng.*, 121(7):1037–1044, 1995.

R. Quantrill and L. Hollaway. The flexural rehabilitation of reinforced concrete beams by the use of prestressed advanced composite plates. *Compos. Sci. Technol.*, 58(8):1259 – 1275, 1998. ISSN 0266-3538.

H. Rahimi and A. Hutchinson. Concrete Beams Strengthened with Externally Bonded FRP Plates. *Journal of Composites for Construction*, 5(1):44 – 56, 2001. doi: 10.1061/(ASCE)1090-0268(2001)5:1(44).

REBAP. Regulamento de Estruturas de Betão Armado e Pré-Esforçado. Ministério da Habitação, Obras Públicas e Transportes, 1985.

M. Rezazadeh, J. Barros, and I. Costa. Analytical approach for the flexural analysis of RC beams strengthened with prestressed CFRP. *Compos. Part B-Eng.*, 73:16 – 34, 2015. ISSN 1359-8368.

Z. Rinaldi, S. Imperatore, and C. Valente. Experimental evaluation of the flexural behavior of corroded P/C beams. *Construction and Building Materials*, 24(11):2267 – 2278, 2010. ISSN 0950-0618. doi: http://dx.doi.org/10.1016/j.conbuildmat.2010.04.029.

P. A. Ritchie, D. A. Thomas, L.-W. Lu, and G. M. Conelly. External Reinforcement of Concrete Beams Using Fiber Reinforced Plastics. *ACI Struct. J.*, 88(4):490 – 500, 1991.

J. Rivera and V. Karbhari. Cold-temperature and simultaneous aqueous environment related degradation of carbon/vinylester composites. *Composites Part B: Engineering*, 33(1):17 – 24, 2002. ISSN 1359-8368. doi: http://dx.doi.org/10.1016/S1359-8368(01)00058-0.

J. Rodriguez, L. Ortega, and J. Casal. Load carrying capacity of concrete structures with corroded reinforcement. *Construction and Building Materials*, 11(4):239 – 248, 1997. ISSN 0950-0618. doi: http://dx.doi.org/10.1016/S0950-0618(97)00043-3. Corrosion and Treatment of Reinforced Concrete.

J. G. Roots. The role of structural modelling in preserving Amsterdam architectural city heritage. Guimarães, Portugal, 2001.

J. G. Rots, P. Nauta, G. M. A. Kusters, and J. Blaauwendraad. Smeared Crack Approach and Fracture Localization in Concrete. *Heron, Fracture Mechanics and Structural Aspects of Concrete*, 30(1):1–48, 1985. ISSN 0263-8223.

RSA. Regulamento de Segurança e Acções para Estruturas de Edifícios e Pontes. Ministério da Habitação, Obras Públicas e Transportes, 1983.

J. C. J. Schellekens and R. De Borst. On the numerical integration of interface elements. *International Journal for Numerical Methods in Engineering*, 36(1): 43–66, 1993. ISSN 1097-0207. doi: 10.1002/nme.1620360104.

J. Schneider. *Introduction to Safety and Reliability of Structures*. International Association for Bridge and Structural Engineering, 1997.

J. Sena-Cruz, J. Barros, M. Coelho, and M. R. Silva. Experimental and numerical study of distinct techniques to strengthen beams failing in bending under monotonic loading. Honk Kong, 2011.

Sika Group. accessed January 2016 . URL `http://lbn.sika.com/en/struct-bond-strength-redirect/sika-structural-strengthening-solutions.html`.

G. Spadea, F. Bencardino, and R. N. Swamy. Structural Behavior of Composite RC Beams with Externally Bonded CFRP. *J. Compos. Constr.*, 2(3):132–137, 1998. doi: 10.1061/(ASCE)1090-0268(1998)2:3(132).

R. D. J. M. Steenbergen and A. C. W. M. Vrouwenvelder. Safety philosophy for existing structures and partial factors for traffic loads on bridges. *Heron*, 55(2), 2010.

M. Stephens and R. D'Agostino. *Goodness-of-fit techniques*. Marcel Dekker, 1986.

M. G. Stewart. Spatial variability of pitting corrosion and its influence on structural fragility and reliability of RC beams in flexure. *Structural Safety*, 26(4):453 – 470, 2004. ISSN 0167-4730. doi: http://dx.doi.org/10.1016/j.strusafe.2004.03.002.

M. G. Stewart. Mechanical behaviour of pitting corrosion of flexural and shear reinforcement and its effect on structural reliability of corroding RC beams. *Structural Safety*, 31(1):19 – 30, 2009. ISSN 0167-4730. doi: http://dx.doi.org/10.1016/j.strusafe.2007.12.001.

M. G. Stewart. Spatial and time-dependent reliability modelling of corrosion damage, safety and maintenance for reinforced concrete structures. *Structure and Infrastructure Engineering*, 8(6):607–619, 2012. doi: 10.1080/15732479.2010.505379.

M. G. Stewart and A. Al-Harthy. Pitting corrosion and structural reliability of corroding RC structures: Experimental data and probabilistic analysis. *Reliability Engineering & System Safety*, 93(3):373 – 382, 2008. ISSN 0951-8320. doi: http://dx.doi.org/10.1016/j.ress.2006.12.013.

M. G. Stewart and J. A. Mullard. Spatial time-dependent reliability analysis of corrosion damage and the timing of first repair for RC structures. *Engineering Structures*, 29(7):1457 – 1464, 2007. ISSN 0141-0296. doi: http://dx.doi.org/10.1016/j.engstruct.2006.09.004.

M. G. Stewart and D. V. Rosowsky. Time-dependent reliability of deteriorating reinforced concrete bridge decks. *Structural Safety*, 20(1):91 – 109, 1998a. ISSN 0167-4730. doi: http://dx.doi.org/10.1016/S0167-4730(97)00021-0.

M. G. Stewart and D. V. Rosowsky. Structural Safety and Serviceability of Concrete Bridges Subject to Corrosion. *Journal of Infrastructure Systems*, 4(4):146–155, 1998b. doi: 10.1061/(ASCE)1076-0342(1998)4:4(146).

M. G. Stewart and Q. Suo. Extent of spatially variable corrosion damage as an indicator of strength and time-dependent reliability of RC beams. *Engineering Structures*, 31(1):198 – 207, 2009. ISSN 0141-0296. doi: http://dx.doi.org/10.1016/j.engstruct.2008.08.011.

A. A. Torres-Acosta, S. Navarro-Gutierrez, and J. Terán-Guillén. Residual flexure capacity of corroded reinforced concrete beams. *Engineering Structures*, 29(6):1145 – 1152, 2007. ISSN 0141-0296. doi: http://dx.doi.org/10.1016/j.engstruct.2006.07.018.

TR-55. Design guidance for strenghening concrete structures using fibre composite materials. SOCIETY, C.(ed.), 2000.

T. Triantafillou, N. Deskovic, and M. Deuring. Strengthening of Concrete Structures with Prestressed Fiber Reinforced Plastic Sheets. *ACI Struct. J.*, 89(3):235–244, 1992.

D. V. Val. Deterioration of Strength of RC Beams due to Corrosion and Its Influence on Beam Reliability. *Journal of Structural Engineering*, 133(9):1297–1306, 2007. doi: 10.1061/(ASCE)0733-9445(2007)133:9(1297).

D. V. Val and R. E. Melchers. Reliability of Deteriorating RC Slab Bridges. *Journal of Structural Engineering*, 123(12):1638–1644, 1997. doi: 10.1061/(ASCE)0733-9445(1997)123:12(1638).

D. V. Val and P. A. Trapper. Probabilistic evaluation of initiation time of chloride-induced corrosion. *Reliability Engineering & System Safety*, 93(3):364 – 372, 2008. ISSN 0951-8320. doi: http://dx.doi.org/10.1016/j.ress.2006.12.010.

D. V. Val, M. G. Stewart, and R. E. Melchers. Effect of reinforcement corrosion on reliability of highway bridges. *Engineering Structures*, 20(11):1010 – 1019, 1998. ISSN 0141-0296. doi: http://dx.doi.org/10.1016/S0141-0296(97)00197-1.

Vejdirektoratet. Reliability-Based Classification of the Load Carrying Capacity of Existing Bridges. Technical Report Report 291, Ministry of Transport, 2004.

C. V. Verhoosel, J. J. C. Remmers, and M. A. Gutiérrez. A dissipation-based arc-length method for robust simulation of brittle and ductile failure. *International Journal for Numerical Methods in Engineering*, 77(9):1290–1321, 2009. ISSN 1097-0207. doi: 10.1002/nme.2447.

K. A. T. Vu and M. G. Stewart. Structural reliability of concrete bridges including improved chloride-induced corrosion models. *Structural Safety*, 22(4):313 – 333, 2000. ISSN 0167-4730. doi: http://dx.doi.org/10.1016/S0167-4730(00)00018-7.

N. Wang, B. Ellingwood, and A.-H. Zureick. Reliability-Based Evaluation of Flexural Members Strengthened with Externally Bonded Fiber-Reinforced Polymer Composites. *J. Struct. Eng.*, 136(9):1151–1160, 2010. doi: 10.1061/(ASCE)ST.1943-541X.0000199.

D. F. Wisniéwski. *Safety Formats for the Assessment of Concrete Bridges*. PhD thesis, Universidade do Minho, Portugal, 2007.

R. S. Y. Wong and F. J. Vecchio. Towards Modeling of Reinforced Concrete Members with Externally Bonded Fiber-Reinforced Polymer Composites. *ACI Struct. J.*, 100(1):47 – 55, 2003.

S.-K. Woo, J.-W. Nam, J.-H. J. Kim, S.-H. Han, and K. J. Byun. Suggestion of flexural capacity evaluation and prediction of prestressed CFRP strengthened design. *Engineering Structures*, 30(12):3751 – 3763, 2008. ISSN 0141-0296. doi: http://dx.doi.org/10.1016/j.engstruct.2008.06.013.

W. Xue, Y. Tan, and L. Zeng. Flexural response predictions of reinforced concrete beams strengthened with prestressed CFRP plates. *Composite Structures*, 92(3): 612 – 622, 2010. ISSN 0263-8223. doi: http://dx.doi.org/10.1016/j.compstruct.2009.09.036.

D.-S. Yang, S.-K. Park, and K. W. Neale. Flexural behaviour of reinforced concrete beams strengthened with prestressed carbon composites. *Compos. Struct.*, 88(4): 497 – 508, 2009. ISSN 0263-8223.

Z. Yang, J. Chen, and D. Proverbs. Finite element modelling of concrete cover separation failure in FRP plated RC beams. *Construction and Building Materials*, 17 (1):3 – 13, 2003. ISSN 0950-0618. doi: http://dx.doi.org/10.1016/S0950-0618(02)00090-9.

M. B. Zidani, K. Belakhdar, A. Tounsi, and E. A. A. Bedia. Finite element analysis of initially damaged beams repaired with FRP plates. *Compos. Struct.*, 134:429 – 439, 2015. ISSN 0263-8223.

A.-H. Zureick, R. M. Bennett, and B. R. Ellingwood. Statistical Characterization of Fiber-Reinforced Polymer Composite Material Properties for Structural Design. *J. Struct. Eng.*, 132(8):1320–1327, 2006. doi: 10.1061/(ASCE)0733-9445(2006)132:8(1320).